GOETHE-UNIVERSITÄT FRANKFURT AM MAIN

Institut für Theoretische Physik
Max-von-Laue Straße 1
60438 Frankfurt am Main

MASTER THESIS

Inhomogeneous Phases in the 1 + 1-Dimensional Gross-Neveu Model at Finite Number of Fermion Flavors

Laurin Pannullo

Frankfurt am Main

Updated version from June 30, 2020 with minor corrections.

Supervisor and first examiner
Prof. Dr. Marc Wagner
Institut für Theoretische Physik
Goethe-Universität Frankfurt am Main

Second examiner
Prof. Dr. Andreas Wipf
Theoretisch-Physikalisches-Institut
Friedrich-Schiller-Universität Jena

Abstract

This thesis focuses on the investigation of the $1+1$-dimensional Gross-Neveu model at finite number of fermion flavors N_f using lattice field theory. A special emphasis is put on the search for an inhomogeneous phase, where the chiral condensate is an oscillating function in space. This inhomogeneous phase, a chirally symmetric phase and a homogeneously broken phase with a constant chiral condensate were originally found in the model in the limit of large-N_f. In the context of this work lattice Monte Carlo simulations of the Gross-Neveu model with various N_f for a wide range of lattice spacings and volumes were carried out. The nature of the employed numerical techniques prevents the direct observation of an inhomogeneous chiral condensate. However, an oscillating spatial correlator of the condensate field was found, which indicates a dominating oscillation in this field. This correlator is able to distinguish three regimes that resemble the large-N_f phases and as the final result a "phase diagram" consisting of these regimes is presented. The overall structure of the phase diagram is similar to the $N_\mathrm{f} \to \infty$ results and persistent for decreasing lattice spacing, thus ruling out that the inhomogeneous phase is merely a lattice artifact.

Contents

Introduction

Quantum Field Theory (QFT) is the theoretical framework that was conceived as the unification of quantum mechanics and special relativity. The description of individual particles evolved into quantized fields that would fluctuate, produce particles and annihilate them again. A particle ceased to be a permanent object by virtue of Einstein's energy-mass relation.

At the core of QFTs (and most other theories of modern physics) is the concept of symmetries. We require the theory to obey the symmetries observed in nature. In this context, symmetry means that the laws of physics do not change if we subject our system to certain transformations. These can be local symmetries that allow us to transform the system only in certain parts of spacetime for example gauge symmetries, which are the central component of theories like *Quantum electrodynamics* (QED) or *Quantum chromodynamics* (QCD). However, they also include global symmetries such as the Poincaré symmetry, which requires the theory to be independent of the frame of reference or space-time. Although we require the formulation of the theory to follow certain symmetries, it may happen that some of these symmetries are not realized in the observed ground state. This phenomenon is called *spontaneous symmetry breaking*.

In 1974 the *Gross-Neveu* (GN) model in $1+1$ dimensions was first proposed as a toy model for the mechanism of dynamical symmetry breaking in asymptotically free theories [1]. These are theories in which the interaction of particles becomes weaker as the energy scale increases, such as QCD. The GN model is arguably the simplest model of a class of quantum field theoretic models called *Four-fermion* (FF) theories that describe the interaction of fermions via a quartic interaction (or FF) term, whereas in the standard model the fermions' interactions are exclusively mediated by gauge bosons. The majority of investigations of the GN model were done in the large-N_f limit (N_f being the number of fermion flavors described by the model), which allows the use of semi-classical methods, since quantum fluctuations are suppressed. It was then found, that the discrete chiral symmetry of the model can be dynamically broken as indicated by a non-zero vacuum expectation value of the chiral condensate.

The GN model was also subjected to finite temperature and chemical potential in the large-N_f limit. Under the assumption of translation invariance of the chiral condensate a phase diagram of the model was produced, where the chiral symmetry was restored for either or both large temperature and large chemical potential [2]. This remained the accepted result until almost 30 years after the inception of the GN, when the assumption of the chiral condensate being homogeneous was discarded and a third *inhomogeneous phase* (IP) breaking translation invariance was found at large baryon chemical potential and small temperatures [3, 4]. In this novel phase the chiral condensate is an oscillating function in space. Such IPs have since been found also in other FF models in the large-N_f limit including (compare with Ref. [5]): the *Nambu-Jona-Lasinio* (NJL) model in $3+1$ dimensions [6], the chiral Gross-Neveu model in $1+1$ dimensions (also NJL_2) [7, 8] and more recently the $1+1$-dimensional isoNJL with multiple chemical potentials [9, 10]. The Quark-Meson model does also show inhomogeneities [6, 11] and is closely related to the $3+1$-dimensional NJL, albeit not a FF theory.

Interestingly, some of these models have counterparts in condensed matter physics, where the phase diagram (including the IP) of the GN model was found more than 20 years prior [12]. We are, however, more interested in the applications in high energy physics and in that context one could argue that the physics

in these models crudely resembles QCD. This leads to the obvious question whether its phase diagram also possesses IPs. Unfortunately, the aforementioned models point to the fact, that these phases occur at finite baryon chemical potential. This puts us in a difficult situation as the only available first principle approach, Lattice QCD, is confined to small ratios of chemical potential and temperature due to the sign problem. Pertubative approaches in the limit of large chemical potential and the large-N_c limit (t'Hooft limit) show indications of inhomogeneous condensates albeit inconclusive [13, 14]. Therefore, our idea of the phase diagram of QCD at low temperatures and high baryon chemical potential continues to rely on models for now.

Thus, one should be inclined to refine these models and bring them closer to QCD. To this extent one could consider, as a first step, to carry out an investigation of the GN model at finite N_f and explore whether the IP persists under the influence of quantum fluctuations. Such a study was already performed at $N_\mathrm{f} = 12$ on the lattice and even found indications of an inhomogenous behavior by recognizing the formation of single kink-antikink field configurations [15]. It was, however, not considered in the context of an IP and there was no follow-up work on this topic.

The focus of this thesis lies on the investigation of this IP in the $1+1$-dimensional GN model at finite N_f. In the context of this work lattice Monte Carlo simulations of naive fermions with $N_\mathrm{f} \geq 8$ at finite baryon chemical potential and temperature were performed. The character of the results is qualitative as producing quantitative results was not the intended goal and is numerically expensive. We thoroughly analyze these results to draw conclusions about the phases of the GN at finite N_f. The presented results are backed up by similar results obtained with SLAC fermions and extended by a thorough analysis on the possible existence of actual symmetry breaking of the translation symmetry, which is presented in Ref. [16].

Outline

This thesis is organized as follows:

Chapter 1 briefly introduces notation and the basic concepts of finite temperature QFT needed for the discussions in this thesis. Moreover, we consider some details of the GN model, for instance the different symmetries realized in the theory and a summary of the existing results in the large-N_f limit.

Chapter 2 discusses the lattice field theory techniques needed for our investigation. It starts by general considerations of the aspects of discretization of spacetime and fermions, continues with the discretization of the GN model and the possible errors one can make when using naive fermions, and ends with a brief description of the numerical technique of Monte Carlo simulations that was used to obtain the main results.

These results are presented in Chapter 3, where we discuss the phase diagram of the GN model at $N_\mathrm{f} = 8$ in detail and also connect to the existing large-N_f results by increasing the flavor number up to $N_\mathrm{f} = 24$. This presentation is preceded by the discussion of the employed observables.

We end with a brief conclusion of our findings and the prospects of possible future investigations in Chapter 4. The Appendices A to E contain supplementary calculations, discussions and material that would have cluttered the discussion and were consequently outsourced.

Notation

In analytic calculations not only parantheses () but also curly {} and square brackets [] are used to group terms. Hereby, the default order is {[()]}, but we might diverge from it at times in order to keep consistency across steps of a calculation. The brackets of arguments of functionals, sets and intervals are, of course, exempt from this and follow the usual conventions.

Throughout this work everything is expressed in natural units, i.e. setting $\hbar = c = k_B = 1$. Only Euclidean spacetime is considered, where the $D = d + 1$-dimensional metric reads

$$\delta_{\mu\nu} = \mathrm{diag}(+1, \underbrace{+1, +1, \ldots, +1}_{d \text{ components}}),$$

where the first component corresponds to the time or more precisely the temperature direction (as discussed in the next section) and the remaining are the spatial components. Indices of spacetime and other spaces (e.g. flavor space) that occur in pairs are summed over regardless of placement unless stated otherwise. Vectors with the dimension of the spacetime are in bold e.g. $\boldsymbol{x} = (x_\mu)^\mathsf{T} = (x^\mu)^\mathsf{T} = (x_0, x_1, \ldots, x_d)^\mathsf{T}$.

Fourier Transforms (FTs) are also performed and the FT of a function $f(x)$ is denoted as

$$\mathscr{F}_x\left[f(x)\right](k) = \tilde{f}(k),$$

where the subscript indicates that is transformed and the ~ indicates a Fourier transformed function. The transformation is then calculated as

$$\tilde{f}(k) = \frac{1}{\sqrt{2\pi}} \int \mathrm{d}x\, f(x)\, \mathrm{e}^{-\mathrm{i}kx},$$

$$f(x) = \frac{1}{\sqrt{2\pi}} \int \mathrm{d}x\, \tilde{f}(k)\, \mathrm{e}^{\mathrm{i}kx},$$

where a symmetric normalization of the transformation is chosen. Note that the choice of sign in the exponential and the normalization are equivalent for the discrete FTs performed on the lattice.

All other notations and conventions are introduced when they are first used.

1 Theoretical Preliminaries and the Gross-Neveu Model in 1 + 1 Dimensions

1.1 Thermal Quantum Field Theory

The Euclidean path integral in thermal QFT for a $D = d + 1$-dimensional arbitrary theory with fermionic fields $\bar{\psi}, \psi$ and a bosonic field ϕ is

$$Z = \int \mathscr{D}\bar{\psi}\mathscr{D}\psi\mathscr{D}\phi\, \mathrm{e}^{-S[\bar{\psi},\psi,\phi]}, \quad S[\bar{\psi},\psi,\phi] = \int \mathrm{d}^D\boldsymbol{x}\, \mathscr{L}, \tag{1.1}$$

where S is the action and $\mathscr{L}$ the Lagrange density that defines our theory, $\bar{\psi}, \psi$ are Grassmann-valued and $\int \mathscr{D}\phi$ integrates the field $\phi(\boldsymbol{x})$ at every spacetime point $\boldsymbol{x}$ over all possible values (the same applies for the fermion fields). Note that the Euclidean spacetime is the result of a Wick rotation of Minkowski spacetime, where real time is analytically continued to imaginary time. By restricting the temporal direction to finite size L_0 and introducing periodic boundary conditions for bosons, i.e. $\phi(x_0, x_1) = \phi(x_0 + L_0, x_1)$ and antiperiodic boundary conditions for fermions, i.e. $\psi(x_0, x_1) = -\psi(x_0 + L_0, x_1)$, we are able to rewrite the path integral as

$$Z(\beta) = \int_{\substack{\text{anti-}\\ \text{periodic}}} \mathscr{D}\bar{\psi}\mathscr{D}\psi \int_{\text{periodic}} \mathscr{D}\phi\, \mathrm{e}^{-S[\bar{\psi},\psi]} \equiv \mathrm{tr}\left(\mathrm{e}^{-\beta H}\right), \tag{1.2}$$

where H is the Hamiltonian that is connected to the Lagrange function $L = \int \mathrm{d}^d\boldsymbol{x}\, \mathscr{L}$ via the Legendre transformation. We identified the path integral with the canonical partition function $\mathrm{tr}\big(\exp(-\beta H)\big)$ known from statistical mechanics with the temperature given by $\beta = L_0 = 1/T$, thus giving a new meaning to the imaginary time. This, however, means that this formulation only describes equilibrium physics. The steps to show the equivalence involve, among other things, the introduction of canonical momenta fields π to perform the Legendre transformation. A detailed derivation can be found in textbooks such as Refs. [17, 18]. From here on, we no longer write the boundary conditions of the integral in Z for convenience.

Now that we established the connection to the canonical partition function, we can introduce a chemical potential in analogy to statistical mechanics and thereby transform the canonical partition function to the grand canonical partition function $\mathscr{Z}$ as

$$\mathscr{Z}(\beta,\mu) = \mathrm{tr}\left(\mathrm{e}^{-\beta(H-\mu N)}\right) = \int \mathscr{D}\bar{\psi}\mathscr{D}\psi\mathscr{D}\phi\, \mathrm{e}^{-S[\bar{\psi},\psi,\phi]+\mu Q} = \int \mathscr{D}\bar{\psi}\mathscr{D}\psi\mathscr{D}\phi\, \mathrm{e}^{-S[\bar{\psi},\psi,\phi](\mu)}, \tag{1.3}$$

where N is the baryon number operator and

$$Q = \int \mathrm{d}x_0\, N = \int \mathrm{d}^{d+1}\boldsymbol{x}\, \bar{\psi}\gamma_0\psi \quad \text{and} \quad S[\bar{\psi},\psi,\phi](\mu) = S[\bar{\psi},\psi,\phi] - \mu Q. \tag{1.4}$$

The expectation value of an observable O dependent on the fields is then calculated as

$$\langle O \rangle = \frac{1}{\mathcal{Z}} \int \mathcal{D}\bar{\psi}\mathcal{D}\psi\mathcal{D}\phi \;\; O[\bar{\psi},\psi,\phi]\, \mathrm{e}^{-S[\bar{\psi},\psi,\phi](\mu)}. \tag{1.5}$$

1.2 Four-Fermion Theories

A *Four-fermion* (FF) theory is a kind of QFT that has a Lagrangian consisting of a kinetic Dirac part and a quartic interaction of the fermionic fields—a so called FF interaction. The general form of the Lagrangian $\mathscr{L}$ for this kind of theory is

$$\mathscr{L} = \sum_{a=1}^{N_\mathrm{f}} \bar{\psi}_a(\boldsymbol{x})\,(\partial\!\!\!/ + m)\,\psi_a(\boldsymbol{x}) - \sum_{n=1}^{N} \frac{g_n^2}{2} \left(\sum_{a=1}^{N_\mathrm{f}} \bar{\psi}_a(\boldsymbol{x})\,\Gamma_{n,1}\psi_a(\boldsymbol{x}) \right) \left(\sum_{a=1}^{N_\mathrm{f}} \bar{\psi}_a(\boldsymbol{x})\,\Gamma_{n,2}\psi_a(\boldsymbol{x}) \right), \tag{1.6}$$

where $\partial\!\!\!/ = \gamma_\mu \partial_\mu$ is the derivative contracted with the Dirac gamma matrices, $\bar{\psi}, \psi$ are fermion spinors of N_f flavors and $\Gamma_{n,i}$ are N linearly independent matrices in spinor space. The FF term with different matrices Γ correspond to different interaction channels. The number of channels depend on the spinor representation , e.g. in $D = 4$ spacetime dimensions in the irreducible representation we find 16 independent matrices Γ or in $D = 2$ spacetime dimensions in the irreducible representation we find only 4 independent matrices Γ.

1.3 The Gross-Neveu Model in 1 + 1 Dimensions

The *Gross-Neveu* (GN) model is arguably the simplest FF theory as its Lagrangian features only a scalar interaction term [1]

$$\mathscr{L} = \sum_{a=1}^{N_\mathrm{f}} \bar{\psi}_a(\boldsymbol{x}) \left(\partial\!\!\!/ + \gamma_0\mu + m\right) \psi_a(\boldsymbol{x}) - \frac{g^2}{2} \left(\sum_{a=1}^{N_\mathrm{f}} \bar{\psi}_a(\boldsymbol{x})\,\psi_a(\boldsymbol{x}) \right)^2, \tag{1.7}$$

where we already introduced the chemical potential according to Eq. (1.3).[1] In the notation of Eq. (1.6) the GN model has $N = 1$ and $\Gamma_{1,1} = \Gamma_{1,2} = \mathbb{1}$. In the following, we suppress the summation over flavor indices whenever it is not important, so simply writing $\sum_{a=1}^{N_\mathrm{f}} \bar{\psi}_a(\boldsymbol{x})\,\psi_a(\boldsymbol{x}) = \bar{\psi}(\boldsymbol{x})\,\psi(\boldsymbol{x})$. In order for the action S to be dimensionless, the Lagrangian is required to have dimension $[\mathscr{L}] = L^{-2}$. The kinetic term fixes the dimension of the spinors as $[\psi] = [\bar{\psi}] = L^{-1/2}$, which in turn determines the coupling constant to be dimensionless, i.e. $\left[g^2\right] = 1$. This dimensionless coupling constant renders the theory pertubatively renormalizable, which holds for all FF theories in 2 spacetime dimensions.

Throughout this work we choose the irreducible representation of the Clifford algebra

$$\left\{\gamma_\mu, \gamma_\nu\right\} = 2\delta_{\mu\nu}, \tag{1.8}$$

of 2×2 $\gamma-$matrices, which can be constructed with the Pauli matrices. We do not have to make an explicit choice, since the matrices can always be transformed into each other by similarity transformations, but note that the Euclidean γ-matrices are all hermitian. We use only 2 of the 3 available γ-matrices in the

[1] Note that the sign is different to adjust for convention. This is not a problem, because the action is an even function of μ as shown in Appendix A.1.

kinetic part of $\mathscr{L}$ and can thus define the remaining matrix as γ_{ch}[2], which is relevant for chiral symmetry. Moreover, in this representation in 2 Euclidean dimensions, we find charge conjugation matrices $\mathscr{C}_{\pm}$ that fulfill (compare with Refs. [19, 20])

$$\mathscr{C}_{-}\gamma_{\mu}\mathscr{C}_{-}^{-1} = -\gamma_{\mu}^{\mathsf{T}}, \tag{1.9a}$$

$$\mathscr{C}_{+}\gamma_{\mu}\mathscr{C}_{+}^{-1} = \gamma_{\mu}^{\mathsf{T}}. \tag{1.9b}$$

1.3.1 Bosonization

A common practice, when investigating these FF theories, is to bosonize the action via a *Hubbard-Stratonovich* (HS) [21, 22] . This transformation can be seen as an inverse Gaussian integration

$$\exp\left[-\int \mathrm{d}^2\boldsymbol{x}\,\frac{g^2}{2}\left(\bar{\psi}(\boldsymbol{x})\,\psi(\boldsymbol{x})\right)^2\right] = \mathscr{N}\int \mathscr{D}\sigma\,\exp\left[-\int \mathrm{d}^2\boldsymbol{x}\left(\frac{N_{\text{f}}}{2\lambda}\sigma(\boldsymbol{x})^2 + \bar{\psi}(\boldsymbol{x})\,\sigma(\boldsymbol{x})\,\psi(\boldsymbol{x})\right)\right], \tag{1.10}$$

where $\mathscr{N}$ is a normalization constant to the transformation, and we introduced a scalar bosonic field σ and a rescaled coupling $\lambda = N_{\text{f}}g^2$. This leads to a Euclidean partition function without the FF interaction term

$$\mathscr{Z} = \int \mathscr{D}\bar{\psi}\mathscr{D}\psi\mathscr{D}\sigma\,\mathrm{e}^{-S_\sigma[\bar{\psi},\psi,\sigma]}, \quad S_\sigma[\bar{\psi},\psi,\sigma] = \int \mathrm{d}^2\boldsymbol{x}\left(\bar{\psi}(\boldsymbol{x})\,Q_{\text{GN}}(\boldsymbol{x})\,\psi(\boldsymbol{x}) + \frac{N_{\text{f}}}{2\lambda}\sigma(\boldsymbol{x})^2\right), \tag{1.11}$$

with

$$Q_{\text{GN}}(\boldsymbol{x}) \coloneqq \partial\!\!\!/ + \gamma_0\mu + \sigma(\boldsymbol{x}) + m, \tag{1.12}$$

where the auxiliary field σ now enters as a dynamically generated mass. Note that we neglected the normalization $\mathscr{N}$, which does not pose a problem, since we are only interested in observables. These are normalized by a factor of $1/\mathscr{Z}$ and thus a missing constant does not matter. In order to ease notation, we continue to neglect any normalization constants that arise from modifications to the path integral. Moreover, from here on we only consider the chiral limit, i.e. $m = 0$ unless stated otherwise.

One can connect the condensate field $\bar{\psi}\psi$ and the bosonic field σ using a series of Ward identities, which we derive in the following. First, consider an infinitesimal shift of σ as

$$\sigma(\boldsymbol{x}) \to \sigma'(\boldsymbol{x}) = \sigma(\boldsymbol{x}) + \delta\sigma(\boldsymbol{x}). \tag{1.13}$$

We apply this transformation to Eq. (1.11) and obtain

$$\begin{aligned}
\mathscr{Z}' &= \int \mathscr{D}\bar{\psi}\mathscr{D}\psi\mathscr{D}\sigma'\,\exp\left\{-\int \mathrm{d}^2\boldsymbol{x}\left[\bar{\psi}(\boldsymbol{x})\,(\partial\!\!\!/ + \gamma_0\mu + \sigma(\boldsymbol{x}) + \delta\sigma(\boldsymbol{x}) + m)\,\psi(\boldsymbol{x}) + \frac{N_{\text{f}}}{2\lambda}\,(\sigma(\boldsymbol{x}) + \delta\sigma(\boldsymbol{x}))^2\right]\right\} \\
&= \int \mathscr{D}\bar{\psi}\mathscr{D}\psi\mathscr{D}\sigma'\,\mathrm{e}^{-S[\bar{\psi},\psi,\sigma]}\,\exp\left\{-\int \mathrm{d}^2\boldsymbol{x}\,\delta\sigma(\boldsymbol{x})\left[\bar{\psi}(\boldsymbol{x})\,\psi(\boldsymbol{x}) + \frac{N_{\text{f}}}{2\lambda}\big(2\sigma(\boldsymbol{x}) + \delta\sigma(\boldsymbol{x})\big)\right]\right\} \\
&\approx \int \mathscr{D}\bar{\psi}\mathscr{D}\psi\mathscr{D}\sigma'\,\mathrm{e}^{-S[\bar{\psi},\psi,\sigma]}\left[1 - \int \mathrm{d}^2\boldsymbol{x}\,\delta\sigma(\boldsymbol{x})\left(\bar{\psi}(\boldsymbol{x})\,\psi(\boldsymbol{x}) + \frac{N_{\text{f}}}{\lambda}\sigma(\boldsymbol{x})\right)\right],
\end{aligned} \tag{1.14}$$

where we used the fact that $\delta\sigma(\boldsymbol{x})$ is infinitesimal in order to expand the exponential and to neglect terms of order $\mathscr{O}(\delta\sigma(\boldsymbol{x})^2)$. The integral in Eq. (1.11) has to be invariant under such a shift[3] and by assumption

[2] In 3 + 1 dimensions this "remaining" γ-matrix is often called γ_5.

[3] The integral integrates over all possible field values. Thus, a shift cannot influence the overall integral.

that the integral measure $\mathscr{D}\sigma$ is invariant under this transformation we derive

$$\begin{aligned}\mathscr{Z} \equiv \mathscr{Z}' &= \mathscr{Z} - \int \mathscr{D}\bar{\psi}\mathscr{D}\psi\mathscr{D}\sigma \left[\int \mathrm{d}^2\boldsymbol{x}\, \delta\sigma(\boldsymbol{x}) \left(\bar{\psi}(\boldsymbol{x})\psi(\boldsymbol{x}) + \frac{N_\mathrm{f}}{\lambda}\sigma(\boldsymbol{x})\right)\right] \mathrm{e}^{-S[\bar{\psi},\psi,\sigma]} \\ \Rightarrow 0 &= \int \mathscr{D}\bar{\psi}\mathscr{D}\psi\mathscr{D}\sigma \left[\int \mathrm{d}^2\boldsymbol{x}\, \delta\sigma(\boldsymbol{x}) \left(\bar{\psi}(\boldsymbol{x})\psi(\boldsymbol{x}) + \frac{N_\mathrm{f}}{\lambda}\sigma(\boldsymbol{x})\right)\right] \mathrm{e}^{-S[\bar{\psi},\psi,\sigma]}. \end{aligned} \tag{1.15}$$

The transformation $\delta\sigma(\boldsymbol{x})$ is arbitrary and by restricting it to a single site, i.e. $\delta\sigma(\boldsymbol{x}) = \delta(\boldsymbol{x}-\boldsymbol{y})\,\delta\sigma$, we obtain the Ward identity

$$\left\langle \bar{\psi}(\boldsymbol{x})\psi(\boldsymbol{x})\right\rangle = \frac{-N_\mathrm{f}}{\lambda}\left\langle\sigma(\boldsymbol{x})\right\rangle, \tag{1.16}$$

which links the chiral condensate $\left\langle \bar{\psi}(\boldsymbol{x})\psi(\boldsymbol{x})\right\rangle$ to the expectation value of the auxiliary field $\langle\sigma(\boldsymbol{x})\rangle$. Therefore, we also refer to $\langle\sigma(\boldsymbol{x})\rangle$ as the chiral condensate.

Furthermore, we want to derive a second Ward identity that links the correlators of the fields. As a starting point we choose the expectation value $\left\langle\sigma(\boldsymbol{y})\right\rangle$ and apply the transformation from Eq. (1.13), where the expectation value does not change under the transformation

$$\begin{aligned}\left\langle\sigma(\boldsymbol{y})\right\rangle \to \left\langle\sigma(\boldsymbol{y})\right\rangle &= \frac{1}{\mathscr{Z}}\int \mathscr{D}\bar{\psi}\mathscr{D}\psi\mathscr{D}\sigma'\,\sigma'(\boldsymbol{y})\,\mathrm{e}^{-S[\bar{\psi},\psi,\sigma']} = \frac{1}{\mathscr{Z}}\int \mathscr{D}\sigma\,\left(\sigma(\boldsymbol{y})+\delta\sigma(\boldsymbol{y})\right)\mathrm{e}^{-S[\bar{\psi},\psi,\sigma']} \\ &\approx \frac{1}{\mathscr{Z}}\int \mathscr{D}\bar{\psi}\mathscr{D}\psi\mathscr{D}\sigma\,\left(\sigma(\boldsymbol{y})+\delta\sigma(\boldsymbol{y})\right) \\ &\qquad\qquad \times\left[1-\int \mathrm{d}^2\boldsymbol{x}\,\delta\sigma(\boldsymbol{x})\left(\bar{\psi}(\boldsymbol{x})\psi(\boldsymbol{x})+\frac{N_\mathrm{f}}{\lambda}\sigma(\boldsymbol{x})\right)\right]\mathrm{e}^{-S[\bar{\psi},\psi,\sigma]} \\ &= \frac{1}{\mathscr{Z}}\int \mathscr{D}\bar{\psi}\mathscr{D}\psi\mathscr{D}\sigma\,\left(\sigma(\boldsymbol{y})+\delta(\boldsymbol{y}-\boldsymbol{z})\,\delta\sigma\right)\left[1-\delta\sigma\left(\bar{\psi}(\boldsymbol{z})\psi(\boldsymbol{z})+\frac{N_\mathrm{f}}{\lambda}\sigma(\boldsymbol{z})\right)\right]\mathrm{e}^{-S[\bar{\psi},\psi,\sigma]} \\ &= \left\langle\sigma(\boldsymbol{y})\right\rangle + \delta\sigma\left(\delta(\boldsymbol{y}-\boldsymbol{z}) - \left\langle\sigma(\boldsymbol{y})\bar{\psi}(\boldsymbol{z})\psi(\boldsymbol{z})\right\rangle - \frac{N_\mathrm{f}}{\lambda}\left\langle\sigma(\boldsymbol{z})\sigma(\boldsymbol{y})\right\rangle\right) \end{aligned} \tag{1.17}$$

$$\Rightarrow \frac{N_\mathrm{f}}{\lambda}\left\langle\sigma(\boldsymbol{y})\bar{\psi}(\boldsymbol{z})\psi(\boldsymbol{z})\right\rangle = \frac{N_\mathrm{f}}{\lambda}\delta(\boldsymbol{y}-\boldsymbol{z}) - \left(\frac{N_\mathrm{f}}{\lambda}\right)^2\left\langle\sigma(\boldsymbol{z})\sigma(\boldsymbol{y})\right\rangle, \tag{1.18}$$

where we chose $\delta\sigma(\boldsymbol{x}) = \delta(\boldsymbol{x}-\boldsymbol{z})\,\delta\sigma$ from line 2 to 3. Starting from $\left\langle\bar{\psi}(\boldsymbol{z})\psi(\boldsymbol{z})\right\rangle$ and performing similar steps yields

$$\frac{N_\mathrm{f}}{\lambda}\left\langle\sigma(\boldsymbol{y})\,\bar{\psi}(\boldsymbol{z})\,\psi(\boldsymbol{z})\right\rangle = -\left\langle\bar{\psi}(\boldsymbol{y})\psi(\boldsymbol{y})\,\bar{\psi}(\boldsymbol{z})\psi(\boldsymbol{z})\right\rangle. \tag{1.19}$$

Combining Eqs. (1.18) and (1.19) produces a Ward identity that connects the correlation functions of $\bar{\psi}\psi$ and σ as

$$\left\langle\bar{\psi}(\boldsymbol{y})\psi(\boldsymbol{y})\,\bar{\psi}(\boldsymbol{z})\psi(\boldsymbol{z})\right\rangle = -\frac{N_\mathrm{f}}{\lambda}\delta(\boldsymbol{y}-\boldsymbol{z}) + \left(\frac{N_\mathrm{f}}{\lambda}\right)^2\left\langle\sigma(\boldsymbol{z})\sigma(\boldsymbol{y})\right\rangle. \tag{1.20}$$

1.3.2 Symmetries

The action of the GN model respects various symmetries and in the following we examine those that are relevant for our investigations.

Poincaré Symmetry

In Euclidean spacetime the Lorentz transformations from Minkowski space become ordinary rotations of $SO(D)$ as the metric now has the same sign for every entry. Nevertheless, we continue to call this sort of transformation "Lorentz transformations" for simplicity's sake. The coordinates transform under such a transformation Λ as

$$x_\mu \to x'_\mu = \Lambda_{\mu\nu}\, x_\nu, \tag{1.21}$$

a scalar field is invariant as

$$\sigma(\boldsymbol{x}) \to \sigma'(\boldsymbol{x}') = \sigma(\boldsymbol{x}), \tag{1.22}$$

and the spinors transform as

$$\psi(\boldsymbol{x}) \to \psi'(\boldsymbol{x}') = S[\Lambda]\,\psi\left(\boldsymbol{x}'\right) = \exp\left[-\frac{\mathrm{i}}{2}\Omega_{\mu\nu}S_{\mu\nu}\right]\psi(\boldsymbol{x}), \tag{1.23a}$$

$$\bar{\psi}(\boldsymbol{x}) \to \bar{\psi}'(\boldsymbol{x}') = \exp\left[\frac{\mathrm{i}}{2}\Omega_{\mu\nu}S_{\mu\nu}\right]\bar{\psi}(\boldsymbol{x}), \tag{1.23b}$$

where $S_{\mu\nu} = [\gamma_\mu, \gamma_\nu]\,\mathrm{i}/4$ and $\Omega_{\mu\nu} = -\Omega_{\nu\mu}$ are the parameters of the Lorentz-Transformation (e.g. rotation angle).

The term $\bar{\psi}\gamma_0\mu\psi$ in the action breaks Lorentz symmetry explicitly for $\mu \neq 0$ (because of the accompanying γ_0). Also finite temperature breaks Lorentz invariance due to the (anti)periodic finite temporal extent.

The translation symmetry part of the Poincaré symmetry is not affected by finite temperature, chemical potential or Euclidean spacetime. The translation symmetry is realized in the action in Eq. (1.11) as it is invariant under a transformation

$$\boldsymbol{x} \to \boldsymbol{x}' = \boldsymbol{x} + \boldsymbol{\delta}, \tag{1.24}$$

where $\boldsymbol{\delta}$ is the constant by which we shift the system.

Flavor Symmetry

The flavors are degenerate in the GN model; therefore, the Lagrangian $\mathscr{L}$ in Eq. (1.7) is invariant under a unitary flavor transformation

$$\psi_a \to \psi_a = \left(\mathrm{e}^{\mathrm{i}\omega_A\lambda_A}\right)_{ab}\psi_b, \qquad \bar{\psi}_a \to \bar{\psi}_a = \bar{\psi}_b\left(\mathrm{e}^{-\mathrm{i}\omega_A\lambda_A}\right)_{ba}, \tag{1.25}$$

where λ^A are the $(N_\mathrm{f})^2 - 1$ generalized $N_\mathrm{f} \times N_\mathrm{f}$ Gell-Mann matrices [23].

Phase Symmetry

The Lagrangian $\mathscr{L}$ in Eq. (1.7) for one flavor is invariant under a global $U(1)$ transformation of the spinors as

$$\psi_a \to \psi'_a = \mathrm{e}^{\mathrm{i}\alpha\mathbb{1}}\psi_a, \qquad \bar{\psi}_a \to \bar{\psi}'_a = \bar{\psi}_a\mathrm{e}^{-\mathrm{i}\alpha\mathbb{1}}, \tag{1.26}$$

which becomes a $U(N_\mathrm{f})$ symmetry through the Flavor symmetry (in a similar way as described in Ref. [23], where the 2 + 1 Thirring model is considered).

Chiral Symmetry

The massless kinetic term in the Lagrangian $\mathscr{L}$ from Eq. (1.7) is invariant under a chiral transformation

$$\psi \to \psi' = \mathrm{e}^{\mathrm{i}\omega\gamma_\mathrm{ch}}\psi, \qquad \bar{\psi} \to \bar{\psi}' = \bar{\psi}\,\mathrm{e}^{\mathrm{i}\omega\gamma_\mathrm{ch}}. \tag{1.27}$$

Applying this transformation to the FF term yields

$$\begin{aligned}\left[\bar{\psi}_a\psi_a\right]\left[\bar{\psi}_b\psi_b\right] \to \left[\bar{\psi}'_b\psi'_b\right]\left[\bar{\psi}'_b\psi'_b\right] &= \left[\bar{\psi}_a\mathrm{e}^{2\mathrm{i}\omega\gamma_\mathrm{ch}}\psi_a\right]\left[\bar{\psi}_b\mathrm{e}^{2\mathrm{i}\omega\gamma_\mathrm{ch}}\psi_b\right] \\ &= \left[\bar{\psi}_a\left(\cos(2\omega)\mathbb{1}+\mathrm{i}\sin(2\omega)\gamma_\mathrm{ch}\right)\psi_a\right]\times\left[\bar{\psi}_b\left(\cos(2\omega)\mathbb{1}+\mathrm{i}\sin(2\omega)\gamma_\mathrm{ch}\right)\psi_b\right],\end{aligned} \tag{1.28}$$

where we used that the complex matrix exponential of the involutary matrix[4] A can be decomposed as

$$\mathrm{e}^{\mathrm{i}\alpha A} = \cos(\alpha)\mathbb{1}+\mathrm{i}\sin(\alpha)A. \tag{1.29}$$

Equation (1.28) shows that only parameters $\omega_o = (2n+1)\pi/2$ and $\omega_e = m\pi$ with $n, m \in \mathbb{Z}$ leave the whole action invariant. The even parameters ω_e correspond to a discrete phase transformation of the individual flavors as

$$\psi_a \to \psi'_a = \psi_a\cos(m\pi) = \psi_a(-1)^m, \qquad \bar{\psi}_a \to \bar{\psi}'_a = \bar{\psi}_a(-1)^m, \tag{1.30}$$

which is just a discrete subgroup of the aforementioned $U(N_\mathrm{f})$ phase transformation. The odd parameters ω_o correspond to

$$\psi \to \psi' = \sin((2n+1)\pi/2)\,\mathrm{i}\gamma_\mathrm{ch}\,\psi = (-1)^n\,\mathrm{i}\gamma_\mathrm{ch}\,\psi, \qquad \bar{\psi} \to \bar{\psi}' = \bar{\psi}\,(-1)^n\,\mathrm{i}\gamma_\mathrm{ch}, \tag{1.31}$$

where all flavors have to be transformed simultaneously. The transformation by $(-1)^n\,\mathrm{i}$ is again part of the $U(N_\mathrm{f})$. By using the transformations of this group from Eq. (1.26) to rotate the spinors by $\alpha = -\pi(n+1/2)$, we obtain a discrete $\mathbb{Z}_2$ chiral symmetry as

$$\psi \to \psi' = \gamma_\mathrm{ch}\,\psi, \qquad \bar{\psi} \to \bar{\psi}' = -\bar{\psi}\,\gamma_\mathrm{ch}. \tag{1.32}$$

To preserve this chiral symmetry in $\mathscr{L}_\sigma$, the auxiliary field σ has to be transformed as

$$\sigma \to -\sigma. \tag{1.33}$$

In the next section, we show that the action S_σ only depends on the determinant of the Dirac operator Q_GN, which is an even function in σ (see Appendix A.1), and thus allows the transformation of σ as in Eq. (1.33). It is actually not a new symmetry, instead just part of the chiral symmetry.

We conclude that the scalar FF interaction of the GN model explicitly breaks the original continuous chiral symmetry of Eq. (1.27) down to this discrete subgroup $\mathbb{Z}_2$.

[4] These are matrices that satisfy $A = A^{-1}$, i.e. matrices that are their own inverse.

1.3.3 The Limit of Large Number of Fermion Flavors

In the HS transformed action S_σ, the fermion fields only occur in bilinear form, which we can integrate out

$$\mathcal{Z} = \int \mathscr{D}\sigma \, \det(Q)^{N_\mathrm{f}} \exp\left(\int \mathrm{d}^2\boldsymbol{x} \, \frac{N_\mathrm{f}}{2\lambda}\sigma(\boldsymbol{x})^2\right) = \int \mathscr{D}\sigma \, \mathrm{e}^{-S_\mathrm{eff}[\sigma]}, \tag{1.34}$$

with

$$S_\mathrm{eff}[\sigma] = N_\mathrm{f}\left(\frac{1}{2\lambda}\int \mathrm{d}^2\boldsymbol{x} \, \sigma(\boldsymbol{x})^2 - \ln\det(Q)\right). \tag{1.35}$$

It is easy to see that for $N_\mathrm{f} \to \infty$ every contribution to the path integral but the global minimum of S_eff is infinitely suppressed. This classical field configuration σ' that minimizes the action globally is a solution to the gap equation[5]

$$\frac{\delta S[\sigma]}{\delta\sigma(\boldsymbol{x})} = 0. \tag{1.36}$$

This, in turn, means that expectation value of an observable O only relies on this classical configuration. Therefore, the expectation value reduces to

$$\langle O\rangle = \frac{1}{\mathcal{Z}}\int \mathscr{D}\sigma \, O[\sigma] \, \mathrm{e}^{-S_\mathrm{eff}[\sigma]} \overset{N_\mathrm{f}\to\infty}{=} O\left[\sigma'\right]. \tag{1.37}$$

In particular the chiral condensate $\langle\sigma(\boldsymbol{x})\rangle$ is then $\sigma'(\boldsymbol{x})$. The chiral condensate serves as an order parameter for the chiral symmetry and a non-zero value signals a broken chiral symmetry.

Homogeneous Phase Diagram

By restricting the chiral condensate $\langle\sigma\rangle$ to being constant in space, one has to consider only constant σ when minimizing S_eff. One then defines the effective potential $U_\mathrm{eff}(\sigma)$, with $S_\mathrm{eff} = N_\mathrm{f}\beta L_1 \, U_\mathrm{eff}$ (see Appendix B for the derivation of the renormalized effective potential), which is a "mexican-hat" potential. It is symmetric and has two global minima at $\sigma' = \pm\sigma_0$ for $\mu = 0$ and $T = 0$. The value σ_0 is used to set the scale and we express all quantities in units of σ_0. When fixing $\mu = 0$ and increasing the temperature T, the minima *move* towards the origin and continuously merge into a single minimum at $\sigma' = 0$ for a critical temperature $T_c/\sigma_0 = \mathrm{e}^\gamma/\pi \approx 0.567$ [6] (compare Figure 1.1b). Right at the transition, there is no energy barrier between the new minimum and the old minima characteristic to a second order phase transition. When fixing $T = 0$ and increasing the chemical potential, a competing local minimum, which is separated by an energy barrier from the global minima, forms and eventually becomes the global minimum at a critical chemical potential $\mu_c/\sigma_0 = 1/\sqrt{2} \approx 0.707$ (compare Figure 1.1c). This is a first order phase transition as the global minimum does not change continuously for varied chemical potential.

When minimizing the effective potential numerically[7] (as given in Eq. (B.15)) in the μ, T-plane one determines a "homogeneous" phase diagram. Figure 1.1a shows this phase diagram that consists of a *homogeneously broken phase* (HBP) with $\sigma' \neq 0$ and a *symmetric phase* (SP) $\sigma' = 0$. A second order phase boundary extends from $(\mu/\sigma_0, T/\sigma_0) = (0, \mathrm{e}^\gamma/\pi) \approx (0, 0.567)$ to the Lifshitz point at $(\mu/\sigma_0, T/\sigma_0) = (0.608, 0.318)$ as indicated by the smooth evolution of σ' to 0. From here the phase boundary continues as a first order phase transition to $(\mu/\sigma_0, T/\sigma_0) = (1/\sqrt{2}, 0) \approx (0.707, 0)$ [2].

[5] Note that there are also solutions that are local minima or maxima, which solve this equation.

[6] The constant γ is called the *Euler-Mascheroni* constant with $\gamma = 0.57721\ldots$.

[7] The integration in U_eff and its minimization is done with appropriate numeric routines from the `scipy` python library.

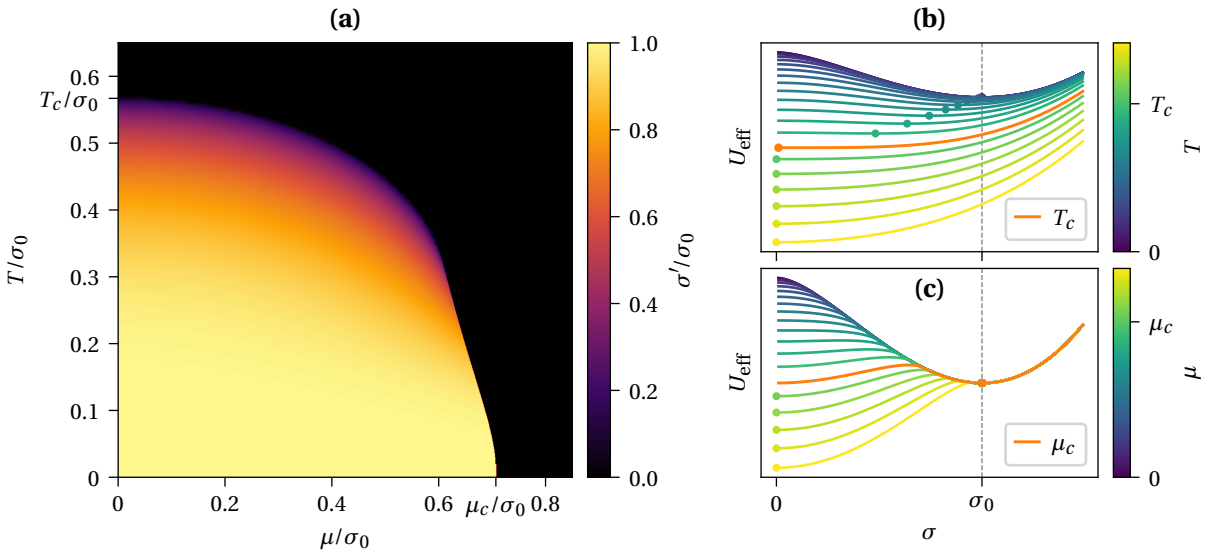

Figure 1.1: 1 + 1-dimensional GN in the large-N_f limit with restriction to homogeneous σ [2].
(a) The homogeneous phase diagram in the μ, T-plane. **(b)** The the evolution of the effective potential for various T and $\mu = 0$. **(c)** The evolution of the effective potential for various μ and $T = 0$. The dots indicate the minimum of the respective potential.

Inhomogeneous Phase Diagram

Without the restriction of the chiral condensate being constant in space, it was found that there is a third phase called *inhomogeneous phase* (IP) where σ' is a periodic oscillating function in space [3, 4]. Figure 1.2a shows this new phase diagram where the HBP/SP boundary up to the Lifshitz point is the same as in the homogeneous phase diagram. Following the Lifshitz point there is now a splitting of the phase boundaries with the IP emerging. The new HBP/IP boundary extends from the Lifshitz point to $(\mu/\sigma_0, T/\sigma_0) = (1/2\pi, 0) \approx (0.637, 0)$. The former boundary (green dashed line) is completely engulfed by the IP and all phase boundaries are second order now. In the IP, the oscillating chiral condensate is described by a combination of Jacobi elliptic functions and for increasing chemical potential the chiral condensate (compare Figure 1.2b)

1. morphs from a kink-antikink shape to a sin-like shape,
2. has an increasing frequency,
3. has a decreasing amplitude.

It is also found that the baryon density has its peak at the steepest descends of $\sigma'(x)$, i.e. its zeros. Therefore, the baryons seem to align with the oscillation and an increase in frequency of the oscillation means the introduction of an additional baryon. Thus, the inhomogeneous phase is interpreted as a crystal of baryons placed in fixed distances [24].

The special property of this phase is that the continuous translation symmetry realized in the action is broken to a subgroup as the condensate is only invariant under a transformation

$$\sigma'(x_0, x_1) = \sigma'(x_0, x_1 + \lambda), \tag{1.38}$$

where λ is the wave length of the oscillation. The breaking of this symmetry apparently contradicts the Coleman theorem, which states that a continuous symmetry cannot be spontaneously broken in $d \leq 2$

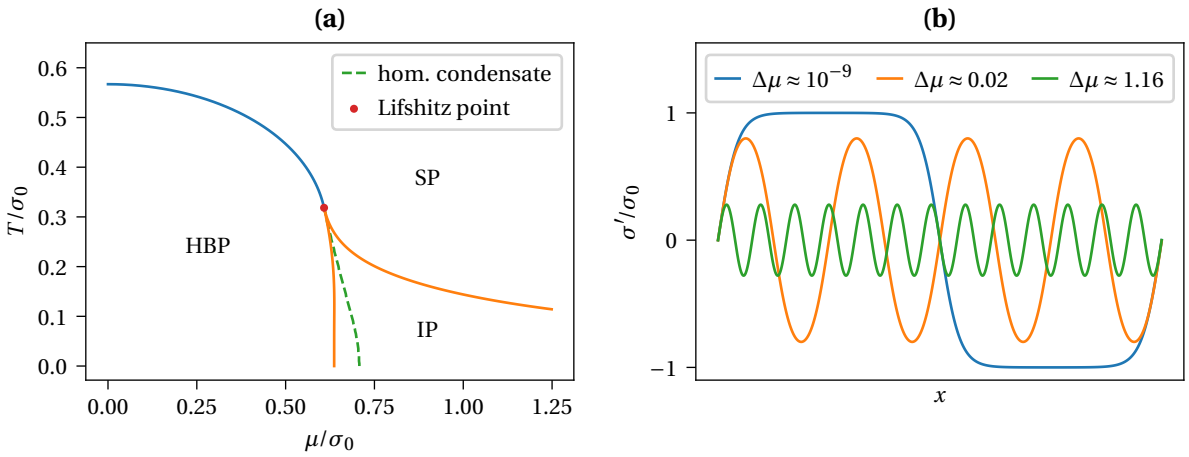

Figure 1.2: 1 + 1-dimensional GN in the large N_f limit [3, 4]. **(a)** The full phase diagram in the μ, T-plane. **(b)** The inhomogeneous condensate for various $\Delta\mu = (\mu - \mu_c)/\sigma_0$ and $T = 0$.

dimensions [25]. It is argued that this would produce massless Nambu-Goldstone bosons with a relativistic dispersion relation whose correlation functions have infrared divergences and thus cannot exist. This problem can be circumvented in the limit of $N_f \to \infty$ (see Ref. [26]), but the same argument does not hold at finite N_f, so it is not obvious if the breaking of translational invariance would still occur. If the Goldstone boson decouples completely or it has a non-relativistic dispersion relation (which does not produce infrared divergences in the correlation function), it could be that there still occurs true spontaneous symmetry breaking of the translation symmetry. For a more in-depth discussion of this matter we refer to Ref. [16].

2 The Gross-Neveu Model on the Lattice

2.1 Spacetime Discretization

As a first step, we introduce a hypercubic $d+1$-dimensional spacetime lattice Γ of size $V = \prod_{\mu=0}^{d} L_\mu$, where d is the number of spatial dimensions and L_μ denotes the physical extent in μ-direction. This lattice is defined by a set of discrete spacetime points

$$\Gamma \coloneqq \{\boldsymbol{x} = \boldsymbol{n}a \,|\, \boldsymbol{n} \in \Lambda\} \quad \text{with} \quad \Lambda \coloneqq \left\{\boldsymbol{n} = (n_0, n_1, \dots, n_d)^\mathsf{T} \,|\, n_\mu \in \left\{0, 1, \dots, N_\mu - 1\right\}\right\}, \tag{2.1}$$

where the lattice points are equidistantly distributed with a lattice spacing a and N_μ is the number of lattice sites in μ-direction.[1] The physical extent of the lattice in μ-direction is then $L_\mu = aN_\mu$. The discretized spacetime of the lattice clearly breaks the Poincaré symmetry down to discrete translations and rotations. The fields $\sigma, \psi, \bar{\psi}$ only occur on these discrete lattice sites, which causes the measure in the path integral $\mathcal{Z}$ to be of finite dimensions. It is then written as

$$\mathcal{D}\sigma = \prod_{\boldsymbol{x}\in\Gamma} \mathrm{d}\sigma(\boldsymbol{x}). \tag{2.2}$$

A discretization of spacetime leads to an upper bound on the physical momenta $\boldsymbol{k}$ on these lattices, which is illustrated by considering a plane wave

$$\exp(\mathrm{i}\boldsymbol{k}\cdot\boldsymbol{x}) = \exp(\mathrm{i}\boldsymbol{k}\cdot\boldsymbol{n}a),$$

where a shift $\boldsymbol{k} \to \boldsymbol{k} + \boldsymbol{e_\nu} 2\pi/a$ does not change the expression since $\boldsymbol{n} \in \mathbb{N}^{d+1}$, and $\boldsymbol{e_\nu}$ denotes the unit vector in ν direction. Therefore, all relevant momenta are located within the first Brillouin zone $[-\pi/a, \pi/a)$.[2]

A finite lattice discretizes the available physical momenta and requires us to impose boundary conditions. These are (anti)periodic boundary conditions i.e. $f(\boldsymbol{x} + \boldsymbol{e_\mu} L_\mu) = \exp(\mathrm{i}2\pi\eta_\mu) f(\boldsymbol{x})$ (no summation over μ), where $\eta_\mu = 0, 1/2$ for periodic and antiperiodic boundary conditions in μ-direction respectively. This is again demonstrated with a plane wave

$$\exp\left[\mathrm{i}\boldsymbol{k}\cdot(\boldsymbol{n} + N_\mu \boldsymbol{e_\mu})a\right] = \exp\left(\mathrm{i}2\pi\eta_\mu\right)\exp(\mathrm{i}\boldsymbol{k}\cdot\boldsymbol{n}a) \quad \Rightarrow \quad k_\mu a N_\mu = 2\pi\left(\tilde{n}_\mu + \eta_\mu\right) \text{ with } \tilde{n}_\mu \in \mathbb{Z}, \tag{2.3}$$

which shows that only certain momenta are allowed.

Both of these conditions combined define the reciprocal lattice $\tilde{\Gamma}$ containing the available physical mo-

[1] Elements of Γ are referred to as "lattice points" with standard symbols $\boldsymbol{x}, \boldsymbol{y}, \boldsymbol{z}$ and elements of Λ are referred to as "lattice sites" with standard symbols $\boldsymbol{n}, \boldsymbol{m}, \boldsymbol{r}, \boldsymbol{s}$.

[2] An asymmetric choice of the first Brillouin Zone as $[0, 2\pi/a)$ would also be correct as long as the continuum limit is not taken.

menta[3]

$$\tilde{\Gamma} := \left\{ \boldsymbol{k} = \frac{\boldsymbol{p}}{a} \,\middle|\, \boldsymbol{p} \in \tilde{\Lambda} \right\}, \tag{2.4}$$

with

$$\tilde{\Lambda} := \left\{ \boldsymbol{p} = (p_0, p_1, \dots, p_d)^\mathsf{T} \,\middle|\, p_\mu = \frac{2\pi\left(\tilde{n}_\mu + \eta_\mu\right)}{N_\mu}\ ,\ \tilde{n}_\mu \in \left\{ -N_\mu/2, -N_\mu/2+1, \dots, N_\mu/2-1 \right\} \right\}, \tag{2.5}$$

where we assume N_μ to be even. The set for $\tilde{n}_\mu$ is obtained by a shift of the set in the asymmetric first Brillouin zone $[0, 2\pi/a)$, where $\tilde{n}_\mu \in \{0, 1, \dots, N_\mu - 1\}$. For an even lattice extent, one shifts this by $-N_\mu/2$ to obtain the set in Eq. (2.5). An odd lattice extent would need a different shift to obtain a Brillouin zone of $[-\pi/a, \pi/a)$ and fulfill $\tilde{n}_\mu \in \mathbb{Z}$. This shift depends on η_μ and is $-(N_\mu - 1)/2$ for $\eta_\mu = 0$ and $-(N_\mu + 1)/2$ for $\eta_\mu = 1/2$. Odd lattices will not be viable for our investigation (as illustrated in Section 2.2.2); therefore, we defined $\tilde{\Lambda}$ for even lattice extents.

From here on, we consider a $1+1$-dimensional spacetime with periodic boundary conditions as default. For fermions we impose antiperiodic boundary conditions in the 0-direction i.e. setting $\eta_0 = 1/2$ for fermionic momenta[4].

In order to recover the continuum physics we have to perform the *continuum limit*, i.e. $a \to 0$ while keeping the volume of the lattice V constant.

2.2 Naive Discretization of Fermions

Also subject to discretization is the derivative operator that acts on the spinors in the Dirac Operator $\partial_\mu \psi(\boldsymbol{x})$. Just as the spacetime discretization itself, a derivative discretization might explicitly break symmetries that are realized in the theory we are interested in. These can be recovered in the continuum, but it might be challenging to do so and therefore it is advisable to choose a discretization that preserves the symmetries that are important to the investigation. There are various different methods to discretize this single derivative in the Dirac operator. The following discussion focuses on the so-called *naive* derivative discretization. In Section 2.3.1 we briefly remark on other discretizations used for the GN model.

We start by considering the Taylor expansion of the fermion fields for space time points in distance a

$$\psi\left(\boldsymbol{x} + a\boldsymbol{e_\mu}\right) = \psi(\boldsymbol{x}) + \partial_\mu \psi(\boldsymbol{x})\, a + \partial_\mu^2 \psi(x)\, a^2 + \mathcal{O}(a^3), \tag{2.6a}$$

$$\psi\left(\boldsymbol{x} - a\boldsymbol{e_\mu}\right) = \psi(\boldsymbol{x}) - \partial_\mu \psi(\boldsymbol{x})\, a + \partial_\mu^2 \psi(\boldsymbol{x})\, a^2 + \mathcal{O}(a^3). \tag{2.6b}$$

Taking the difference of Eq. (2.6a) and Eq. (2.6b) yields

$$\psi\left(\boldsymbol{x} + a\boldsymbol{e_\mu}\right) - \psi\left(\boldsymbol{x} - a\boldsymbol{e_\mu}\right) = 2\partial_\mu \psi(\boldsymbol{x})\, a + \mathcal{O}(a^3) \Rightarrow \partial_\mu \psi(\boldsymbol{x}) = \frac{\psi\left(\boldsymbol{x} + a\boldsymbol{e_\mu}\right) - \psi\left(\boldsymbol{x} - a\boldsymbol{e_\mu}\right)}{2a} + \mathcal{O}(a^2), \tag{2.7}$$

[3] Similarly to the lattice sites and points we make a distinction between elements of $\tilde{\Gamma}$ calling them "physical momenta" with standard symbol $\boldsymbol{k}$ and elements of $\tilde{\Lambda}$ calling them just "momenta" with standard symbols $\boldsymbol{p}, \boldsymbol{q}$.

[4] To ease notation we refrain from introducing two different sets for fermionic and bosonic momenta and instead set $\boldsymbol{\eta}$ according to the context, e.g. in the expression $\tilde{\psi}(\boldsymbol{k})$ it should be clear that $\boldsymbol{k}$ is a fermionic physical momentum that belongs to $\tilde{\Gamma}$ with $\eta_0 = 1/2$

which defines the naive discretization

$$\partial_\mu \psi(\boldsymbol{x}) \to \partial_\mu^{\text{naive}} \psi(a\boldsymbol{n}) = \frac{\psi\left(a\left(\boldsymbol{n}+\boldsymbol{e_\mu}\right)\right) - \psi\left(a\left(\boldsymbol{n}-\boldsymbol{e_\mu}\right)\right)}{2a} = \sum_{\boldsymbol{m}\in\Lambda} \frac{\delta_{\boldsymbol{n}+\boldsymbol{e_\mu},\boldsymbol{m}} - \delta_{\boldsymbol{n}-\boldsymbol{e_\mu},\boldsymbol{m}}}{2a} \psi(a\boldsymbol{m}) = \sum_{\boldsymbol{m}\in\Lambda} D_\mu^{\text{naive}}(\boldsymbol{n}|\boldsymbol{m})\, \psi(a\boldsymbol{m}), \quad (2.8)$$

with a discretization error of a^2. Therefore, we recover the derivative in the continuum limit of $a \to 0$, albeit we might retain unphysical lattice artifacts. In order to get a better understanding of the continuum limit, we consider the momentum representation of the naive derivative operator[5]

$$\tilde{D}_\mu^{\text{naive}}\left(\boldsymbol{p}|\boldsymbol{q}\right) = \frac{1}{|\Lambda|} \sum_{\boldsymbol{n},\boldsymbol{m}\in\Lambda} \mathrm{e}^{-\mathrm{i}\boldsymbol{n}a\cdot\boldsymbol{p}/a} D_\mu^{\text{naive}}(\boldsymbol{n}|\boldsymbol{m})\, \mathrm{e}^{\mathrm{i}\boldsymbol{m}a\cdot\boldsymbol{q}/a} = \delta_{\boldsymbol{p},\boldsymbol{q}} \frac{\mathrm{i}}{a} \sin\left(q_\mu\right) = \delta_{\boldsymbol{p},\boldsymbol{q}} \tilde{D}_\mu^{\text{naive}}\left(\boldsymbol{q}\right), \quad (2.9)$$

where $|\Lambda| = \prod_\mu N_\mu$ is the number of lattice sites and $\delta_{\boldsymbol{p},\boldsymbol{q}}$ compares the integers $\tilde{\boldsymbol{n}}$ that belong to the momenta $\boldsymbol{p}$ and $\boldsymbol{q}$. Next we obtain the naively discretized free Dirac operator $\tilde{Q}_{\text{free}}^{\text{naive}}\left(\boldsymbol{p}\right)$ by contracting this derivative with the Dirac matrices γ_μ and by a subsequent inversion, the propagator

$$\tilde{Q}_{\text{free}}^{\text{naive}}\left(\boldsymbol{p}\right) = \tilde{\not{D}}^{\text{naive}}\left(\boldsymbol{p}\right) + m = \frac{\mathrm{i}}{a}\gamma_\mu \sin\left(p_\mu\right) + m, \quad \left(\tilde{Q}_{\text{free}}^{\text{naive}}\right)^{-1}(\boldsymbol{p}) = \frac{m - \mathrm{i}\,\gamma_\mu \sin\left(p_\mu\right)/a}{m^2 + \sin\left(p_\mu\right)^2/a^2}, \quad (2.10)$$

where m would be the mass of the considered free fermion. For fixed physical momentum $\boldsymbol{k}$ this assumes the well known form in the continuum limit

$$\lim_{a\to 0} \left(\tilde{Q}_{\text{free}}^{\text{naive}}\right)^{-1}(\boldsymbol{k}a) = \lim_{a\to 0} \frac{m - \mathrm{i}/a\,\gamma_\mu \sin\left(k_\mu a\right)}{m^2 + \left(\sin\left(k_\mu a\right)/a\right)^2} = \frac{m - \mathrm{i}\gamma_\mu k_\mu}{m^2 + \boldsymbol{k}^2} = \tilde{Q}_{\text{free}}^{-1}(\boldsymbol{k}). \quad (2.11)$$

2.2.1 Fermion Doublers in the Naive Discretization

When we consider a massless fermion, i.e. setting $m = 0$, the continuum propagator has one pole at $\boldsymbol{p} = 0$. This gives rise to one physical fermion, since only the momenta in the vicinity of a pole contribute as the others are suppressed in the path integral. The naive propagator, however, has multiple poles that remain in the continuum limit. These occur at the edges of the first Brillouin zone whenever the components of the momenta are either 0 or $\pm\pi$. This circumstance is simply due to the fact that the sin has a zero at π which is not present for the linear dispersion relation of the continuum (compare with Figure 2.1). We label the poles as

$$\boldsymbol{A} := (0,0)^\mathsf{T}, \quad \boldsymbol{B} := (0,\pm\pi)^\mathsf{T}, \quad \boldsymbol{C} := (\pm\pi,0)^\mathsf{T}, \quad \boldsymbol{D} := (\pm\pi,\pm\pi)^\mathsf{T}. \quad (2.12)$$

The poles $\boldsymbol{B},\boldsymbol{C},\boldsymbol{D}$ also give rise to additional fermions, which are called *doublers*. Therefore, we end up with 4 (in D spacetime dimensions 2^D) fermions per "original" fermion flavor. We refer to the fermions belonging to one original flavor as *sub-flavors* of that flavor (this includes the original physical fermion). The momentum region in the vicinity of a pole is associated to the respective sub-flavor. We divide the first Brillouin zone into these regions $R(\boldsymbol{X})$ that we define as squares of edge length π with the corresponding

[5] Note that this representation is actually obtained by taking the FT of the spinors in $\bar{\psi}D\psi$.

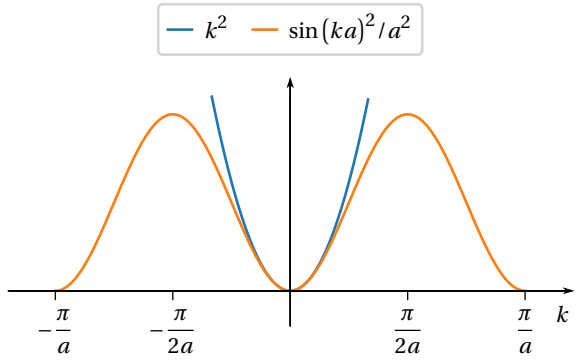

Figure 2.1: The 1-dimensional part of the denominator of the massless continuum in Eq. (2.11) and naive propagator in Eq. (2.10).

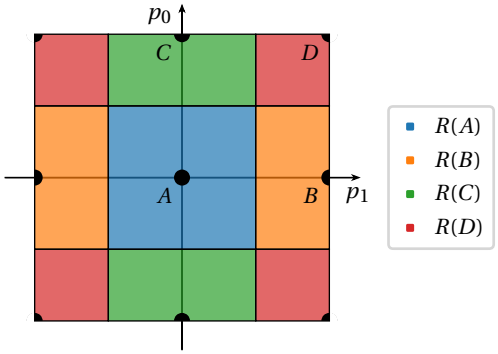

Figure 2.2: The 2-dimensional momentum domain divided in the sub-flavor regions.

pole $\boldsymbol{X}$ in the center (see Figure 2.2).[6] The regions $R(\boldsymbol{X})$ define the set

$$\mathfrak{R} := \{R(\boldsymbol{A}),\, R(\boldsymbol{B}),\, R(\boldsymbol{C}),\, R(\boldsymbol{D})\}. \tag{2.13}$$

With this in mind we introduce a new notation of a sub-flavor index that depends on the momentum of the spinor, thus relabeling the original spinors as

$$\psi_a\big((\boldsymbol{p}+\boldsymbol{X})/a\big) \to \psi_a^X\big(\boldsymbol{p}/a\big), \tag{2.14}$$

where $\boldsymbol{X}$ denotes one of the poles associated to a certain sub-flavor.

Even though one could expect, that the doublers behave just like additional flavors, they have a deficiency, which is revealed when considering the naively discretized action of a single free massless fermion approaching the continuum limit.[7] We consider it in momentum space and apply the new notation of regions to it

$$\begin{aligned}
&\sum_{\boldsymbol{p}\in\tilde{\Lambda}} \bar{\psi}\big(\boldsymbol{p}/a\big)\, \tilde{\not{D}}^{\text{naive}}\big(\boldsymbol{p}\big)\, \psi\big(\boldsymbol{p}/a\big) \\
&\quad= \sum_{R(\boldsymbol{X})\in\mathfrak{R}} \sum_{\boldsymbol{p}\in R(\boldsymbol{X})} \bar{\psi}\big(\boldsymbol{p}/a\big)\, \tilde{\not{D}}^{\text{naive}}\big(\boldsymbol{p}\big)\, \psi\big(\boldsymbol{p}/a\big) \\
&\quad= \frac{\mathrm{i}}{a}\Big[\sum_{\boldsymbol{p}\in R(\boldsymbol{A})} \bar{\psi}\big(\boldsymbol{p}/a\big)\, \gamma_\mu \sin(p_\mu)\, \psi\big(\boldsymbol{p}/a\big) + \sum_{\boldsymbol{p}\in R(\boldsymbol{B})} \bar{\psi}\big(\boldsymbol{p}/a\big)\, \gamma_\mu \sin(p_\mu)\, \psi\big(\boldsymbol{p}/a\big) \\
&\qquad + \sum_{\boldsymbol{p}\in R(\boldsymbol{C})} \bar{\psi}\big(\boldsymbol{p}/a\big)\, \gamma_\mu \sin(p_\mu)\, \psi\big(\boldsymbol{p}/a\big) + \sum_{\boldsymbol{p}\in R(\boldsymbol{D})} \bar{\psi}\big(\boldsymbol{p}/a\big)\, \gamma_\mu \sin(p_\mu)\, \psi\big(\boldsymbol{p}/a\big)\Big] \\
&\quad= \frac{\mathrm{i}}{a} \sum_{\boldsymbol{p}\in R(0)} \Big[\bar{\psi}^A\big(\boldsymbol{p}/a\big)\, \gamma_\mu \sin\Big(p_\mu + A_\mu\Big)\, \psi^A\big(\boldsymbol{p}/a\big) + \bar{\psi}^B\big(\boldsymbol{p}/a\big)\, \gamma_\mu \sin\Big(p_\mu + B_\mu\Big)\, \psi^B\big(\boldsymbol{p}/a\big) \\
&\qquad + \bar{\psi}^C\big(\boldsymbol{p}/a\big)\, \gamma_\mu \sin\Big(p_\mu + C_\mu\Big)\, \psi^C\big(\boldsymbol{p}/a\big) + \bar{\psi}^D\big(\boldsymbol{p}/a\big)\, \gamma_\mu \sin\Big(p_\mu + D_\mu\Big)\, \psi^D\big(\boldsymbol{p}/a\big)\Big]
\end{aligned}$$

[6] A more rigorous mathematical definition in D spacetime dimensions would make use of the infinity norm as $R(\boldsymbol{X}) = \{\boldsymbol{p}\in\tilde{\Lambda} : ||\boldsymbol{p}-\boldsymbol{X}||_\infty = \max\{|p_0 - X_0|, \ldots, |p_d - X_d|\} < \pi\}$.

[7] The following short discussion follows the arguments presented in [27].

$$\xrightarrow[\text{continuum}]{\text{approaching}} \approx \mathrm{i} \sum_{\boldsymbol{p}\in R(0)} \Big[\; \bar{\psi}^A(\boldsymbol{k})\, \gamma_\mu k_\mu\, \psi^A(\boldsymbol{k}) + \bar{\psi}^B(\boldsymbol{k})\, (\gamma_0 k_0 - \gamma_1 k_1)\, \psi^B(\boldsymbol{k}) \\ + \bar{\psi}^C(\boldsymbol{k})\, (-\gamma_0 k_0 + \gamma_1 k_1)\, \psi^C(\boldsymbol{k}) - \bar{\psi}^D(\boldsymbol{k})\, \gamma_\mu k_\mu\, \psi^D(\boldsymbol{k}) \Big], \tag{2.15}$$

where, in the last step, we used that only the momenta close to the poles contribute in the continuum limit and therefore expanded the sin functions for small momenta p_μ, and introduced the physical momentum $\boldsymbol{k} = \boldsymbol{p}/a$, which is fixed when taking the continuum limit. This reveals that the doublers have an incorrect momentum relation as their kinetic part features additional minus signs in contrast with the original fermion. This can, however, be remedied by a unitary linear transformation of the spinors

$$\bar{\chi} = \bar{\psi} P^\dagger, \quad \chi = P\psi, \quad P = \mathrm{diag}(\mathbb{1}, \gamma_0, \gamma_1, \gamma_0\gamma_1), \tag{2.16}$$

where P acts in sub-flavor space. By applying this transformation to Eq. (2.15) we flip the wrong signs and recover the standard kinetic term for all four sub-flavors within their respective region

$$\sum_{X=A}^{D} \sum_{\boldsymbol{p}\in R(0)} \bar{\chi}^X(\boldsymbol{p})\, \mathrm{i}\gamma_\mu p_\mu\, \chi^X(\boldsymbol{p}). \tag{2.17}$$

This transformation does not alter the action, since it is unitary and is merely a rewriting to conventional field coordinates.

The doubler phenomenon is subject of the well known Nielsen-Ninoyima theorem, which states that a fermion discretization that

1. has no doublers,
2. preserves chiral symmetry,
3. is local, i.e. its Fourier Transform exists and all its derivatives are continuous,
4. is translationally invariant,

cannot exist [28, 29, 30]. This in turn means that every lattice discretization has to drop one of these properties. The naive discretization violates, as shown, the first property in order to fulfill the rest. The preservation of the chiral symmetry is, of course, very important for our investigation in Chapter 3 and therefore naive fermions are an acceptable choice.

2.2.2 Even and Odd Lattice Extents N_μ

One is restricted to even lattice extents when using the naive derivative. The reason why is evident when we consider the available momenta in μ-direction on the lattice. Odd lattice extents causes momenta at the edge of the first Brillouin zone that are associated to antiperiodic/ periodic boundary conditions to behave like momenta associated to periodic/ antiperiodic boundary conditions, i.e. for initially antiperiodic boundary conditions there is now a momentum $p_\mu = -\pi$ and for initially periodic boundary conditions there is no momentum $p_\mu = -\pi$ anymore. Therefore, the boundary condition for the doublers in this direction is flipped (compare Figure 2.3). [8] The reason can be understood purely on a geometric level as it is just not possible to distribute an odd number of points in the appropriate way.

[8] Note that the same effect also occurs in an asymmetric first Brillouin zone and is not the result of the shift of momenta.

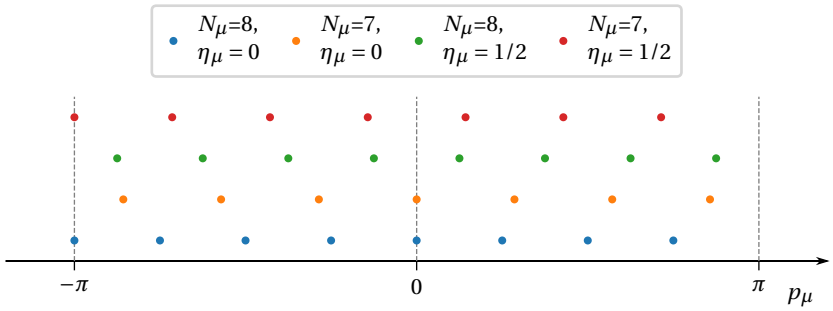

Figure 2.3: Momenta $p_\mu \in \tilde{\Lambda}$ for even/odd lattice extents $N_\mu = 8, 7$ each for periodic/antiperiodic boundary conditions $\eta_\mu = 0, 1/2$.

The presence of one direction of finite extent with antiperiodic boundary conditions effectively serves as an infrared regulator for the determinant of the Dirac operator. Having a fermion that has periodic boundary conditions in all directions removes this regulating feature. This introduces zero eigenmodes and consequently a divergence of the action. A detailed description of the effects on the GN action can be found in Appendix C.2 (Note that this description depends on the discussion in the next section).

2.2.3 Introduction of the Chemical Potential

Although an introduction of a chemical potential happens on the level of the path integral, we want to discuss at this point how it is introduced in the naive discretization. A linear introduction of the chemical potential into the action as $\gamma_0 \mu$ as in the continuum in Eq. (1.3) seems sensible. However, doing so leads to a divergent energy density in the continuum limit. To prevent this, it is common practice when using the naive discretization (but also Wilson or staggered fermions for example) to introduce the chemical potential in an exponential to the time derivative (see Ref. [31]) as

$$D_0^{\text{naive}}(\boldsymbol{n}|\boldsymbol{m}) = \frac{\delta_{\boldsymbol{n}+\boldsymbol{e}_\mu,\boldsymbol{m}}\, \mathrm{e}^{\mu a} - \delta_{\boldsymbol{n}-\boldsymbol{e}_\mu,\boldsymbol{m}}\, \mathrm{e}^{-\mu a}}{2a} \tag{2.18}$$

and in momentum space

$$D_0^{\text{naive}}(\boldsymbol{p}|\boldsymbol{q}) = \delta_{\boldsymbol{p},\boldsymbol{q}} \frac{\mathrm{i}}{a} \sin\left(q_0 - \mathrm{i}\mu a\right). \tag{2.19}$$

There are also alternative approaches that show that the emerging divergence when using the linear term is not an artifact of the lattice discretization but rather a continuum effect. The partition function can then be corrected by adding a μ-dependent constant [32].

The introduction of the chemical potential does not alter the previous discussion about the deficiency of the doublers as it picks up the same wrong signs in the kinetic term.

2.3 Discretization of the 1 + 1-Dimensional Gross-Neveu Action

Applying the previously discussed naive discretization *naively* without further modifications to the GN action from Eq. (1.11) results in a discretized action as

$$\begin{aligned} S_\sigma[\bar\psi,\psi,\sigma] &= \int \mathrm{d}^2\boldsymbol{x}\left(\sum_{b=1}^{N_\mathrm{f}} \bar\psi_b(\boldsymbol{x})\, Q_\mathrm{GN}(x)\, \psi_b(\boldsymbol{x}) + \frac{N_\mathrm{f}}{2\lambda}\sigma(\boldsymbol{x})^2\right) \\ \xrightarrow{\text{NN disc.}}\ S_\sigma^\mathrm{NN}[\bar\psi,\psi,\sigma] &= \frac{N_\mathrm{f}\,a^2}{2\lambda}\sum_{\boldsymbol{n}\in\Lambda}\sigma(\boldsymbol{n}a)^2 + a^2\sum_{\boldsymbol{n},\boldsymbol{m}\in\Lambda}\sum_{b=1}^{N_\mathrm{f}/4}\bar\psi_b(\boldsymbol{m}a)\left(\mathbb{D}^\mathrm{naive}(\boldsymbol{m}|\boldsymbol{n}) + \delta_{\boldsymbol{m},\boldsymbol{n}}\sigma(\boldsymbol{n}a)\right)\psi_b(\boldsymbol{n}a) \\ &= \frac{N_\mathrm{f}}{2\lambda}\sum_{\boldsymbol{n}\in\Lambda}\sigma(\boldsymbol{n})^2 + \sum_{\boldsymbol{n},\boldsymbol{m}\in\Lambda}\sum_{b=1}^{N_\mathrm{f}/4}\bar\psi_b(\boldsymbol{m})\left(\mathbb{D}^\mathrm{naive}(\boldsymbol{m}|\boldsymbol{n}) + \delta_{\boldsymbol{m},\boldsymbol{n}}\sigma(\boldsymbol{n})\right)\psi_b(\boldsymbol{n}), \end{aligned} \tag{2.20}$$

which we call the *naive naive* (NN) discretization. We rescaled the number of fermions N_f by a factor of $1/4$ in the sum to account for the doublers such that N_f is the total number of fermions that are present—including doublers. Note that we absorbed the lattice spacing into the field variable to obtain only dimensionless quantities as

$$a\sigma\to\sigma,\quad a^{1/2}\psi\to\psi,\quad a^{1/2}\bar\psi\to\bar\psi,\quad a\mathbb{D}^\mathrm{naive}(m|n)\to\mathbb{D}^\mathrm{naive}(m|n),\quad a\mu\to\mu \tag{2.21}$$

and now use elements of Λ instead of elements of Γ as arguments of the fields. The same applies to objects of momentum space. We continue the discussion for the remainder of this chapter in these variables and only switch back in Section 2.3.3.

The NN discretization leaves the interaction term $\bar\psi\sigma\psi$ unchanged, which results in a wrong continuum limit. To show this, we start by considering the discretized interaction in Fourier space

$$\begin{aligned} \sum_{b=1}^{N_\mathrm{f}/4}\sum_{\boldsymbol{n}\in\Lambda}\bar\psi_b(\boldsymbol{n})\,\sigma(\boldsymbol{n})\,\psi_b(\boldsymbol{n}) &= \frac{1}{|\Lambda|^{3/2}}\sum_{b=1}^{N_\mathrm{f}/4}\sum_{\boldsymbol{n}\in\Lambda}\sum_{\boldsymbol{p},\boldsymbol{q},\boldsymbol{p}'\in\tilde\Lambda}\tilde{\bar\psi}_b(\boldsymbol{p})\,\mathrm{e}^{-\mathrm{i}\boldsymbol{p}\cdot\boldsymbol{n}}\tilde\sigma(\boldsymbol{p}')\,\mathrm{e}^{\mathrm{i}\boldsymbol{p}'\cdot\boldsymbol{n}}\mathrm{e}^{\mathrm{i}\boldsymbol{q}\cdot\boldsymbol{n}}\tilde\psi_b(\boldsymbol{q}) \\ &= \frac{1}{|\Lambda|^{3/2}}\sum_{b=1}^{N_\mathrm{f}/4}\sum_{\boldsymbol{p},\boldsymbol{q},\boldsymbol{p}'\in\tilde\Lambda}|\Lambda|\,\delta_{\boldsymbol{p}',\boldsymbol{p}-\boldsymbol{q}}\,\tilde{\bar\psi}_b(\boldsymbol{p})\,\tilde\sigma(\boldsymbol{p}')\,\tilde\psi_b(\boldsymbol{q}) \\ &= \frac{1}{\sqrt{|\Lambda|}}\sum_{b=1}^{N_\mathrm{f}/4}\sum_{\boldsymbol{p},\boldsymbol{q}\in\tilde\Lambda}\tilde{\bar\psi}_b(\boldsymbol{p})\,\tilde\sigma(\boldsymbol{p}-\boldsymbol{q})\,\tilde\psi_b(\boldsymbol{q}), \end{aligned} \tag{2.22}$$

where $\boldsymbol{p}'$ is a bosonic momentum with periodic boundary conditions in all directions, i.e. $\boldsymbol{\eta}=\boldsymbol{0}$. Rewriting this in terms of sub-flavors yields a vector-matrix-vector multiplication as

$$\frac{1}{\sqrt{|\Lambda|}}\sum_{b=1}^{N_\mathrm{f}/4}\sum_{\boldsymbol{p},\boldsymbol{q}\in R(\boldsymbol{0})}\begin{pmatrix}\tilde{\bar\psi}_b^A(\boldsymbol{p})\\ \tilde{\bar\psi}_b^B(\boldsymbol{p})\\ \tilde{\bar\psi}_b^C(\boldsymbol{p})\\ \tilde{\bar\psi}_b^D(\boldsymbol{p})\end{pmatrix}^\mathsf{T}\begin{pmatrix}\sigma^A & \sigma^B & \sigma^C & \sigma^D\\ \sigma^B & \sigma^A & \sigma^D & \sigma^C\\ \sigma^C & \sigma^D & \sigma^A & \sigma^B\\ \sigma^D & \sigma^C & \sigma^B & \sigma^A\end{pmatrix}\begin{pmatrix}\tilde\psi_b^A(\boldsymbol{q})\\ \tilde\psi_b^B(\boldsymbol{q})\\ \tilde\psi_b^C(\boldsymbol{q})\\ \tilde\psi_b^D(\boldsymbol{q})\end{pmatrix}, \tag{2.23}$$

where $\sigma^X=\sigma(\boldsymbol{p}-\boldsymbol{q}+\boldsymbol{X})$. By applying the transformation P of Eq. (2.16), we obtain the interaction with

fermions with the correct dispersion relation

$$\frac{1}{\sqrt{|\Lambda|}}\sum_{b=1}^{N_\mathrm{f}/4}\sum_{\boldsymbol{p},\boldsymbol{q}\in R(\mathbf{0})}\begin{pmatrix}\tilde{\bar{\chi}}_b^A(\boldsymbol{p})\\ \tilde{\bar{\chi}}_b^B(\boldsymbol{p})\\ \tilde{\bar{\chi}}_b^C(\boldsymbol{p})\\ \tilde{\bar{\chi}}_b^D(\boldsymbol{p})\end{pmatrix}^{\mathsf{T}}\begin{pmatrix}\sigma^A & \sigma^B\gamma_0 & \sigma^C\gamma_1 & \sigma^D\gamma_0\gamma_1\\ \sigma^B\gamma_0 & \sigma^A & \sigma^D\gamma_0\gamma_1 & \sigma^C\gamma_1\\ \sigma^C\gamma_1 & \sigma^D\gamma_0\gamma_1 & \sigma^A & \sigma^B\gamma_0\\ \sigma^D\gamma_0\gamma_1 & \sigma^C\gamma_1 & \sigma^B\gamma_0 & \sigma^A\end{pmatrix}\begin{pmatrix}\tilde{\chi}_b^A(\boldsymbol{q})\\ \tilde{\chi}_b^B(\boldsymbol{q})\\ \tilde{\chi}_b^C(\boldsymbol{q})\\ \tilde{\chi}_b^D(\boldsymbol{q})\end{pmatrix}, \tag{2.24}$$

which shows the flaws of the NN discretization. The first one is that the off-diagonal elements contain gamma matrices even though the GN model features only scalar interactions. The second one is that these off-diagonal inter sub-flavor interactions are unwanted all together. There is no flavor mixing in the GN model and therefore also sub-flavors should not mix.

To get rid of the incorrect interactions in Eq. (2.24), a modification of the interaction term in Fourier space to suppress inter sub-flavor coupling is appropriate, where effectively only the diagonal terms contribute. To do so, we introduce a modification $\tilde{F}(\boldsymbol{p}-\boldsymbol{q})$ into the interaction

$$\frac{1}{\sqrt{|\Lambda|}}\sum_{b=1}^{N_\mathrm{f}/4}\sum_{\boldsymbol{p},\boldsymbol{q}\in\tilde{\Lambda}}\tilde{\bar{\psi}}_b(\boldsymbol{p})\,\tilde{F}(\boldsymbol{p}-\boldsymbol{q})\,\tilde{\sigma}(\boldsymbol{p}-\boldsymbol{q})\,\tilde{\psi}_b(\boldsymbol{q}), \tag{2.25}$$

where $\tilde{F}(\boldsymbol{p})$ should be 1 for momenta of region $R(\boldsymbol{A})$ and vanish for momenta $\boldsymbol{p}$ belonging to momentum regions other than $R(\boldsymbol{A})$. This modification suppresses the incorrect off-diagonal interactions while not altering the desired diagonal interactions.

We consider two possible choices for $\tilde{F}$

$$\tilde{W}(\boldsymbol{p}) = \tilde{w}(p_0)\times\tilde{w}(p_1) \qquad \text{with} \qquad \tilde{w}(p_\mu) = (1+\cos(p_\mu))/2 \tag{2.26}$$

and

$$\tilde{H}(\boldsymbol{p}) = \tilde{h}(p_0)\times\tilde{h}(p_1) \qquad \text{with} \qquad \tilde{h}(p_\mu) = \Theta(\pi/2-|p_\mu|), \tag{2.27}$$

with the 1-dimensional functions $\tilde{h},\tilde{w}$ depicted in Figure 2.4a. The function $\tilde{H}$ fulfills the requirements exactly, whereas $\tilde{W}$ is 1 only at $\boldsymbol{A}$ and vanishes only at the edges of the first Brillouin zone. In the continuum limit, however, solely momenta close to the poles contribute, where $\tilde{W}$ is in fair agreement with the requirements. We also have to consider the properties of H and W—the FTs of $\tilde{H}$ and $\tilde{W}$— since we want to formulate the discretization in position space. The non-zero entries of H clearly span the whole lattice as is illustrated by its 1-dimensional component h (compare Figure 2.4b). On the contrary W uses only a couple of close lattice sites and is therefore numerically advantageous. Thus, we use $\tilde{W}$ to modify the interaction and obtain as expression of the interaction in position space

$$\sum_{b=1}^{N_\mathrm{f}}\sum_{\boldsymbol{n},\boldsymbol{m}\in\Lambda}\bar{\psi}_b(\boldsymbol{n})\,\delta_{\boldsymbol{n},\boldsymbol{m}}\left(\sum_{\boldsymbol{r}}\frac{W(\boldsymbol{n}|\boldsymbol{r})}{\sqrt{|\Lambda|}}\,\sigma(\boldsymbol{r})\right)\psi_b(\boldsymbol{m}), \tag{2.28}$$

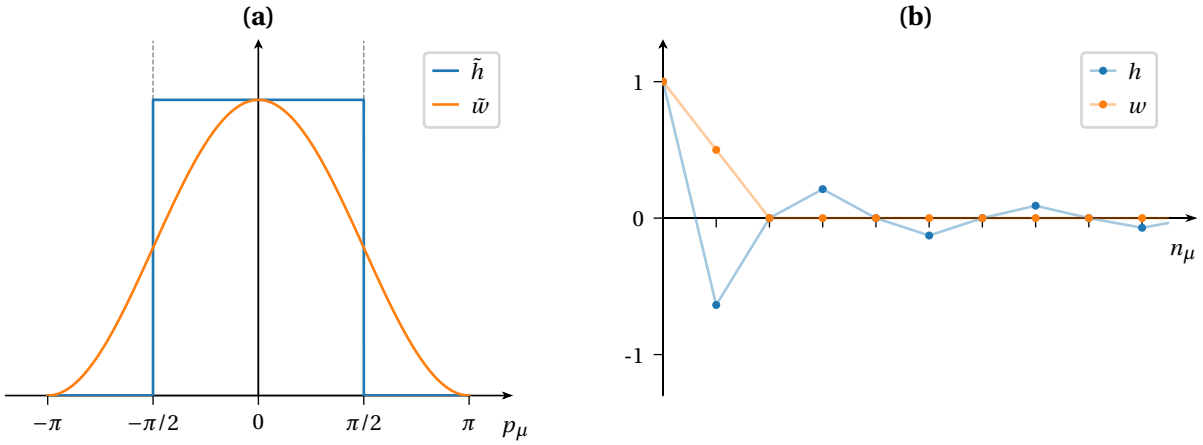

Figure 2.4: The functions $\tilde{h}, \tilde{w}, h, w$ on a lattice with infinite volume **(a)** $\tilde{h}$ and $\tilde{w}$. **(b)** h and w.

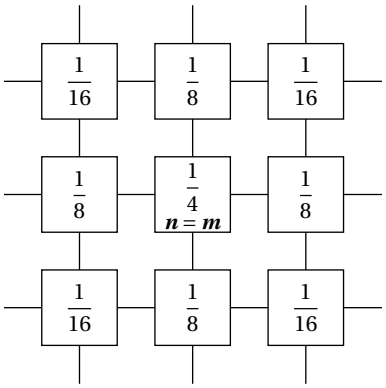

Figure 2.5: Visualization of $W(\boldsymbol{n}|\boldsymbol{m})/\sqrt{|\Lambda|}$ as a grid of neighboring lattice sites.

where $W(\boldsymbol{n}|\boldsymbol{r})$ is the FT of $\tilde{W}(\boldsymbol{p}-\boldsymbol{q})$ given by (compare Figure 2.5)

$$\frac{W(\boldsymbol{n}|\boldsymbol{r})}{\sqrt{|\Lambda|}} = \frac{1}{16}\Big[4\delta_{\boldsymbol{n},\boldsymbol{r}} + 2\Big(\delta_{\boldsymbol{n}+\boldsymbol{e}_0,\boldsymbol{r}} + \delta_{\boldsymbol{n}-\boldsymbol{e}_0,\boldsymbol{r}} + \delta_{\boldsymbol{n}+\boldsymbol{e}_1,\boldsymbol{r}} + \delta_{\boldsymbol{n}-\boldsymbol{e}_1,\boldsymbol{r}}\Big) + \delta_{\boldsymbol{n}+\boldsymbol{e}_0+\boldsymbol{e}_1,\boldsymbol{r}} + \delta_{\boldsymbol{n}-\boldsymbol{e}_0-\boldsymbol{e}_1,\boldsymbol{r}} + \delta_{\boldsymbol{n}-\boldsymbol{e}_0+\boldsymbol{e}_1,\boldsymbol{r}} + \delta_{\boldsymbol{n}+\boldsymbol{e}_0-\boldsymbol{e}_1,\boldsymbol{r}}\Big]. \tag{2.29}$$

The action with this discretization of the interaction term is then

$$S_\sigma^{\mathrm{ND}}[\bar{\psi},\psi,\sigma] = \frac{N_\mathrm{f}}{2\lambda}\sum_{\boldsymbol{n}\in\Lambda}\sigma(\boldsymbol{n})^2 + \sum_{\boldsymbol{n},\boldsymbol{m}\in\Lambda}\sum_{b=1}^{N_\mathrm{f}/4}\bar{\psi}_b(\boldsymbol{m})\left[\not{D}^{\mathrm{naive}}(\boldsymbol{m}|\boldsymbol{n}) + \delta_{\boldsymbol{m},\boldsymbol{n}}\left(\sum_{\boldsymbol{r}} W(\boldsymbol{n}|\boldsymbol{r})\,\sigma(\boldsymbol{r})\right)\right]\psi_b(\boldsymbol{n}), \tag{2.30}$$

which we call the *naive distributed* (ND) discretization.

One can also arrive at this action by starting in the FF formulation of the action and altering the interaction term so that there is no sub-flavor mixing. This is again achieved by introducing $\tilde{W}$ into the interaction term in momentum space as

$$\sum_{b,c=1}^{N_\mathrm{f}/4}\sum_{\boldsymbol{p},\boldsymbol{q},\boldsymbol{p}',\boldsymbol{q}'\in\tilde{\Lambda}}\delta_{\boldsymbol{q}-\boldsymbol{p},\boldsymbol{p}'-\boldsymbol{q}'}\left[\tilde{\bar{\psi}}_b(\boldsymbol{p})\,\tilde{W}(\boldsymbol{p}-\boldsymbol{q})\,\tilde{\psi}_b(\boldsymbol{q})\right]\left[\tilde{\bar{\psi}}_c(\boldsymbol{p}')\,\tilde{W}(\boldsymbol{p}'-\boldsymbol{q}')\,\tilde{\psi}_c(\boldsymbol{q}')\right]. \tag{2.31}$$

We transform this back to position space

$$\sum_{\boldsymbol{n}\in\Lambda}\left(\sum_{b=1}^{N_\mathrm{f}/4}\sum_{\boldsymbol{r}\in\Lambda}\bar{\psi}_b(\boldsymbol{r})\,\frac{W(\boldsymbol{r}|\boldsymbol{n})}{\sqrt{|\Lambda|}}\,\psi_b(\boldsymbol{r})\right)\left(\sum_{c=1}^{N_\mathrm{f}/4}\sum_{\boldsymbol{s}\in\Lambda}\bar{\psi}_c(\boldsymbol{s})\,\frac{W(\boldsymbol{s}|\boldsymbol{n})}{\sqrt{|\Lambda|}}\,\psi_c(\boldsymbol{s})\right) \tag{2.32}$$

and apply the HS transformation as

$$\exp\left\{\frac{g^2}{2}\sum_{\boldsymbol{n}\in\Lambda}\left(\sum_{b=1}^{N_\mathrm{f}/4}\sum_{\boldsymbol{r}\in\Lambda}\bar{\psi}_b(\boldsymbol{r})\;W(\boldsymbol{r}|\boldsymbol{n})\,\psi_b(\boldsymbol{r})\right)^2\right\}$$
$$=\int\mathscr{D}\sigma\,\exp\left\{-\sum_{\boldsymbol{n}\in\Lambda}\left[\frac{1}{2g^2}\sigma(\boldsymbol{n})^2+\sum_{b=1}^{N_\mathrm{f}/4}\bar{\psi}_b(\boldsymbol{n})\,\left(\sum_{r}W(\boldsymbol{n}|\boldsymbol{r})\,\sigma(\boldsymbol{r})\right)\psi_b(\boldsymbol{n})\right]\right\}. \tag{2.33}$$

The complete resulting action is again $S_\sigma^{\mathrm{ND}}[\bar{\psi},\psi,\sigma]$ as in Eq. (2.30).

2.3.1 Other Fermion Discretizations

We briefly review other fermion discretizations that have been used successfully in FF theories. This is by no means a thorough introduction to their concepts, but serves to put the discussion of naive fermions into perspective. Among those other fermion discretizations are:

- The WILSON discretization of fermions that introduces an artificial mass term to the Dirac operator in order to lift the poles at the edges of the first Brillouin zone and thus gets rid of the doublers (see, e.g. Ref. [33] for an introduction). This, however, breaks chiral symmetry explicitly. It has been shown for the GN model that the chiral symmetry can be recovered in the continuum limit by fine-tuning the bare mass and two additional introduced bare couplings [34].

- The SLAC discretization [35, 36], whose basic idea is that the FT of the derivative is just the discretized momenta (compare with Ref. [18] for additional information), i.e.

  $$\mathscr{F}_{\boldsymbol{x}}[\partial_\mu^{\mathrm{SLAC}}\psi(\boldsymbol{x})](\boldsymbol{k})=\mathrm{i}k_\mu\mathscr{F}_{\boldsymbol{x}}[\psi(\boldsymbol{x})](\boldsymbol{k})\qquad\text{with}\qquad\boldsymbol{k}\in\tilde{\Gamma}.$$

  This causes a jump at the edge of the Brillouin zone and therefore violates the locality property in the Nilsen-Ninomiya theorem, which poses severe problems when using it in gauge theories [37]. These problems do not arise in theories without local gauge invariance (see Ref. [38]) including four fermion theories, where the SLAC discretization has been used successfully (see, e.g. Refs. [27, 39, 40, 16]).

- The STAGGERED discretization (also called Kogut-Susskind fermions) achieves a minimal doubling of fermions by distributing its degrees of freedom in a particular way on sub-lattices (for an introduction we refer to textbooks such as Refs. [33, 41]); thereby, it breaks parts of the chiral symmetry. In order to achieve the right continuum limit when discretizing the GN model, one has to distribute the bosonic field σ in a similar manner as for the ND discretization. A distribution of σ on a dual lattice as plaquettes was proposed and used in finite N_f simulations in Ref. [27] and also applied successfully in a large-N_f investigation of inhomogeneous condensates in Ref. [42].

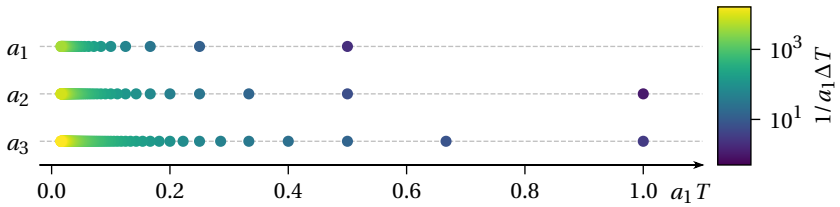

Figure 2.6: The sequence of available temperatures for three different lattice spacings $a_1 = 2\,a_2 = 4\,a_3$ up to a minimum temperature $a_1 T = 1/64$. The colorbar indicates the density of available temperatures by $1/\Delta T$ in units of a_1, where $\Delta T = T_{n+1} - T_n$ and T_{n+1}, T_n are consecutive temperatures in the sequence of temperatures.

2.3.2 Setting the Temperature

As introduced in Section 1.1, the temperature is the inverse size of the temporal direction $T = 1/L_0$. On the lattice the size of the temporal direction is $L_0 = N_0\,a$ and consequently a discrete quantity for finite a. Figure 2.6 shows a comparison of the available temperatures and their density for three different lattice spacings. This illustrates, that we are restricted to a non-constant temperature resolution and overall the resolution becomes finer as we approach the continuum. One can also conclude that it is not possible to truly reach $T = 0$, which is the region of our interest, and approaching it becomes increasingly costly for smaller lattice spacings. These circumstances also have a noticeable impact on our ability to resolve effects at high temperatures in the Lattice simulations as for example a phase transition.

2.3.3 Scale Setting and the Lattice Spacing a

Within this short subsection, we denote previously introduced dimensionless quantities (combinations of quantity X with the lattice spacing a) as $\hat{X}$. The formulation of the simulated equations is in dimensionless quantities and therefore the observables are as well. As these have no physical meaning we re-express (just as in the discussion in Section 1.3.3) all dimensionful quantities in units of

$$\sigma_0 = \langle|\sigma|\rangle\Big|_{(\mu,T)=(0,0)}, \tag{2.34}$$

i.e. the expectation value of the chiral condensate at chemical potential and temperature zero. As example the chemical potential will then be given as μ/σ_0. Note that this ratio also corresponds to the ratio of the previously defined dimensionless quantities

$$\frac{\hat{\mu}}{\hat{\sigma}_0} = \frac{\mu\,a}{\sigma_0\,a} = \frac{\mu}{\sigma_0}. \tag{2.35}$$

This way of scale setting also allows us to recover the lattice spacing a as

$$\hat{\sigma}_0 = a\sigma_0 \Rightarrow a = \hat{\sigma}_0/\sigma_0, \tag{2.36}$$

where $\hat{\sigma}_0$ would be the value measured in a simulation and σ_0 is what would be physically measured.

As we saw in Section 2.3.2, a lattice setup with $T = 0$ is not possible. Therefore, σ_0 is approximated on a lattice by $\langle|\sigma|\rangle|_{(\mu,T)=(0,T)}$ with a sufficiently small temperature $T \approx 0$. We can control the lattice spacing by varying λ, where smaller values of λ correspond to smaller lattice spacings.

2.3.4 The Large-N_f Limit as a Testbed of the Discretization

As a first check for the quality of the employed discretization, we show that it reproduces the large-N_f results discussed in Section 1.3.3.

Homogeneous Phase Diagram

We start with the homogeneous phase diagram for which it is quite easy to minimize the lattice regularized effective action (some notes on doing so can be found in Appendix C.1). Note that for the homogeneous phase diagram it does not matter which discretization (NN or ND) of the interaction term is used, since the distribution function drops out of the eigenvalues for homogeneous σ (see Appendix A.2).

Figure 2.7a depicts the continuum calculated phase boundary and the phase boundaries for different lattice spacing in the (μ, T)-plane. The lattice results converge to the continuum boundary for decreasing lattice spacing, thereby validating the naive discretization in the homogeneous case.

Inhomogeneous Phase Diagram

A calculation of the inhomogeneous phase diagram is also possible, albeit more difficult and numerically more expensive. In this case, the action is not independent of the discretization of the interaction term (NN or ND). Figure 2.7b shows results from Ref. [46] obtained with a hybrid discretization, where the 0-direction is discretized with a finite mode approach (see Refs. [43, 44, 45, 46]) as the condensate is expected to be translationally invariant in the 0-direction and the 1-direction is discretized with the 1-dimensional analogon of the NN (inserting $\tilde{h}$ for the spatial momenta in the interaction term) and ND discretization [46]. A stability analysis of the SP is used to produce the results, which only allows for the phase boundaries of the SP to be found.

Both discretizations approach the continuum result for decreasing lattice spacing. Though they approach the inhomogeneous phase boundary from "opposite sides" and with different rates. The small inhomogeneous phase for ND can be explained by the nature of the discretization. High frequencies of the auxiliary field σ are suppressed in this discretization and therefore inhomogeneous condensates with high frequencies are suppressed. With decreasing lattice spacing this suppression only affects physical momenta of increasing magnitude, which causes the phase boundary to converge to the continuum boundary. It is not yet fully understood why the NN discretization apparently has the same continuum limit in the large-N_f limit. The jagged phase boundary lines are a result of the finite box in which these lattice calculations take place. Since we impose periodic boundary conditions, an integer number of wavelengths have to fit into the box and thus not all wavelengths of the inhomogeneous condensate can be realized. This results in the visible jumps of the phase boundary (compare to Ref. [42]).

2.4 Lattice Monte Carlo Simulations

This section briefly introduces the concepts needed to compute the lattice discretized path integral and observables. For an introduction to Monte Carlo simulations in the context of lattice field theory we refer to the textbooks [18, 33, 41], for the simulation of dynamical fermions to the lecture notes in Ref. [47] and for the general analysis of Monte Carlo Data to Ref. [48]. The discussion in this section is a condensation of the information in these references. For details on the implementation of these methods in the code that was used in the simulations, we refer to the doctoral theses of B. Wellegehausen [49] and D. Schmidt [50].

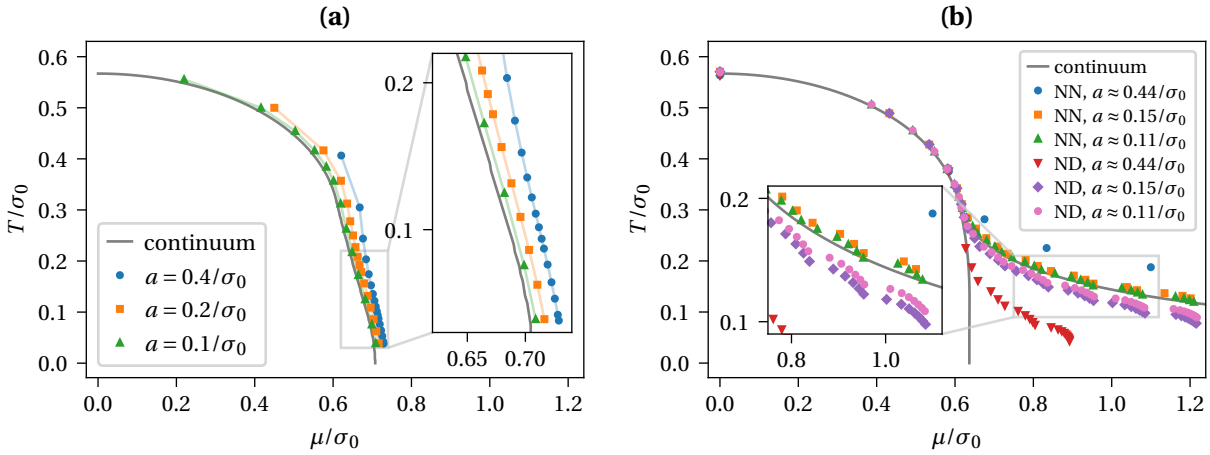

Figure 2.7: Phase boundaries of the $1+1$-dimensional GN model in the large-N_f limit using various discretization schemes. **(a)** The homogeneous phase diagram in the continuum (grey line) and on the lattice with $L_1 = 25.6/\sigma_0$ for different lattice spacings a. **(b)** The inhomogeneous phase diagram in the continuum (grey lines) and on the lattice with $L_1 \approx 22.2/\sigma_0$ for different lattice spacings and discretizations NN and ND [46].

2.4.1 Pseudofermions

In the path integral ,we can integrate out the fermion bilinear in the action Eq. (2.30) as

$$\begin{aligned}\mathcal{Z} &= \int \mathscr{D}\sigma\, \mathscr{D}\bar{\psi}\, \mathscr{D}\psi \quad \exp\left[-\sum_{\boldsymbol{n}\in\Lambda}\left(\frac{N_\mathrm{f}}{2\lambda}\sigma^2(\boldsymbol{n}) + \sum_{b=1}^{N_\mathrm{f}} \bar{\psi}_b(\boldsymbol{n})\, Q_\mathrm{GN}^\mathrm{ND}(\boldsymbol{n})\, \psi_b(\boldsymbol{n})\right)\right] \\ &= \int \mathscr{D}\sigma\, \det(Q)^{N_\mathrm{f}} \exp\left[-\sum_{\boldsymbol{n}\in\Lambda}\frac{N_\mathrm{f}}{2\lambda}\sigma^2(\boldsymbol{n})\right]. \end{aligned} \tag{2.37}$$

This determinant is possibly difficult and/or expensive to evaluate. To circumvent this, we apply a method called *pseudofermions* [51, 52]. The idea is that we raise the determinant back up in the exponent by a reverse integration of a bosonic field. To do so we rewrite $\det(Q)^{N_\mathrm{f}}$ [9] as

$$\det(Q)^{N_\mathrm{f}} = \det\left(Q^\dagger Q\right)^{N_\mathrm{f}/2} = \det(M)^{N_\mathrm{f}/2} = \det\left(M^{-q}\right)^{-N_\mathrm{PF}}, \tag{2.38}$$

where we used in the first step that $\det Q$ is real, introduced the new Matrix $M = Q^\dagger Q$ and variables q, N_PF as $N_\mathrm{f}/2 = qN_\mathrm{PF}$. We rewrite $\det Q$ in Eq. (2.37) according to Eq. (2.38) and apply a reversed Gaussian integration of a complex bosonic field ϕ

$$\mathcal{Z} = \int \mathscr{D}\sigma\, \det\left(M^{-q}\right)^{-N_\mathrm{PF}} \exp\left(-\sum_{\boldsymbol{n}\in\Lambda}\frac{N_\mathrm{f}}{2\lambda}\sigma^2(\boldsymbol{x})\right) = \int \mathscr{D}\sigma\, \mathscr{D}\phi^\dagger\, \mathscr{D}\phi\, \mathrm{e}^{-S_\mathrm{PF}[\sigma,\phi^\dagger,\phi]}, \tag{2.39}$$

[9] We omit the superscript "ND" in the following section and consider $Q_\mathrm{GN} \equiv Q_\mathrm{GN}^\mathrm{ND}$. The section is, of course, valid for the NN discretization as well.

where the positive definiteness of M is a necessary condition for the Gaussian integral to converge, which is ensured by its definition as $Q^\dagger Q$, and

$$S_{\mathrm{PF}}[\sigma,\phi^\dagger,\phi] = -\sum_{\boldsymbol{n}\in\Lambda}\left(\frac{N_\mathrm{f}}{2\lambda}\sigma^2(\boldsymbol{n}) + \sum_{b=1}^{N_{\mathrm{PF}}}\phi_b^\dagger(\boldsymbol{n})\,M^{-q}\,\phi_b(\boldsymbol{n})\right). \tag{2.40}$$

The bosonic fields $\phi^\dagger,\phi$ are the aforementioned pseudofermions, which have the same degrees of freedom as the fermion fields $\bar\psi$ and ψ. The number of pseudofermions is arbitrary and the appropriate choice depends on numerical aspects [49]. We choose $N_{\mathrm{PF}} = N_\mathrm{f}$ and thus $q = 1/2$ for all simulations.

2.4.2 Monte Carlo Method

A Monte Carlo method is, in general, a computational algorithm that relies on repeated random samples to obtain numerical results. For example, integrals can be computed using Monte Carlo techniques. We draw N samples of the domain of integration A and evaluate the integrand f at these samples. For an infinite number of samples N, the true value of the integral I is the average of the function samples

$$I = \int_A \mathrm{d}x f(x) = \lim_{N\to\infty}\frac{1}{N}\sum_{n=1}^{N} f(x_n), \tag{2.41}$$

where x_n are uniformly distributed random samples in A. If we take N to be finite, the error is $\propto 1/\sqrt{N}$. This method is also applicable to high dimensional integrals like the path integral $\mathcal{Z}$ in Eq. (2.39), where the domain of integration contains all possible field configurations σ.[10] However, its integrand, the weight $\exp(-S)$, is often sharply peaked and for large parts of the domain of integration ≈ 0. Due to the high dimensionality, we might not sample the peaks and therefore severely underestimate the integral.

The method of *importance sampling* samples the field configuration not uniformly random but according to the probability distribution density

$$P_{\mathrm{eq}}(\sigma) = \mathrm{e}^{-S[\sigma]}/\mathcal{Z}. \tag{2.42}$$

Therefore it primarily samples the configurations with a large contribution, which enables us to use a small set of configurations to approximate the integral. Note that $\exp(-S)$ has to be real and positive in order for Eq. (2.42) to be interpreted as a probability weight. This is often spoiled by the determinant of the fermion operator that is complex in some theories, e.g. in QCD at finite baryon chemical potential. This is the infamous *sign-problem*. Fortunately, the $1+1$-dimensional GN model has a real fermion determinant for finite chemical potential as shown in Appendix A.1. Moreover, we restrict the simulations to an even number of flavors to ensure that the eigenvalues always occur in pairs and thus guarantee the determinant to be positive.

[10] Pseudofermions are not simulated, but are dealt with differently. Therefore our discussion of the generation of field configurations is restricted to σ.

Markov Chains

In practice, these field configurations are generated in a *Markov chain*. This is a stochastic process, that builds a sequence of field configurations, where the next configuration is generated from the previous one

$$\ldots \xrightarrow{T(\sigma_{n-1}|\sigma_n)} \sigma_n \xrightarrow{T(\sigma_n|\sigma_{n+1})} \sigma_{n+1} \xrightarrow{T(\sigma_{n+1}|\sigma_{n+2})} \sigma_{n+2} \xrightarrow{T(\sigma_{n+2}|\sigma_{n+3})} \ldots,$$

where σ_n denotes n-th state of the Markov chain and $T(\sigma_n|\sigma_{n+1})$ is the transition probability to go from configuration σ_n to σ_{n+1}. These transition probabilities have to meet three properties:

1. $T(\sigma|\sigma') \geq 0 \;\; \forall\, \sigma, \sigma'$,
2. $\sum_{\sigma'} T(\sigma|\sigma') = 1 \;\; \forall\, \sigma$,
3. $\sum_{\sigma'} T(\sigma|\sigma') P_{\text{eq}}(\sigma) = P_{\text{eq}}(\sigma') \;\; \forall\, \sigma'$.

The first property ensures that we can reach any possible configuration in a single step of the chain, which is called *strong ergodicity*. The second property assures that all probabilities are normalized and the third property characterizes an important property of the Markov chain: The probability distribution P_{eq} is a fix point of the Markov chain, which means that any amount of subsequent steps in the chain continue to follow this desired *equilibrium* distribution. This is important, as this ensures that we can use the configurations in the estimation of the integral and, later, observables.

The beginning of the chain is an arbitrary initial configuration σ_I with the initial distribution $P_I(\sigma) = \delta(\sigma - \sigma_I)$. Each subsequent step of the Markov process changes this distribution and it can be shown (see Ref. [41]) that the deviation from the equilibrium distribution P_{eq} decreases with each step. After a number of steps N^{therm}, which we call *thermalization* time, the chain approximately follows the equilibrium distribution.

The generation of the configurations is done by an algorithm, which, in principle, has to fulfill properties 1–3 of the Markov chain transition probabilities. In practice, the first property is often exchanged for the weaker *relaxed ergodicity*

$$T^m(\sigma|\sigma') \geq 0 \qquad \text{with} \qquad m \ll N, \tag{2.43}$$

where $T^m(\sigma|\sigma')$ is the transition probability to go from state σ to σ' with m intermediate steps. This demands that the chain is able to eventually reach any state and the number of intermediate steps m should be small compared to the total number of generated configurations.

The third property is usually met by requiring the algorithm to fulfill the stronger condition of *detailed balance*

$$P_{\text{eq}}(\sigma)\, T(\sigma|\sigma') = P_{\text{eq}}(\sigma')\, T(\sigma'|\sigma) \;\; \forall\, \sigma, \sigma', \tag{2.44}$$

which yields the third property by summing it over σ' and using property 2.

Rational Hybrid Monte Carlo Algorithm

A particularly efficient algorithm for the simulation of dynamical fermions (as they are in our simulations) is the *rational Hybrid Monte Carlo* (rHMC) algorithm and we start by introducing the regular HMC algorithm. Contrary to local algorithms like the Metropolis-Hastings algorithm, the HMC updates the whole lattice simultaneously. This is significantly more effective for fermionic systems as updates require an

evaluation of M^{-q}, which is expensive to calculate. It's basic principle is the reformulation of a QFT path integral to a partition function known from classical mechanics, where the former time dimension is a space dimension as well. The fields are then evolved via Hamiltonian equations of motion in a fictitious *Molecular dynamics* time.

We introduce a conjugate momenta field π to the bosonic field σ in the path integral $\mathcal{Z}$

$$\mathcal{Z} = \int \mathcal{D}\sigma\, \mathcal{D}\phi^\dagger\, \mathcal{D}\phi\, \mathrm{e}^{S_{\mathrm{PF}}[\sigma,\phi^\dagger,\phi]} = \int \mathcal{D}\sigma\, \mathcal{D}\pi\, \mathcal{D}\phi^\dagger\, \mathcal{D}\phi\, \mathrm{e}^{-H[\sigma,\pi,\phi^\dagger,\phi]}, \tag{2.45}$$

where the conjugate momentum does not change the expectation value of observables as its contribution is canceled by the normalization $1/\mathcal{Z}$ and

$$H[\sigma,\pi,\phi^\dagger,\phi] := \frac{1}{2}\sum_{\boldsymbol{n}\in\Lambda} \pi(\boldsymbol{n})^2 + S_{\mathrm{PF}}[\sigma,\phi^\dagger,\phi]. \tag{2.46}$$

The corresponding Hamiltonian *equations of motion* (EOM) are

$$\dot{\pi}(\boldsymbol{n}) = -\frac{\partial H}{\partial \sigma(\boldsymbol{n})} = -\frac{\partial S}{\partial \sigma(\boldsymbol{n})}, \qquad \dot{\sigma}(\boldsymbol{n}) = \frac{\partial H}{\partial \pi(\boldsymbol{n})} = \pi(\boldsymbol{n}), \tag{2.47}$$

where the time derivatives are taken with respect to the Molecular dynamics time.

One update, i.e. a step in the Markov chain with the HMC algorithm, can then be characterized in four steps:

Step 1: *Generation of the pseudofermion fields $\phi^\dagger, \phi$.*

As mentioned earlier, the pseudofermions are a numerical "trick" to evaluate the determinant of Q. We do not evolve them like σ and π, but rather draw them at the beginning of the update according to their distribution

$$P_{\mathrm{PF}}(\phi) \propto \exp\left(-\sum_{\boldsymbol{n}\in\Lambda}\sum_{b=1}^{N_{\mathrm{PF}}} \phi_b^\dagger(\boldsymbol{n})\, M^{-q}\, \phi_b(\boldsymbol{n})\right) = \exp\left(\sum_{\boldsymbol{n}\in\Lambda}\sum_{b=1}^{N_{\mathrm{PF}}} \xi_b^\dagger(\boldsymbol{n})\, \xi_b(\boldsymbol{n})\right), \tag{2.48}$$

with $\xi = M^{-q/2}\phi$ and therefore $\phi = M^{q/2}\xi$. Consequently, we can generate the pseudofermion fields by drawing complex, Gaussian distributed random fields ξ and a subsequent multiplication with $M^{q/2}$.

Step 2: *Generation of the conjugate momentum field π.*

At each step, we draw new conjugate momenta, which puts the system on different energy shells along which we evolve the fields. The momenta are drawn according to a Gaussian distribution

$$P_\pi(\pi) \propto \exp\left(-\frac{1}{2}\sum_{\boldsymbol{n}\in\Lambda} \pi^\dagger(\boldsymbol{n})\pi(\boldsymbol{n})\right). \tag{2.49}$$

This is not an arbitrary choice as it is required that

$$P_\pi(\pi)\mathrm{e}^{-S} \propto \mathrm{e}^{-H}$$

to fulfill the condition of detailed balance (see Ref. [18] for a short proof). This in turn requires P_π to be a Gaussian distribution for the Hamiltonian that we chose to construct in Eq. (2.46).

Step 3: *Integration of the fields σ, π via the EOM in Eq. (2.47) for a period of time τ, which yields the new field configurations σ', π'.*

An exact integration of these EOM preserves the energy (and therefore also H), as it is a constant of motion, and generates new field configurations σ', π'. In the actual simulations, the integration is a numeric procedure, which has an error. The integration is done with a symplectic algorithm such as the *leap-frog* algorithm (see Ref. [47] for a discussion of other more sophisticated algorithms), which ensures the time reversibility and the area preservation in phase space that are properties needed for the detailed balance condition. The integrator evolves the EOM in N time steps $\delta\tau$ with $N \cdot \delta\tau = \tau$. Note that in each time step of the integration, one has to calculate S and therefore also M^{-q}, which can become very costly with increasing lattice size.

Step 4: *Accepting the new configuration σ' as the next configuration in the Markov chain with the probability*

$$A(\sigma, \pi \to \sigma', \pi') = \min\left(1, \exp\left(H[\sigma, \pi, \phi^\dagger, \phi] - [\sigma', \pi', \phi^\dagger, \phi]\right)\right). \tag{2.50}$$

If the configuration is rejected, the last configuration σ is considered to be the new configuration in the chain.

The acceptance step corrects for the numerical error in the integration and ensures that the detailed balance condition is met.

The difference between rHMC and HMC is that instead of calculating M^{-q} exactly, it is only rationally approximated in the rHMC algorithm by

$$M^{-s} \approx \alpha_0 \sum_{r=1}^{N_R} \alpha_r (M + \beta_r)^{-1}, \tag{2.51}$$

where $s \in \mathbb{Q}$, N_R is the total number of terms, that determine the accuracy of the approximation and the coefficients $\alpha_0, \alpha_r, \beta_r$, which are constant throughout the simulation, can be computed with the Remez algorithm [53] . It is sufficient to use a less accurate approximation in the integration step, since the resulting additional error in the integration is also compensated in the acceptance step where M^{-q} is approximated to machine precision. Note that a less accurate approximation decreases the acceptance rate of configurations and therefore might increase computational cost. The parameters of the algorithm such as the accuracy of the rational approximation or step size of the EOM integrator $\delta\tau$ are usually chosen so that acceptance rates are $\approx 80\%$. The rational approximation is also used to calculate $M^{q/2}$, which is needed for the generation of the pseudofermion fields.

Estimation of Observables

We can estimate the path integral expectation value $\langle O \rangle$ of an observable $O[\sigma]$ as

$$\langle O \rangle \approx \overline{O} = \frac{1}{N} \sum_{n=1}^{N} O[\sigma_n], \tag{2.52}$$

where $\overline{O}$ is the estimator for the expectation value $\langle O \rangle$ and σ_n are the generated field configurations after the thermalization time. The estimator itself is again a random variable that would have different values if we perform the same simulation again. For N uncorrelated generated configurations σ_n used in the

calculation of $\overline{O}$, we can estimate this statistical error of the estimation as

$$\varepsilon_{\overline{O}} = \sqrt{\frac{\sigma^2_{\overline{O}}}{N}}, \tag{2.53}$$

with the variance estimator

$$\sigma^2_{\overline{O}} = \frac{1}{N-1}\sum_{n=1}^{N}\left(O[\sigma_n] - \overline{O}\right)^2. \tag{2.54}$$

The configurations are obviously not uncorrelated since the algorithm generates new configurations based on the previous configuration. This effect is called *autocorrelation*. The time it takes the system to "forget" the information of a past configuration is the *autocorrelation time* τ_O and depends on the considered observable. This quantity can be measured and enters the error of our estimate as

$$\varepsilon_{\overline{O}} = \sqrt{\frac{\sigma^2_{\overline{O}} \cdot \tau_O}{N}} = \sqrt{\frac{\sigma^2_{\overline{O}}}{N_{\text{eff}}}}, \tag{2.55}$$

where N_{eff} is the number of effective configurations, i.e. uncorrelated configurations.

We can also remove the correlation of the data by *binning*, where we divide the N measurements $O[\sigma_n]$ into M bins of size $2\tau_O$ and calculate their mean values. The mean values of the bins are then used as a new set of uncorrelated data of size M.

Jackknife Error

The previous calculation of errors does not hold for observables O that are functions of the expectation value of another observable X,

$$O = f(\langle X \rangle). \tag{2.56}$$

We could either try and propagate the error, which is not always possible, or use a technique like the *Jackknife* method. This method is used to estimate the error of derived quantities like O for uncorrelated data sets of size N. Therefore, we have to ensure that the data set is uncorrelated, e.g. by binning. The idea of the Jackknife method is that we calculate O on subsets of our data from which a single configuration of the original data has been removed and observe how much the value of O varies. We start by calculating the *Jackknife estimators*

$$O^J_n = f\left(X^J_n\right) \qquad \text{with} \qquad X^J_n = \frac{1}{N-1}\sum_{\substack{m=1 \\ m\neq n}}^{N} X_m, \tag{2.57}$$

where X_m is the measured quantity X on the m-th configuration. We can now estimate the variance of the Jackknife estimators

$$\sigma^2_{\overline{O}^J} = \frac{N-1}{N}\sum_{n=1}^{N}\left(O^J_n - \overline{O}^J\right)^2 \qquad \text{with} \qquad \overline{O}^J = \frac{1}{N}\sum_{n=1}^{N} O^J_n, \tag{2.58}$$

which we can use to estimate the error of O by $\varepsilon_O = \sigma_{\overline{O}^J}$. The error of all observables measured in the simulations as presented in Chapter 3 is given by the Jackknife method. Note that for $f = \langle X \rangle$ the Jackknife estimated error reduces to Eq. (2.53) and therefore gives the correct error for directly measured quantities.

3 The Phases of the Gross-Neveu Model in $1+1$ Dimensions at Finite N_f

This chapter discusses the observables required to detect the different phases of the GN model in $1+1$ dimensions and subsequently presents the obtained results. Note that we continue to use the term "phase" even though we will not be able to differentiate a found region in the (μ, T)-plane between a phase in a thermodynamic sense and a regime, that merely shows a distinct behavior.

3.1 Benchmark Model

From the investigation in Ref. [15], we do know that an inhomogeneous auxiliary field σ is already visible on a single configuration. Figure 3.1 shows a configuration from our own simulations that features a visible oscillation. By comparison of our configurations and the large-N_f phases, it seems appropriate to assume that deep within a phase the configurations are of similar shape as the large-N_f phases plus an additional distortion by noise. We devise a simple model ς that crudely mimics the generated configurations in our Monte Carlo simulation and is used to benchmark the ability of observables to detect the different phases of the GN. It also helps us to understand how different properties of the field σ influence the observables. The full model is then

$$\varsigma(\boldsymbol{x}) = A\cos\left(\frac{2\pi}{L_1}\big(x_1+\delta x\big)\big(q+\delta q\big)\right) + B\sigma_0 + \varepsilon\eta(\boldsymbol{x}), \tag{3.1}$$

where the parameters A, q, B, ϵ are fixed to values in order to mimic one of the three phases and the parameters $\eta(\boldsymbol{x}), \delta q, \delta x$ are randomly distributed variables that approximate the fluctuating character of a simulation. The parameters and their purposes are explained in Table 3.1. The parameter δx allows for a spatial shift of the oscillation. The occurrence and distribution of such a shift is connected to whether translation symmetry is spontaneously broken and therefore, we do not assume a distribution of the shift for now. We also expect that the frequency can slightly fluctuate between configurations. The benchmark model is obviously not able (and not intended) to mimic any sort of phase transition. Moreover, the Gaussian uncorrelated noise of η is most certainly too simplified as the noise is likely to be correlated in spacetime.

The behavior in the individual phases is obtained by setting either A or B or both to zero:

$$\varsigma_\mathrm{SP}(\boldsymbol{x}) = \varepsilon\eta(\boldsymbol{x}) \qquad \text{in the symmetric phase,} \tag{3.2a}$$

$$\varsigma_\mathrm{HBP}(\boldsymbol{x}) = B\sigma_0 + \varepsilon\eta(\boldsymbol{x}) \qquad \text{in the homogeneously broken phase,} \tag{3.2b}$$

$$\varsigma_\mathrm{IP}(\boldsymbol{x}) = A\cos\left(\frac{2\pi}{L_1}\big(x_1+\delta x\big)\big(q+\delta q\big)\right) + \varepsilon\eta(\boldsymbol{x}) \qquad \text{in the inhomogeneous phase.} \tag{3.2c}$$

As already explained, we want to use this benchmark model to predict the behavior and usefulness of observables that depend on σ. To do so, we carry out analytical calculations of these observables using ς

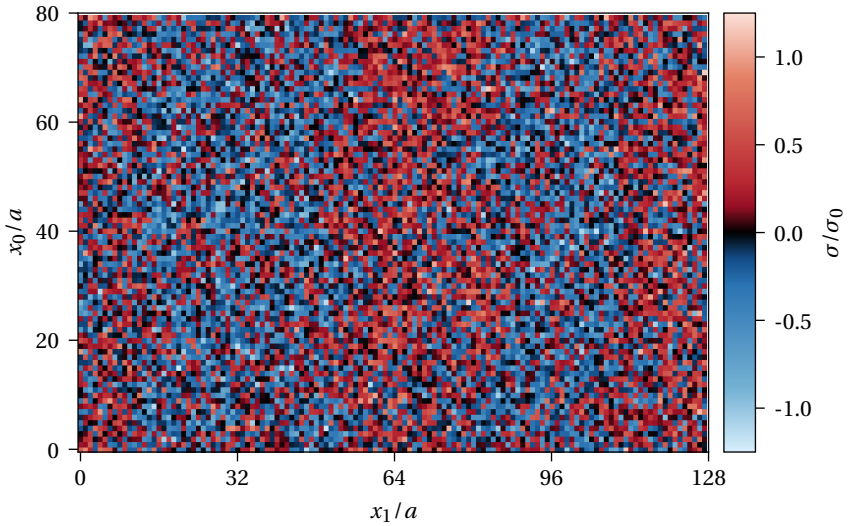

Figure 3.1: Typical configurations of the bosonic field σ generated in the simulations with parameters $N_\mathrm{f} = 8$, $a \approx 0.1253/\sigma_0$, $N_s = 128$ at $(\mu/\sigma_0, T/\sigma_0) \approx (0.59, 0.1)$.

Var.	Domain	Fix/random	Distribution	Purpose
ε	$\mathbb{R}$	fix	—	Controls the strength of the noise.
B	$\mathbb{R}$	fix	—	Sets the value of a homogeneous condensate.
A	$\mathbb{R}$	fix	—	Sets the amplitude of the oscillation.
q	$\mathbb{Z}$	fix	—	Sets the wave number of the oscillation.
$\eta(\boldsymbol{x})$	$\mathbb{R}$	random	$p_\eta(\eta(\boldsymbol{x})) = \frac{1}{\sqrt{2\pi}}\,\mathrm{e}^{-\eta(\boldsymbol{x})^2/2}$	Approximates the noise in the generated configurations.
δq	$\mathbb{Z}$	random	$p_q(\delta q) = \mathscr{C}^{-1}\,\mathrm{e}^{-\delta q^2/2\Delta q^2}$ $\mathscr{C} = \sum_{\delta q=-\infty}^{\infty} \mathrm{e}^{-\delta q^2/2\Delta q^2}$ [a]	Allows the wave number to fluctuate between configurations in integer steps.
δx	$\mathbb{R}$	random	$p_x(\delta x)$	Allows the oscillation to be shifted. No assumption about the distribution of the shift is made.

[a] As the model ς should only mimic the condensate deep inside a phase, we impose the condition $q \gg \Delta$.

Table 3.1: Variables of the model ς.

as input. Expectation values of observables $O[\sigma]$ are then computed as

$$\langle O_\varsigma \rangle = \int \mathscr{D}\eta \, p_\eta(\eta) \int_{-\infty}^{\infty} \mathrm{d}\delta x \, p_x(\delta x) \sum_{\delta q=-\infty}^{\infty} p_q(\delta q) \;\; O[\varsigma] \,, \tag{3.3}$$

where the subscript ς indicates that the observable is calculated with the model ς as input, $\mathscr{D}\eta = \prod_{\boldsymbol{x}\in\Gamma} \mathrm{d}\eta(\boldsymbol{x})$ and $p_\eta(\eta) = \prod_{\boldsymbol{x}\in\Gamma} p_\eta(\eta(\boldsymbol{x}))$. The detailed calculations of all observables within the model ς can be found in Appendix D.

3.2 Observables

3.2.1 The Chiral Condensate

The averaged chiral condensate

$$\langle \bar{\sigma} \rangle = \left\langle \frac{1}{|\Lambda|} \sum_{\boldsymbol{n}\in\Lambda} \sigma(\boldsymbol{n}) \right\rangle \tag{3.4}$$

is an interesting observable since a non-zero expectation value would signal the (homogeneous) breaking of chiral symmetry. On the lattice at finite N_f this observable needs to be modified. The reason for this can be illustrated when we restrict σ to being homogeneous and consider the effective potential from Figure 1.1. In the HBP, the action has two degenerate minima symmetric around the origin (for $T = 0$ at $\pm\sigma_0$). In an infinite volume, the energy barrier between these minima is infinitely large and thus enables spontaneous symmetry breaking, where $\langle\bar{\sigma}\rangle$ assumes a non-zero value. A lattice, however, is a finite volume and thus it only takes a finite amount of energy to pass the energy barrier between the two minima. In a Monte Carlo simulation, an ergodic algorithm will eventually sample configurations belonging to both minima. This can be seen in Figure 3.2, where the algorithm spends most of the time in the vicinity of the two minima of the action and occasionally quickly tunnels through the energy barrier that separates them. This would then lead to $\langle\bar{\sigma}\rangle \approx 0$. Therefore, it is advisable to use an observable independent of the sign of $\bar{\sigma}$ like $\langle|\bar{\sigma}|\rangle$ or $\langle\bar{\sigma}^2\rangle$. We use the latter, since it greatly simplifies the results of analytic calculations for the model ς and define

$$\Sigma^2 = \frac{\left\langle \bar{\sigma}^2 \right\rangle}{\sigma_0^2}. \tag{3.5}$$

This observable yields for the different phases in the model ς (the corresponding calculation is found in Appendix D.2)

$$\Sigma^2_{\varsigma_{\mathrm{SP}}} = \frac{\varepsilon^2}{|\Lambda|\sigma_0^2} \qquad \text{in the SP,} \tag{3.6a}$$

$$\Sigma^2_{\varsigma_{\mathrm{HBP}}} = B^2 + \frac{\varepsilon^2}{|\Lambda|\sigma_0^2} \qquad \text{in the HBP,} \tag{3.6b}$$

$$\Sigma^2_{\varsigma_{\mathrm{IP}}} = \frac{\varepsilon^2}{|\Lambda|\sigma_0^2} \qquad \text{in the IP.} \tag{3.6c}$$

This shows that within the benchmark model the quantity Σ^2 is not able to distinguish the SP and the

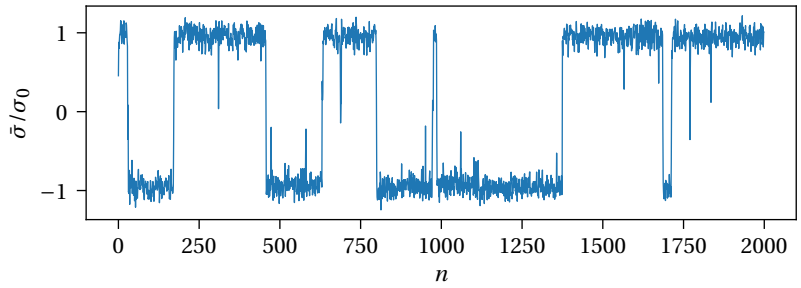

Figure 3.2: The averaged field $\bar{\sigma}$ plotted for every configuration of a Monte Carlo timeline in the HBP featuring the tunneling of the auxiliary field σ between the two minima of the action.

IP from one another. The information about an oscillation vanishes in the spacetime average, leaving only the part that originates from the noise. One might also consider $\langle\sigma(\boldsymbol{x})\rangle$ without the average. This would depend on a potential spatial drift in configurations (δx in ς). If such a drift would be present, the oscillations might also vanish in the ensemble average. Such a spatial drift of an oscillation would in principle not be forbidden and might occur in a Monte Carlo simulation in an analogous manner to the case in Figure 3.2 regardless of the actual spontaneous breaking of translation symmetry being present or not.

As an alternative, one could consider the FT of the field, where a spatial shift would only influence its phase. Therefore we define the next observable

$$\tilde{\Sigma}^2(k) = \frac{\left\langle \sum_{x_0\in\Gamma_0} |\tilde{\sigma}(x_0,k)|^2 \right\rangle}{N_0\sigma_0^2}, \tag{3.7}$$

where Γ_0 is the set of temporal lattice points given by $\Gamma_\mu = \{0, a, 2a, \ldots, (N_\mu - 1)a\}$ and $\tilde{\sigma}(x_0, p)$ is the spatial FT of $\sigma(\boldsymbol{x})$ as

$$\tilde{\sigma}(x_0,k) = \mathscr{F}_{x_1}[\sigma(\boldsymbol{x})](x_0,k). \tag{3.8}$$

This independence of the shift is also present in the model ς, where $\tilde{\Sigma}^2$ is able to distinguish all three phases as (the corresponding calculation is found in Appendix D.3)

$$\tilde{\Sigma}^2_{\varsigma_\mathrm{SP}} = \frac{\varepsilon^2}{\sigma_0^2} \qquad \text{in the SP,} \tag{3.9a}$$

$$\tilde{\Sigma}^2_{\varsigma_\mathrm{HBP}} = B^2 N_1 + \frac{\varepsilon^2}{\sigma_0^2} \qquad \text{in the HBP,} \tag{3.9b}$$

$$\tilde{\Sigma}^2_{\varsigma_\mathrm{IP}} = \frac{A^2 N_1}{4\sigma_0^2}\left(p_q\left(k - \frac{2\pi}{L_1}q\right) + \left(k + \frac{2\pi}{L_1}q\right)\right) + \frac{\varepsilon^2}{\sigma_0^2} \qquad \text{in the IP.} \tag{3.9c}$$

The Susceptibility of Σ^2

The susceptibility χ_{Σ^2} of Σ^2 is an indicator for phase transitions that Σ^2 is sensitive to. It diverges at such a phase boundary in an infinite volume (peaks in a finite volume) and is defined as

$$\chi_{\Sigma^2} = V\left(\left\langle (\Sigma^4\right\rangle - \left\langle \Sigma^2\right\rangle^2\right). \tag{3.10}$$

This observable is not suited to be tested by the benchmark model since it is only interesting in the vicinity of a phase boundary, where the model ς is (as already established) not valid. Since Σ^2 does not distinguish between the SP and the IP, we expect that it will be blind to a phase transition between the two. Nevertheless, it could be useful to map the phase boundary of the HBP.

3.2.2 Spatial Correlator

As an alternative to the chiral condensate we consider a spatial correlator, which might be able to detect inhomogeneities. We first define the quantity

$$c(x,y) = \frac{1}{N_0}\sum_{y_0\in\Gamma_0}\sigma(y_0,y)\sigma(y_0,y+x), \tag{3.11}$$

where y is a spatial reference point. When calculating the ensemble average of this observable using ς_IP as input (see Appendix D.4.1 for the detailed calculations with the full model ς) one finds that

$$\begin{aligned}\left\langle c_{\varsigma_\mathrm{IP}}(x,y)\right\rangle &= \int_{-\infty}^{\infty}\mathrm{d}\delta y\; p_y(\delta y)\;\left\langle c_{\varsigma_\mathrm{IP}}(x,y)\right\rangle_{\eta,\delta q}\\ &= \int_{-\infty}^{\infty}\mathrm{d}\delta y\; p_y(\delta y)\left[\cos\left(2\pi\left(2y+2\delta y+x\right)q/L_1\right)\vartheta\left((2y+2\delta y+x)/L_1,\mathrm{i}/2\pi\Delta q^2\right)\right.\\ &\qquad\left.+\cos\left(2\pi\, xq/L_1\right)\vartheta\left(x/L_1,\mathrm{i}/2\pi\Delta q^2\right)\right]\frac{A^2}{2\vartheta\left(0,\mathrm{i}/2\pi\Delta q^2\right)}+\varepsilon^2\delta_{x,0},\end{aligned} \tag{3.12}$$

where $\langle\cdot\rangle_{\eta,\delta q}$ indicates that only the ensemble averages of $\eta,\delta q$ are to be taken and we introduced the Jacobi theta function of the third kind

$$\vartheta(z,s) = \sum_{\tau=-\infty}^{\infty}\mathrm{e}^{\mathrm{i}\pi\tau^2 s+\mathrm{i}2\pi\tau z} = 1+2\sum_{\tau=1}^{\infty}\mathrm{e}^{\mathrm{i}\pi\tau^2 s}\cos(2\pi\tau z). \tag{3.13}$$

This expression still depends on the distribution of the shift, since we refrained from doing any assumption about the shift so far. In an exploratory manner we assume different distributions in order to see how this influences $\langle c_{\varsigma_\mathrm{IP}}(x,y)\rangle$. We consider the following cases:

I In a scenario where spontaneous breaking of translational symmetry is realized, we would assume that the oscillation is locked in position and therefore no shift occurs. A delta peak distribution mimics this case: $p_y^\mathrm{I}(\delta y) = \delta(\delta y)$.

II In the case that there is no spontaneous symmetry breaking or it is just invisible to the Monte Carlo algorithm, we would assume all shifts to be allowed. This corresponds to a uniformly distributed shift over the lattice: $p_y^\mathrm{II}(\delta y) = \Theta(\delta y)\,\Theta(L_1-\delta y)/L_1$.

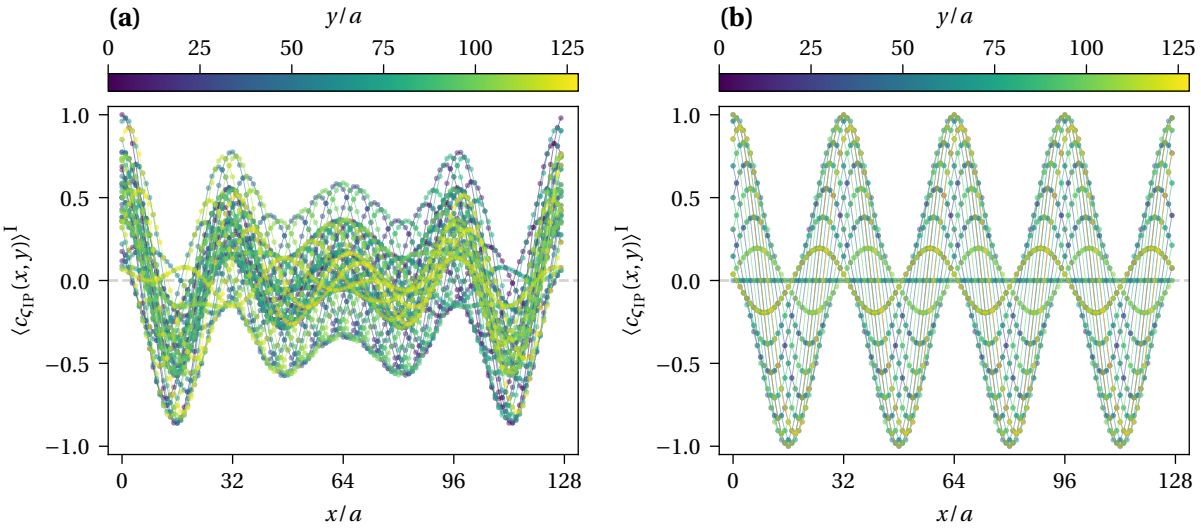

Figure 3.3: $\left\langle c_{\varsigma_\mathrm{IP}}(x,y)\right\rangle^{\mathrm{I}}$ for $A=1, L_1/a=128, q=4, \varepsilon=0$. **(a)** $\Delta q=0.7$. **(b)** $\Delta q=0.0$.

By inserting the distributions in Eq. (3.12) we obtain in case I

$$\left\langle c_{\varsigma_\mathrm{IP}}(x,y)\right\rangle^{\mathrm{I}} = \frac{A^2}{2\vartheta\left(0,\mathrm{i}/2\pi\Delta q^2\right)}\left[\cos\left(2\pi\left(2y+x\right)q/L_1\right)\vartheta\left((2y+x)/L_1,\mathrm{i}/2\pi\Delta q^2\right)\right.$$
$$\left.+\cos\left(2\pi\, xq/L_1\right)\vartheta\left(x/L_1,\mathrm{i}/2\pi\Delta q^2\right)\right]+\varepsilon^2\delta_{x,0} \quad (3.14)$$

and in case II

$$\begin{aligned}\left\langle c_{\varsigma_\mathrm{IP}}(x)\right\rangle^{\mathrm{II}} &= \frac{A^2}{2\vartheta\left(0,\mathrm{i}/2\pi\Delta q^2\right)}\left[\exp\left(-\frac{q^2}{2\Delta q^2}\right)+\cos\left(2\pi\, xq/L_1\right)\vartheta\left(x/L_1,\mathrm{i}/2\pi\Delta q^2\right)\right]+\varepsilon^2\delta_{x,0}\\ &\approx \frac{A^2}{2\vartheta\left(0,\mathrm{i}/2\pi\Delta q^2\right)}\cos\left(2\pi\, xq/L_1\right)\vartheta\left(x/L_1,\mathrm{i}/2\pi\Delta q^2\right)+\varepsilon^2\delta_{x,0}, \quad (3.15)\end{aligned}$$

where we used $q \gg \Delta q$ in the last step and the corresponding calculations are found in Appendix D.4.2.

Figure 3.3 shows $\langle c_{\varsigma_\mathrm{IP}}(x,y)\rangle^{\mathrm{I}}$ for a fictitious lattice of $N_1 = 128$ for a wide range of reference points y with frequency fluctuation width $\Delta q = 0.7$ (Figure 3.3a) and $\Delta q = 0.0$ (Figure 3.3b). Even though $\langle c_{\varsigma_\mathrm{IP}}(x,y)\rangle^{\mathrm{I}}$ depends strongly on the reference point y, for most y the curves follow a general oscillating shape. However, the curves for some y are systematic outliers, e.g. for $\Delta q = 0$ the curve for $y = L/4q$ is constant zero. This failure to detect an inhomogeneity would be an undesirable effect as we could miss an oscillation or severely underestimate its amplitude.

$\langle c_{\varsigma_\mathrm{IP}}(x,y)\rangle^{\mathrm{II}}$ on the other hand does not depend on y anymore as the uniform drift restores translational invariance in this observable, which is favorable, but is achieved in an uncontrolled way.

Although $\langle c(x,y)\rangle$ appears to be unsuited for an actual investigation of the IP, it might come in handy when we want to gain an insight into the distribution of a spatial shift in our simulations as its behavior is apparently sensitive to the shift distribution. In an effort to construct a more "robust" observable that is

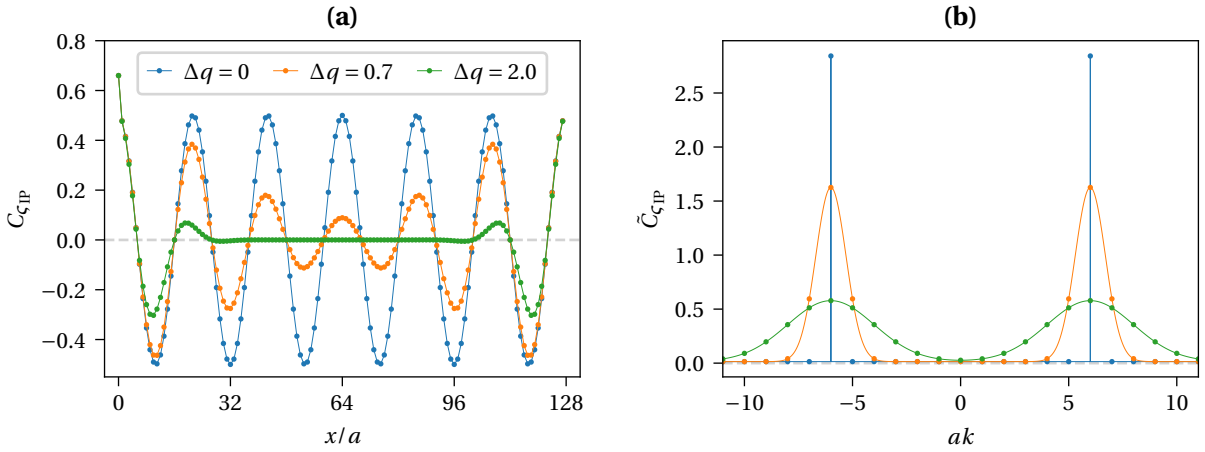

Figure 3.4: $C_{\varsigma_{IP}}$ and $\tilde{C}_{\varsigma_{IP}}$ for $A = 1$, $L_1/a = 128$, $q = 6$, $\varepsilon = 0.4$ for various Δq. **(a)** $C_{\varsigma_{IP}}$. **(b)** $\tilde{C}_{\varsigma_{IP}}$.

independent of the shift, we consider the full spacetime average over $\boldsymbol{y}$ of c

$$\bar{c}(x) := \frac{1}{|\Lambda|} \sum_{\boldsymbol{y} \in \Gamma} \sigma(\boldsymbol{y}) \sigma(y_0, y_1 + x). \tag{3.16}$$

The calculation of $\langle \bar{c}(x) \rangle_{\eta, \delta q}$ using ς_{IP} as input yields

$$\left\langle \bar{c}_{\varsigma_{IP}}(x) \right\rangle_{\eta, \delta q} = \frac{A^2}{2\vartheta\left(0, \mathrm{i}/2\pi\Delta q^2\right)} \cos\left(2\pi\, xq/L_1\right) \vartheta\left(x/L_1, \mathrm{i}/2\pi\Delta q^2\right) + \varepsilon^2 \delta_{x,0} \equiv \left\langle \bar{c}_{\varsigma_{IP}}(x) \right\rangle, \tag{3.17}$$

where the resulting expression is not dependent on the spatial shift δy anymore and thus is equal to the full expectation value $\langle \bar{c}(x) \rangle$. We define

$$C(x) := \langle \bar{c}(x) \rangle = \left\langle \frac{1}{|\Lambda|} \sum_{\boldsymbol{y} \in \Gamma} \sigma(\boldsymbol{y}) \sigma(y_0, y_1 + x) \right\rangle, \tag{3.18}$$

which we simply call the *spatial correlator* and is calculated within the model ς to be (the corresponding calculation is found in Appendix D.4.3)

$$C_{\varsigma_{SP}}(x) = \varepsilon^2 \delta_{x,0} \qquad \text{in the SP,} \tag{3.19a}$$

$$C_{\varsigma_{HBP}}(x) = B^2 \sigma_0^2 + \varepsilon^2 \delta_{x,0} \qquad \text{in the HBP,} \tag{3.19b}$$

$$C_{\varsigma_{IP}}(x) = \frac{A^2}{2\vartheta\left(0, \mathrm{i}/2\pi\Delta q^2\right)} \cos\left(2\pi\, xq/L_1\right) \vartheta\left(x/L_1, \mathrm{i}/2\pi\Delta q^2\right) + \varepsilon^2 \delta_{x,0} \qquad \text{in the IP.} \tag{3.19c}$$

Note that $C(x)$ is equal to $\langle c(x) \rangle^{\mathrm{II}}$, because the uniform distribution leads to the same mathematical operations as the spacetime average. The spatial correlator can distinguish all three phases and features an oscillation in the inhomogeneous phase with the same wave length as the original oscillation.

To analyze the oscillation within the correlator, we employ the FT of C

$$\tilde{C}(k) = \mathscr{F}_x[C(x)](k), \tag{3.20}$$

which takes the following form in the benchmark model:

$$\tilde{C}_{\varsigma_{\mathrm{SP}}}(k) = \frac{\varepsilon^2}{\sqrt{N_1}} \qquad \text{in the SP,} \tag{3.21a}$$

$$\tilde{C}_{\varsigma_{\mathrm{HBP}}}(k) = B^2\sqrt{N_1} + \frac{\varepsilon^2}{\sqrt{N_1}} \qquad \text{in the HBP,} \tag{3.21b}$$

$$\tilde{C}_{\varsigma_{\mathrm{IP}}}(k) = \frac{A^2\sqrt{N_1}}{4}\left(p_q\left(k - \frac{2\pi}{L_1}q\right) + \left(k + \frac{2\pi}{L_1}q\right)\right) + \frac{\varepsilon^2}{\sqrt{N_1}} \qquad \text{in the IP.} \tag{3.21c}$$

Figure 3.4 shows $C_{\varsigma_{\mathrm{IP}}}$ and $\tilde{C}_{\varsigma_{\mathrm{IP}}}$ for various Δq. The amplitude of the oscillation in $C_{\varsigma_{\mathrm{IP}}}$ is modulated by the Jacobi theta function, which results in a stronger fall-off for larger Δq. The emergence of the jacobi theta function in the fall-off is solely caused by our choice of the frequency fluctuation distribution and other choices might produces other fall-offs. Moreover, the correlator is symmetric around $L/2$. The frequency spectrum is symmetric around $k = 0$ and features peaks at $k = \pm q$ (q being the frequency of the oscillation in ς_{IP}) and the neighboring frequencies follow the Gaussian distribution of $p_q(k \pm q)$.

$\tilde{C}(k)$ is proportional to $\tilde{\Sigma}^2$ (only differing by a multiplicative factor) as the two quantities are related via the convolution theorem. We show the equality explicitly:

$$\begin{aligned}\tilde{C}(k) =& \frac{1}{\sqrt{N_1}}\sum_{x\in\Gamma_1}\frac{1}{|\Lambda|}\sum_{y\in\Gamma}\sigma(\boldsymbol{y})\sigma(y_0, y_1 + x)\mathrm{e}^{\mathrm{i}kx} = \frac{1}{|\Lambda|\sqrt{N_1}}\sum_{\boldsymbol{y}\in\Gamma}\sigma(\boldsymbol{y})\sum_{x\in\Gamma_1}\sigma(y_0, y_1 + x)\mathrm{e}^{\mathrm{i}kx} \\ =& \frac{1}{|\Lambda|^{3/2}}\sum_{\boldsymbol{y}\in\Gamma}\sigma(\boldsymbol{y})\sum_{x\in\Gamma_1}\sigma(y_0, x_1)\mathrm{e}^{\mathrm{i}k(x-y_1)} = \frac{1}{\sqrt{N_1}N_0}\sum_{y_0\in\Gamma_0}\tilde{\sigma}(y_0, k)\,\tilde{\sigma}(y_0, k)^* = \frac{\sigma_0^2}{\sqrt{N_1}}\tilde{\Sigma}^2,\end{aligned} \tag{3.22}$$

where we used the periodic boundary conditions for the bosonic field σ to shift the sum. This relationship enables us to gain insights into the present frequencies in σ by analyzing $\tilde{C}(k)$.

3.2.3 Minimum of the Spatial Correlator

The spatial correlator can distinguish the three phases within the model ς by its shape. It would, however, be favorable to encode the information about the phase in a scalar quantity. From Eq. (3.19), we can deduct that the minimum of the correlator in the three phases is

$$C_{\min} := \min_x C(x) = \begin{cases} > 0, & \text{inside the homogenously broken phase} \\ \approx 0, & \text{inside the symmetric phase} \\ < 0, & \text{inside the inhomogenous phase} \end{cases}. \tag{3.23}$$

This quantity should then be able to distinguish the phases and enables us to plot a phase diagram with it.

3.3 Simulation Parameters

In the following section we discuss the more numerical aspects and parameters of the performed simulations. Note that for the simulations and depicted results only the ND discretization was used unless explicitly stated otherwise.

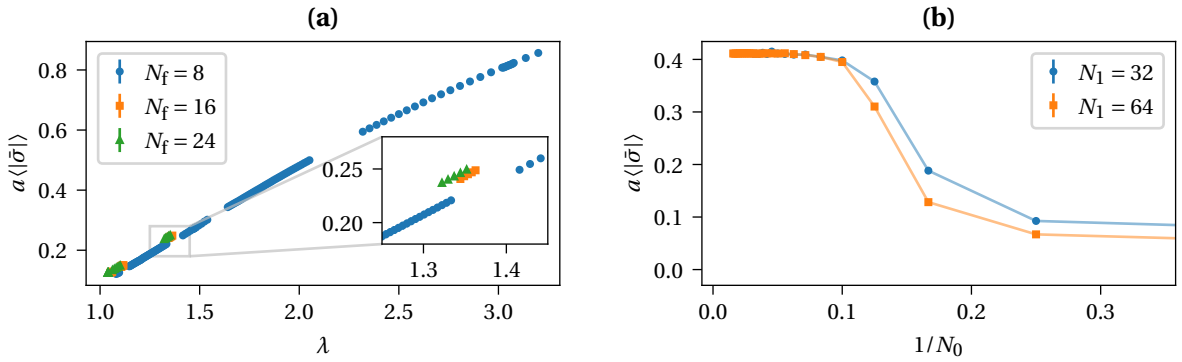

Figure 3.5: Simulation results needed for the determination of σ_0. **(a)** Scan over λ for $N_f = 8, 16, 24$, $N_0 = 64$, $N_1 = 64$. **(b)** Scan over $1/N_0$ for $N_f = 8$, $N_1 = 32, 64$, $\lambda = 1.8132$ to determine σ_0.

3.3.1 Determination of σ_0

In order to set the scale and the relative lattice spacing, we need to determine $a\sigma_0$. To do so, we first perform a scan over λ at $N_0 = 64$, $N_1 = 64$ and the corresponding N_f, and measure $a\langle|\bar{\sigma}|\rangle$. Figure 3.5a shows this scan for various N_f.

We choose a coupling λ that approximately corresponds to the wanted $a\sigma_0$. Subsequently, we perform a scan over N_0 for different N_1 for the selected λ, where $a\langle|\bar{\sigma}|\rangle$ quickly approaches a constant value $a\langle|\bar{\sigma}|\rangle \approx a\sigma_0$. This is depicted in Figure 3.5b for $\lambda = 1.8132$.

3.3.2 Thermalization and Starting Configuration

The number of steps it takes the system to thermalize depends on the parameters of the algorithm (foremost τ), the system size but also on the starting configuration. We use two different starting configurations for the auxiliary field σ:

1. *Hot* start: The auxiliary field σ is set to values drawn from a Gaussian distribution. This sort of configuration is similar to the configurations found in the SP and therefore, the system thermalizes quickly if this is the preferred phase.

2. *Cold* start: The auxiliary field σ is set to a constant non-zero value. This is very close to the configurations of the HBP and facilitates thermalization in such a phase.

Depending on the starting configuration and physical parameters the algorithm can be trapped in the "wrong" phase in a metastable minimum. As an example Figure 3.6 shows the Monte Carlo timelines of the action of two simulations for very low temperature at a chemical potential where the IP with several oscillations is preferred. One simulation is performed with a hot start, the other with a cold start where all other simulation parameters are exactly the same. The cold start needs over 1000 configurations to leave the homogeneous configurations and produce an oscillation, whereas the hot start needs about 350 configurations to be thermalized.[1] These thermalization times might be longer than the number of total configurations generated and thus one needs to be cautious. As a good practice one should perform simulations with both starts and only trust them when they agree. This procedure greatly increases the numerical effort and therefore we only follow it in problematic regions exemplary to gain more insight into magnitude of the effect or when we are interested in the exact position of a phase transition.

[1] Note that the exact thermalization time is difficult to determine for the hot start. There is no scalar quantity that is able to

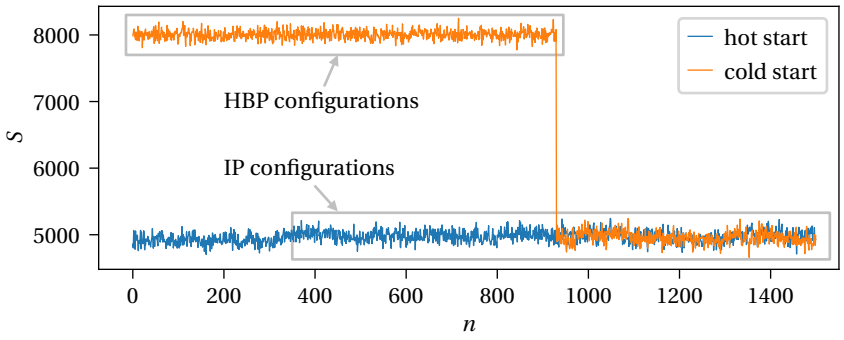

Figure 3.6: The Monte Carlo timelines of the action from simulations that have all parameters in common except for the starting configuration.

3.3.3 Simulated Ensembles

In order to obtain the results presented in the following, a large number of field configuration ensembles had been generated for a wide range of N_f, N_1, N_0, μ, a with 500–4000 configurations per ensemble. Table 3.2 is a compilation of these generated ensembles.

3.4 Results on the Gross-Neveu Model in 1 + 1 Dimensions at $N_f = 8$

This section is structured according to the available observables and discuss them one by one. All results are obtained with $N_f = 8$ and the ND discretization unless stated otherwise.

3.4.1 Results Obtained with Σ^2

Phase Transition at $\mu = 0$

We investigate the phase transition at $\mu = 0$ for varied temperature as a first test of volume and lattice spacing dependence. Figure 3.7 shows simulation results of Σ^2 for $a \approx 0.4113/\sigma_0$ and various L_1. The critical temperature T_c of the phase transition is indicated by the peak of the susceptibility in Figure 3.7b. The flat peaks of the blue and orange curves are likely caused by the fact that T_c is between the available temperatures. Overall the critical temperature does not depend strongly on the volume in the regime of the simulated volumes. We conclude that a physical size of $L_1 \geq 13.16\sigma_0$ seems to be sufficiently large for a qualitative investigation.

An infinite volume is required when one performs the continuum limit, where L_1 is kept constant and the limit $a \to 0$ is taken. This limit is shown in Figure 3.8 where the phase transition is shown for various a and $L_1 = 13.16/\sigma_0$. The shape of the chiral condensate Σ^2 and the critical temperature is quite similar for the two smaller lattice spacings. The difference of the largest lattice spacing shows how much the naive fermions are plagued by discretization effects.

Due to the limited temperature resolution (as discussed in Section 2.3.2) a reliable determination of T_c in the continuum is not possible without considerably smaller lattice spacings or the application of multiple-histogram methods. This would, however, go far beyond the scope of this thesis as its goal is not the exact determination of T_c.

differentiate between the IP and the SP on a single configuration. Therefore the given number was determined in this case by reviewing the spatial correlators on the single configurations.

$N_1 = L_1/a$	$N_0 = 1/Ta$	μ/σ_0	λ	$a\sigma_0$
$N_f = 8$				
16	$2,4,\ldots,16$	$0.0,\ldots,1.0$	1.8132	0.4113(3)
32	$2,4,\ldots,32$	$0.0,\ldots,1.0$	1.8132	0.4113(3)
			2.0619	0.5036(9)
			3.0710	0.8206(6)
64	$2,4,\ldots,44,48,52,\ldots,64$	$0.0,\ldots,1.4$	1.8132	0.4113(3)
		$0.0,\ldots,1.1$	1.4172	0.2518(5)
128	$12,14,\ldots,52,56,\ldots,70,76,80,100$	$0, 0.59$	1.0960	0.1253(3)
	$80,100$	$0.5,\ldots,0.9$		
$N_f = 16$				
64	$2,4,\ldots,28,32,\ldots,48$	0.0	1.3687	0.2518(5)
	48	$0.0,\ldots,1.0$		
$N_f = 24$				
64	$2,4,\ldots,28,32,\ldots,48$	0.0	1.3567	0.2518(5)
	48	$0.0,\ldots,1.0$		

Table 3.2: Ensembles of field configurations.

Σ^2 in the (μ, T)-Plane

Of more interest is the region of $\mu > 0$, which we will investigate thoroughly with $C_{\min}$ as it is able to differentiate all phases. Nevertheless we consider also Σ^2 in the (μ, T)-plane for completeness. All data in the (μ, T)-plane is shown as heatmaps where the color corresponds to the measured value of the corresponding observable mapped by the colorbar. The data is linearly interpolated in these heatmaps as it drastically facilitates the interpretation of the data and the position of the actual data is indicated by grey dots. The corresponding plots with the uninterpolated data are to be found in Appendix E.

Figure 3.9 depicts Σ^2 for $L \approx 16.12/\sigma_0$ and $a \approx 0.2518/\sigma_0$ with the phase boundary of the HBP from the large-N_f results in white. The SP corresponds to the black region, the HBP to the yellow region. The HBP is of similar shape as in the large-N_f case, albeit smaller in size with the difference in the temperature direction being larger. The blue dots corresponds to $\max_\mu \chi_{\Sigma^2}\big|_T$, i.e. the susceptibility χ_{Σ^2} maximized over the chemical potential μ for fixed temperature T[2] and the determined maxima align with the perceived phase transition. The data around the phase transition for the lowest simulated temperatures shows an unexpected behavior, which is likely caused by irreconcilable thermalization effects. Therefore, in this case, the data points in the vicinity of the phase transition at temperatures below $T/\sigma_0 \approx 0.1$ are, in general, unreliable.

[2] The upper temperature limit for this procedure was set to T_c at $\mu = 0$—determined by a peak in a scan of the susceptibility at $\mu = 0$.

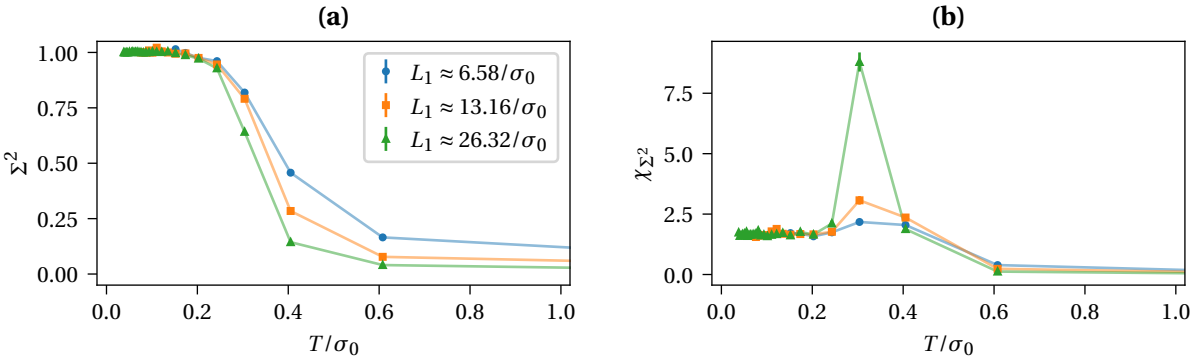

Figure 3.7: Temperature scan at $\mu = 0$ for various L_1 and $a \approx 0.4113/\sigma_0$. **(a)** Σ^2. **(b)** χ^2_Σ.

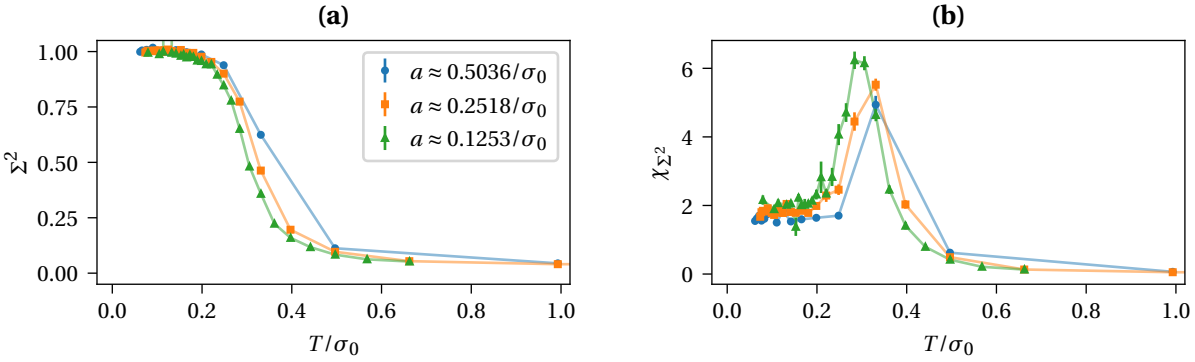

Figure 3.8: Temperature scan at $\mu = 0$ for various a and $L_1 \approx 16/\sigma_0$. **(a)** Σ^2. **(b)** χ^2_Σ.

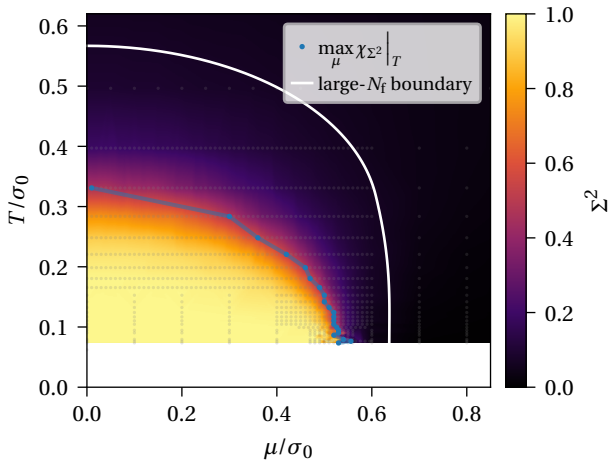

Figure 3.9: Σ^2 in the (μ, T)-plane for $L \approx 16.12/\sigma_0$ and $a \approx 0.2518/\sigma_0$. The data is linearly interpolated with the (μ, T) values of the actual simulated data given by the grey dots. The blue dots correspond to $\max_\mu \chi_{\Sigma^2}\big|_T$. The white lines represent the large-N_f boundary of the homogeneously broken phase [3, 4].

3.4.2 The Spatial Correlator

The spatial correlator is able to clearly distinguish the different phases within the benchmark model and thus appears also able to achieve this in the simulations. Figure 3.10 shows C (left column) and $\tilde{C}$ (right column), where each row corresponds to different (μ, T). The x-axis in the C plots extends up to $L_1/2$ as the correlator is symmetric and likewise the plot of $\tilde{C}$ depicts only data for positive k.

The first row with $(\mu/\sigma_0, T/\sigma_0) \approx (0, 0.665)$ (Figures 3.10a and 3.10b) corresponds to the SP and the second row (Figures 3.10c and 3.10d) with $(\mu/\sigma_0, T/\sigma_0) \approx (0, 0.080)$ to the HBP. The spatial correlator in the SP and HBP does not show behavior that is qualitatively different from the one shown by Σ^2. It is in fair agreement with the benchmark model only differing in the fall-off of the $x = 0$ peak. The noise η in the model ς is not spatially correlated and thus produces only a δ peak at $x = 0$. This is of course unlikely to be realistic and thus causes a difference to the simulations.

The third and fourth row (Figures 3.10e to 3.10h) with $(\mu/\sigma_0, T/\sigma_0) \approx (0.7, 0.08)$,$(\mu/\sigma_0, T/\sigma_0) \approx (0.9, 0.1)$ correspond to the IP with combined fits of the benchmark correlator $C_{\varsigma_{\mathrm{IP}}}$ and its FT $\tilde{C}_{\varsigma_{\mathrm{IP}}}$ to the data of the smallest lattice spacing in a limited fit range as grey curves. The spatial correlator obtained from the simulations shows a clear oscillation, which is in fair agreement to the behavior of $C_{\varsigma_{\mathrm{IP}}}$—given its simplicity. Recalling the connection of $\tilde{C}(k)$ and $|\tilde{\sigma}(y_0, k)|$ from Eq. (3.22), we can conclude that there is also a pronounced oscillation with a dominating frequency present in σ itself. Furthermore, it also displays an increase in frequency and decrease in amplitude of the oscillation for increasing μ similar to the large-N_f results.

For larger lattice spacing the oscillations of C in the IP have a considerably smaller amplitude or vanish altogether. The reason why this is happening becomes clear when we recall that the ND discretization suppresses the large momenta of σ in order to decouple the sub-flavors from one another. This, however, decouples the large momenta of σ altogether. For large lattice spacings, the Brillouin zone can be small enough for the relevant frequency of the oscillation to be affected by the suppression. This is prominent in Figure 3.10f, where the true peak of the largest lattice spacing is suppressed in such a magnitude that the peak is located at a neighboring frequency and in a similar manner in Figure 3.10h that features a cusp, which is the remnant of a completely suppressed peak. The suppression procedure also causes the decoupled large momenta of $\tilde{C}$ to be constant. The onset of this effect moves to smaller k for larger lattice spacings. This happens for the green curve at $k \approx 3$ and for the orange curve at $k \approx 6$ in Figures 3.10f and 3.10h.

Probing of the Spatial Drift with $\langle c(x, y) \rangle$

The benchmark model calculations indicated that $\langle c(x, y) \rangle$ shows different behavior depending on the distribution of a spatial shift. The absence of a spatial drift (case I) would result in a strong dependence of $\langle c(x, y) \rangle$ on y, where $\langle c(x, y') \rangle \approx 0$ for certain y'. A uniform distribution of a spatial shift in the configurations (case II) would result in an independence of $\langle c(x, y) \rangle$ from y and the same behavior as C. Figure 3.11 shows a scan over all possible y of $\langle c(x, y)) \rangle$ for $(\mu/\sigma_0, T/\sigma_0) \approx (0.9, 0.08)$. The curves all follow the same shape with no curves apparently being systematic outliers with, e.g. an amplitude of approximately zero. In conjunction with the observed behavior of $\langle c_{\varsigma_{\mathrm{IP}}}(x, y) \rangle^{\mathrm{I}}$ and $\langle c_{\varsigma_{\mathrm{IP}}}(x, y) \rangle^{\mathrm{II}}$ this indicates that there is indeed a somewhat uniform spatial drift and thus also translation symmetry in the simulations. This is the expected behavior of the ergodic rHMC algorithm and was also observed in exemplary inspections of the other lattice ensembles.

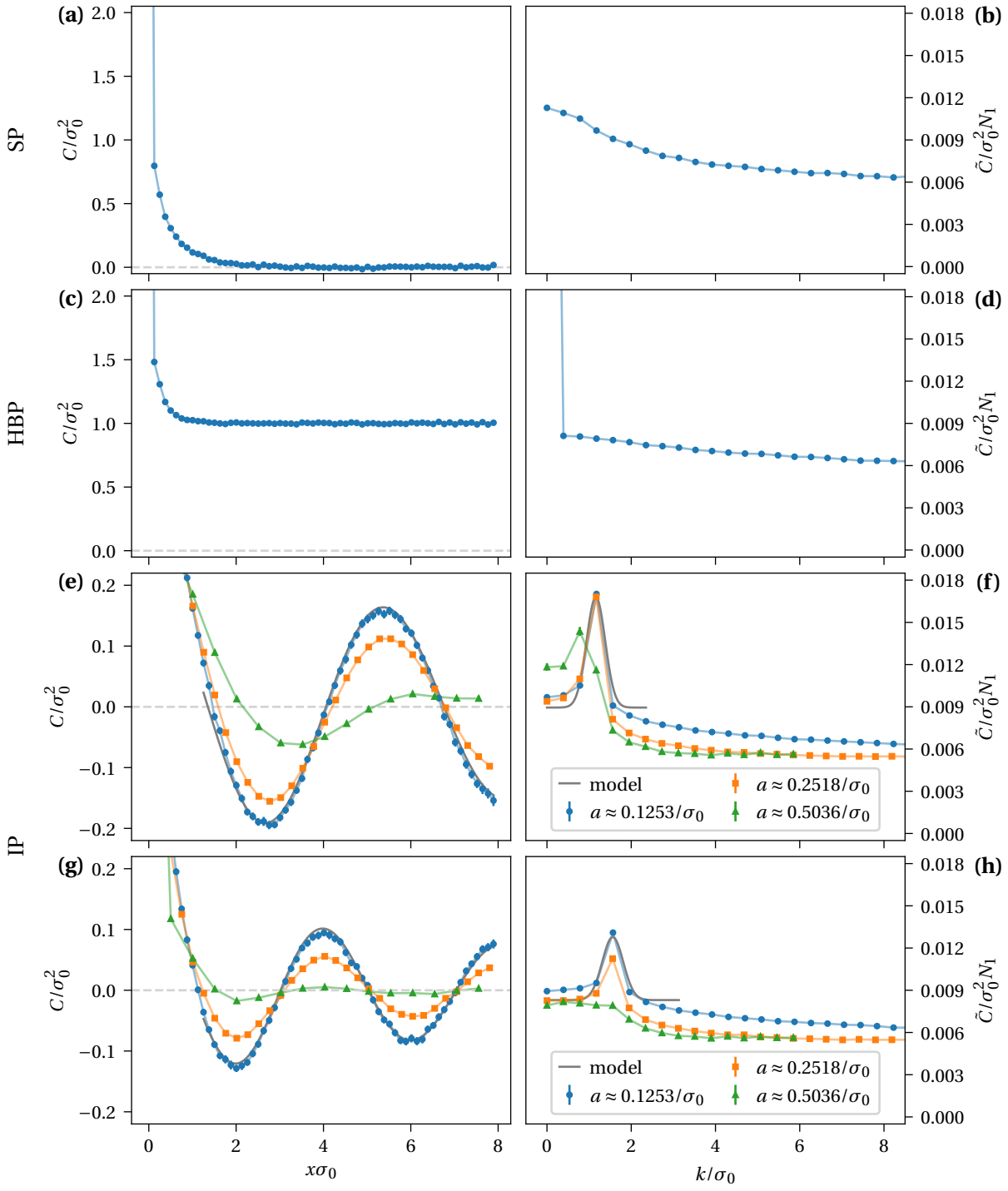

Figure 3.10: Simulation results of the spatial correlator C (left column) and its FT $\tilde{C}$ (right column) for various (μ, T), T, a and $L_1 = 16/\sigma_0$.
(a),(b) $(\mu/\sigma_0, T/\sigma_0) \approx (0, 0.665)$ corresponding to the SP with $a \approx 0.1253/\sigma_0$.
(c),(d) $(\mu/\sigma_0, T/\sigma_0) \approx (0, 0.080)$ corresponding to the HBP with $a \approx 0.1253/\sigma_0$.
(e),(f) $(\mu/\sigma_0, T/\sigma_0) \approx (0.7, 0.08)$ and **(g),(h)** $(\mu/\sigma_0, T/\sigma_0) \approx (0.9, 0.08)$ corresponding to the IP. The grey lines are combined fits of $C_{\varsigma_{\mathrm{IP}}}$ and $\tilde{C}_{\varsigma_{\mathrm{IP}}}$ to the simulation data of the smallest lattice spacing in a limited fitting window.

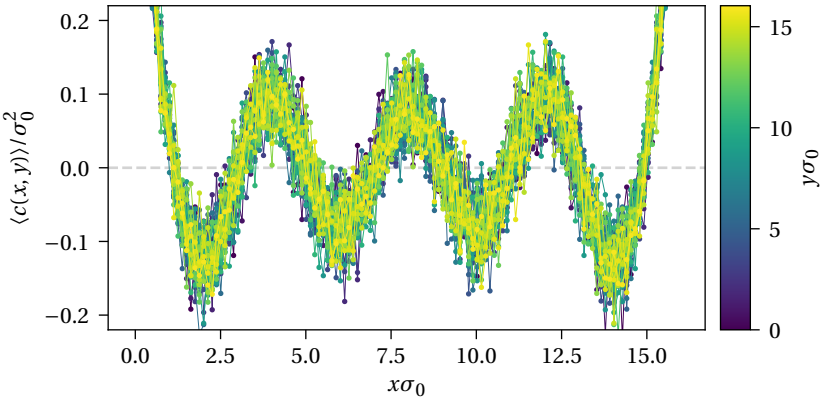

Figure 3.11: $\langle c(x,y)\rangle$ at $(\mu/\sigma_0, T/\sigma_0) \approx (0.9, 0.08)$ for $a \approx 0.1253/\sigma_0$, $L_1 = 16.04/\sigma_0$.

3.4.3 The Phase Diagram Obtained with C_{min}

Now that it is established that the spatial correlator C indeed indicates inhomogeneous behavior of the auxiliary field σ, we can use its spatial minimum C_{min} as a scalar indicator as to whether there is an IP for a given (μ, T). From Figure 3.10a we expect C_{min} in the SP to have mostly small negative values due to noise—contrary to the expectation from the benchmark model.

Figures 3.12a to 3.12c depict C_{min} in the (μ, T)-plane for decreasing a (and similar L_1) with the large-N_f phase boundaries in white as comparison. According to our expectation of C_{min}, the yellow region indicates an HBP, the black region an SP and the blue region an IP. The structure of the phase diagram shows strong similarities to the large-N_f results, albeit the IP and the HBP are smaller. This is likely due to the quantum fluctuations that are present at finite N_f and increase disorder—favoring an SP.

As we have seen in Figure 3.10, the lattice spacing has a significant impact on the IP, which is also prominent in the C_{min} plot. For the largest lattice spacing the IP barely exists and increases in size for decreasing lattice spacing just as in the large-N_f limit (compare to Figure 2.7b). This is further illustrated by Figures 3.12d to 3.12f where the differences of the C_{min} data for the various lattice spacings are shown.[3] These plots also uncover that the HBP/IP phase boundary moves considerably for low temperatures for varied lattice spacing. The differences for high temperatures are likely a combination of the limited temperature resolution and the interpolation procedure as they are of limited magnitude.

We know from the large-N_f results that the chiral condensate right after the HBP to IP transition contains a single oscillation with an "infinite" wavelength. This leads to the expectation that the location of this phase boundary is governed by finite size effects, since there is a maximum wavelength that is able to fit inside the box. Therefore, the realization of the first oscillation might be delayed to a larger μ corresponding to the first wavelength that fits inside the box. In order to verify this expectation, we compare C_{min} of different volumes L_1 at fixed lattice spacing a in Figures 3.12g to 3.12i and the difference plots in Figures 3.12j to 3.12l. It appears as though the influence of finite size on the HBP/IP transition at low temperatures is negligible as the difference region becomes quite small. The reason for the large difference regions at high temperature can be illustrated by Figure 3.7a, where the value of Σ^2 in the SP is larger for smaller volumes, where the noise is less suppressed in the average. This effect is present in a similar manner in C_{min}, albeit not shown explicitly.

Figure 3.12b also shows a "backbending" of the HBP/IP phase boundary for low temperatures, which is

[3] Note that whenever one of the compared ensembles lacked data, their difference is set to zero (black) for visualization purposes.

not a thermalization issue (as both hot and cold start exhibit this behavior). This effect is also present in large-N_f lattice calculations and is a combined effect of finite volume and finite lattice spacing, which was found to vanish non-monotonically in the respective limits (compare with Ref. [42]).

As the HBP/IP phase transition is of particular interest and apparently sensitive to the lattice spacing, we consider C_{min} at fixed temperature T for varied chemical potential μ for different a in Figure 3.13a. The location of the phase transition seems to converge nicely. The continuous decrease of C_{min} during the phase transition resembles a second order phase transition. This can be further illustrated by Figure 3.13b which shows the action S and $\bar{\sigma}$ per configuration of the circled data point in Figure 3.13a. Although $\langle\bar{\sigma}\rangle$ is not able to differentiate the three phases, $\bar{\sigma}$ allows us to categorize configurations to certain phases (with the categorization being backed up by exemplary review of spatial correlators on the configurations). By this categorization we are able to observe the algorithm freely tunneling between the phases. The action stays seemingly constant for the brief tunneling and the different phases.

Figure 3.14 shows scans of C_{min} for fixed $\mu = 0$ and $\mu/\sigma_0 \approx 0.59$. The scan at $\mu = 0$ is of similar shape as the Σ^2 scans depicted in Figures 3.7 and 3.8. This is not surprising as the two observables are expected to behave similarly for homogeneous phases as indicated by the behavior of C_ς and Σ_ς^2 . The slice at finite chemical potential reveals how the amplitude of the oscillation increases for decreasing temperature, but does not show any plateau behavior as for the $\mu = 0$ case. This, however, is likely attributed to the fact that the temperatures are not sufficiently low as the results in Ref. [16] feature a plateau for even lower temperatures. Moreover, the transition seems to be smooth and resembles a second order transition, higher order transition or even a crossover.

3.4.4 Comparison of the Naive Naive and Naive Distributed Discretization

Now that we thoroughly discussed the phase diagram obtained by simulations with the ND discretization, we want to illustrate the difference to the phase diagram obtained with the NN discretization. Figures 3.15a and 3.15c show the phase diagrams obtained with the NN and ND discretization for $a \approx 0.41/\sigma_0$, $L_1 \approx 26.24$ and Figure 3.15b shows a difference plot of the two. The phase diagrams seem to be quite similar in structure as both posses all three phases. Compared to the ND discretization, the NN discretization features a considerably smaller HBP both in T and μ direction. The IP on the other hand is larger, which is explained by the fact that high frequencies of oscillations σ are not suppressed and are only limited by the resolution of the lattice spacing.

In contrast to the continuum limit in the large-N_f case depicted in Figure 2.7b, the agreement of the two discretizations does not increase for decreasing lattice spacing in our finite N_f simulations. The correctness of the ND discretization is backed up by the agreement to the SLAC discretization as presented in Ref. [16].

3.5 Dependence on N_f

As shown before, the phase diagram at $N_f = 8$ is qualitatively similar to the large-N_f phase diagram and we want to check whether the phase diagram becomes increasingly similar to the large-N_f case for increasing N_f. We check this with simulations on $a \approx 0.25/\sigma_0$, $L_1 \approx 16/\sigma_0$ lattices for $N_f = 8, 16, 24$. A temperature scan at $\mu = 0$ (see Figure 3.16a) nicely shows how the shape of Σ^2 at the phase transition approaches the large-N_f result for increasing N_f. Moreover, the value of Σ^2 in the SP decreases with increasing N_f as quantum fluctuations are increasingly suppressed. Figure 3.16b features a scan over μ at $T/\sigma_0 \approx 0.08$. The transition moves slightly towards the critical chemical potential from the large-N_f results at this temperature. The

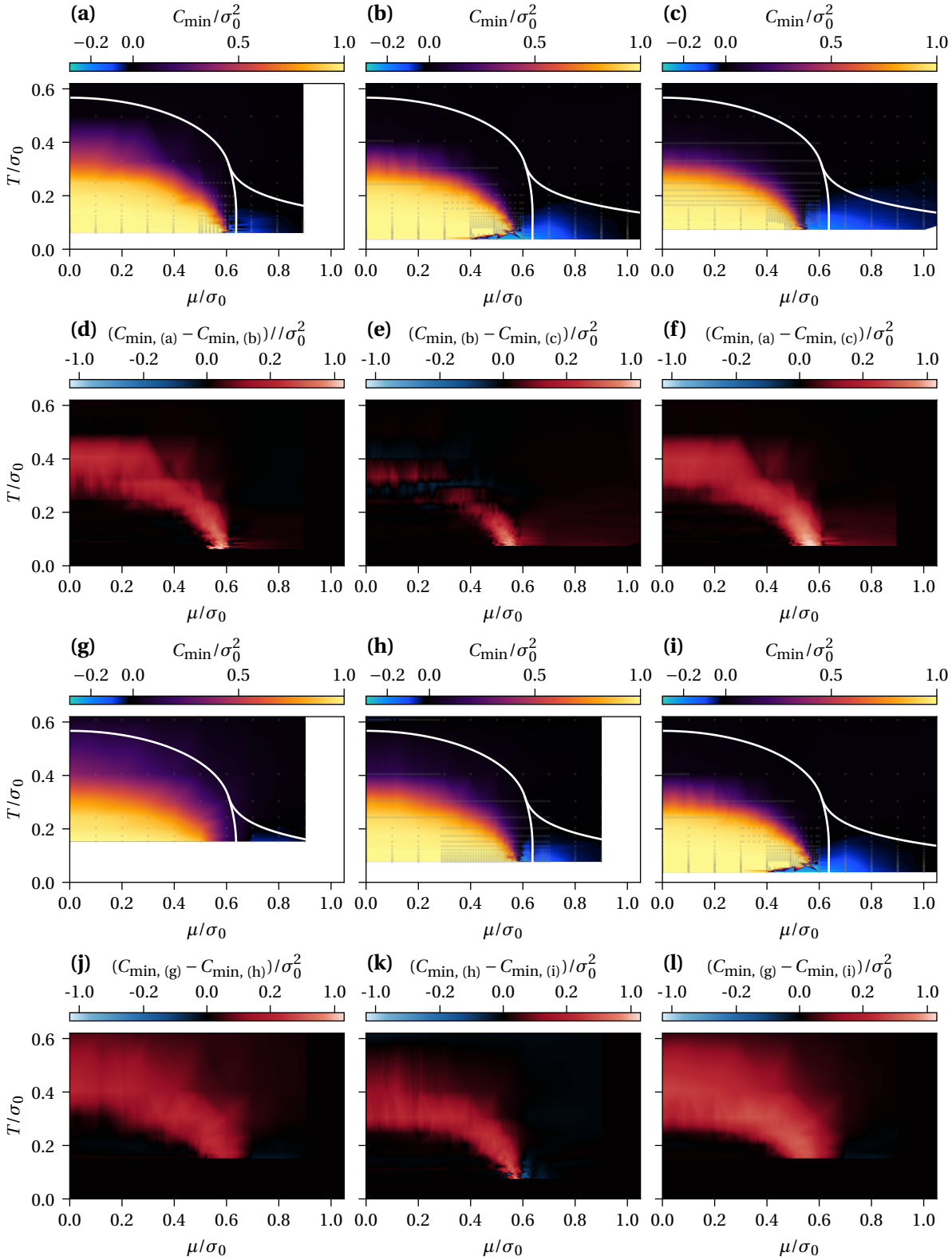

Figure 3.12: Simulation results for various lattice ensemble in the (μ, T)-plane with C_{min} in (a)-(c), (g)-(i) and the difference of these data sets in (d)-(f), (j)-(l). The data is linearly interpolated with the (μ, T) values of the actual simulated data given by the grey dots. The white lines represent the large-N_f phase boundaries [3, 4]. **(a)** $a \approx 0.5036/\sigma_0$, $L_1 = 16.12/\sigma_0$. **(b)** $a \approx 0.4113/\sigma_0$, $L_1 = 26.32/\sigma_0$. **(c)** $a \approx 0.2518/\sigma_0$, $L_1 = 16.12/\sigma_0$. **(g)** $a \approx 0.4413/\sigma_0$, $L_1 = 6.58/\sigma_0$. **(h)** $a \approx 0.4413/\sigma_0$, $L_1 = 13.16/\sigma_0$. **(i)** $a \approx 0.4413/\sigma_0$, $L_1 = 26.32/\sigma_0$.

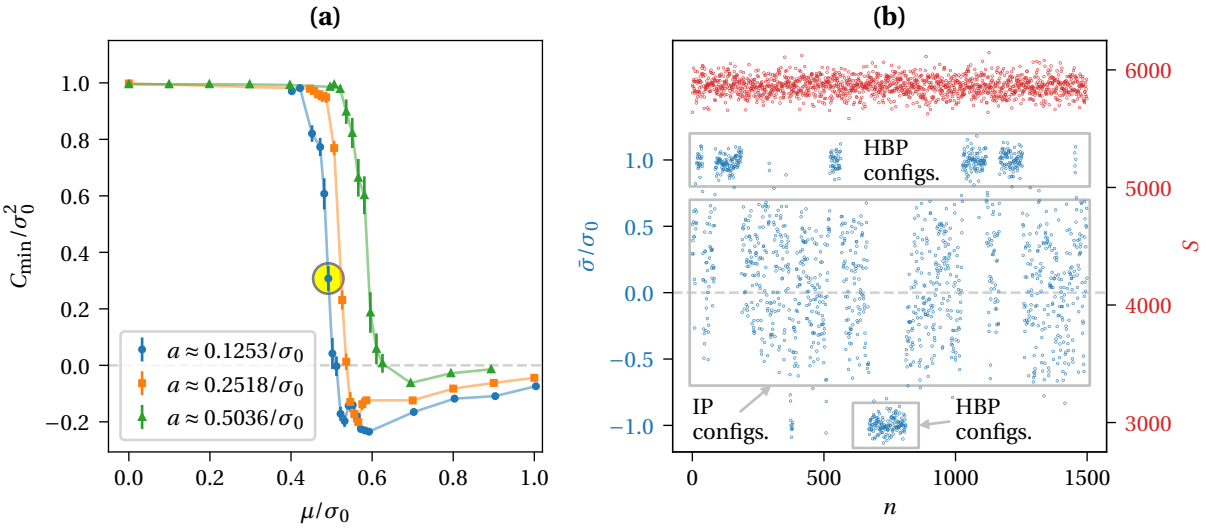

Figure 3.13: Simulation results for $T/\sigma_0 \approx 0.1$ and $L_1 = 16.04/\sigma_0$. **(a)** C_{min} for varied chemical potential μ and for various a. **(b)** The action S and $\bar{\sigma}$ per configuration n for $\mu/\sigma_0 \approx 0.49$ and $a \approx 0.1253/\sigma_0$ (The circled point in (a)).

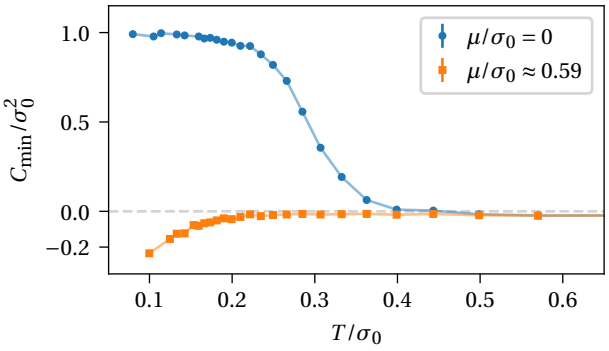

Figure 3.14: C_{min} at $\mu = 0$, $\mu \approx 0.59/\sigma_0$ for varied temperature T and for $a \approx 0.1258\sigma_0$, $L_1 = 16.04/\sigma_0$.

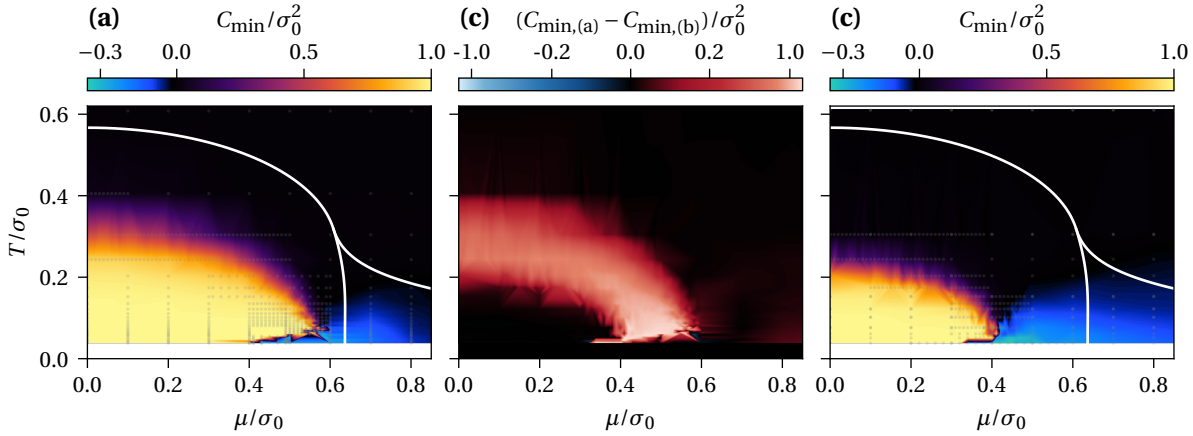

Figure 3.15: C_{min} in the (μ, T)-plane for $a \approx 0.41/\sigma_0$, $L_1 \approx 26.24/\sigma_0$ for the ND and NN discretization. The white lines represent the large-N_f phase boundaries [3, 4]. **(a)** ND discretization. **(b)** Difference of the data from (a) and (c). **(c)** NN discretization.

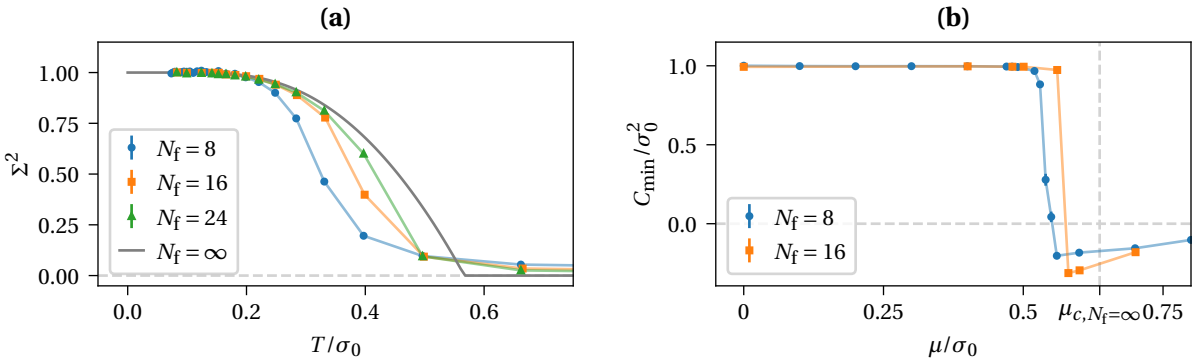

Figure 3.16: Simulation results for different flavors $N_f = 8, 16, 24$ on $a \approx 0.25/\sigma_0$, $L_1 \approx 16/\sigma_0$ lattices. **(a)** Σ^2 at $\mu = 0$ for varied temperature with the large-N_f result in grey. **(b)** C_{min} at $T/\sigma_0 \approx 0.08$ for varied chemical potential. The critical chemical potential in the large-N_f limit at this temperature is shown as the vertical dashed line.

simulations were done both for a hot and cold start, thus ruling out that the discrepancy is caused by thermalization effects. It would be interesting to compare to an even higher N_f. However, the thermalization times in this (μ, T)-region are quite long and increase with N_f. Therefore, the simulations of higher N_f proved to be too costly.

4 Conclusions and Outlook

The main focus of this work was the investigation of the possible existence and characterization of the IP in the $1+1$-dimensional GN model at finite N_f. The main tool for this investigation was the spatial correlator C, which shows a distinctly different behavior for three regions in the (μ, T)-plane. In a region at low temperatures and high chemical potential it showed a strong oscillation and its FT features a single dominating frequency. By its relationship to the auxiliary field σ, one can conclude that the field itself has to contain a dominant oscillation. However, by the nature of the employed numerical techniques it is not possible to draw any conclusion about the presence of spontaneous symmetry breaking. This question remains unanswered even after a thorough investigation of the correlator's long-range behavior in Ref. [16], where it could, however, be argued by the distinctly different behavior of the correlator in the symmetric and inhomogeneous region that a phase transition has to happen.

All three found phases persist for decreasing lattice spacing and the obtained phase diagram at finite N_f has a similar structure as the large-N_f phase diagram. The phase boundaries seem to converge to the large-N_f results for increasing N_f, which is a reassuring observation since this means that the often employed large-N_f limit is, in principle, able to retain information on the finite N_f case.

This renders finite N_f investigation of other models featuring IPs in the large-N_f limit a promising endeavor. Only very recently the rich phase diagram of the isoNJL model in $1+1$ dimensions for multiple chemical potentials was studied in the large-N_f case [9, 10]. Motivated by the findings in this work, this appears to be a promising candidate for further finite N_f investigations in $1+1$ dimensions. A variation of the GN, that comes to mind, would be the extension to $2+1$ dimensions, where an early work found an inhomogeneous chiral condensate, that is energetically degenerate to the translation invariant solution [54] and a preferred IP was found in an exploratory lattice study [45]. The latter result, however, proved to be a lattice artifact that vanishes in the continuum limit [55, 46] and thus discourages a finite N_f study. The $3+1$-dimensional NJL model features an IP, but it is not renormalizable and therefore depends on a cutoff scale (compare, e.g. Ref. [5]), which raises questions about the predictive capabilities for QCD. The Quark-meson model on the other hand is renormalizable and shares some characteristics of the NJL (including an IP). As it is mostly studied in the mean field approach or other approximations, a full lattice simulation could be interesting.

The phenomenon of color superconductivity (particle-particle pairing $\psi\psi$ instead of antiparticle-particle pairing $\bar{\psi}\psi$ in the chiral condensate) occurs in some models, e.g. the NJL model and also in the ground state of QCD at asymptotically high densities. In the NJL model one finds, with a specific inhomogeneous ansatz for the chiral condensate and the assumption of constant diquark condensate $\psi\psi$, that a color superconducting phase overlaps with the IP resulting in a region where both phases compete [56, 57]. Even more interestingly, an inhomogeneous color superconducting phase could occur in isospin asymmetric systems, e.g. neutron stars (compare to Ref. [5] and references therein). As these color superconducting phases seem to occur in the same (μ, T)-regions (and might even be inhomogeneous themselves) as inhomogeneous chiral condensates, an investigation of the latter should eventually include color superconductivity.

A Properties of the Dirac Operator

A.1 Properties of $\det Q_{\mathrm{GN}}$ and Proof that $\det Q_{\mathrm{GN}} \in \mathbb{R}$

We consider the GN Dirac operator Q [1] from Eq. (1.12)

$$Q(\boldsymbol{x},\boldsymbol{y})[\sigma,\mu] = \delta(\boldsymbol{x}-\boldsymbol{y})\left(\partial_{\boldsymbol{y}} + \gamma_0\mu + \sigma(\boldsymbol{x})\right), \tag{A.1}$$

where we explicitly write the dependence on σ,μ in order to keep track of their signs. The momentum representation of Q is then

$$Q(\boldsymbol{q},\boldsymbol{p})[\sigma,\mu] = 2\pi\,\delta(\boldsymbol{q}-\boldsymbol{p})(\mathrm{i}\gamma_\mu \boldsymbol{p}_\mu + \gamma_0\mu) + \underbrace{\int \mathrm{d}^2\boldsymbol{x}\,\mathrm{e}^{-\mathrm{i}\boldsymbol{x}(\boldsymbol{q}-\boldsymbol{p})}\sigma(\boldsymbol{x})}_{2\pi\,\tilde{\sigma}(\boldsymbol{q}-\boldsymbol{p})}, \tag{A.2}$$

with the eigenvalue equation

$$\int \frac{\mathrm{d}^2\boldsymbol{p}}{2\pi}\, Q(\boldsymbol{q},\boldsymbol{p})[\sigma,\mu]\,\chi_j(\boldsymbol{p}) = \lambda_j(\boldsymbol{q})\,\chi_j(\boldsymbol{q}), \tag{A.3}$$

where $j \in \{1,2\}$ and the determinant

$$\det Q[\sigma,\mu] = \prod_{q}\prod_{j=1}^{2}\lambda_j(\boldsymbol{q}). \tag{A.4}$$

By applying γ_{ch} from left and inserting $\gamma_{\mathrm{ch}}\gamma_{\mathrm{ch}} = \mathbb{1}$ left of $\chi_j(\boldsymbol{p})$ in Eq. (A.3) we obtain

$$\int \mathrm{d}^2\boldsymbol{p}\left[\delta(\boldsymbol{q}-\boldsymbol{p})(\mathrm{i}\underbrace{\gamma_{\mathrm{ch}}\gamma_\mu\gamma_{\mathrm{ch}}}_{=-\gamma_\mu}\boldsymbol{p}_\mu + \underbrace{\gamma_{\mathrm{ch}}\gamma_0\gamma_{\mathrm{ch}}}_{=-\gamma_0}\mu) + \tilde{\sigma}(\boldsymbol{q}-\boldsymbol{p})\right]\gamma_{\mathrm{ch}}\,\chi_j(\boldsymbol{p}) = \lambda_j(\boldsymbol{q})\,\gamma_{\mathrm{ch}}\,\chi_j(\boldsymbol{q}), \tag{A.5}$$

which shows that the determinant is an function of σ, i.e.

$$\det Q[\sigma,\mu] = \det Q[-\sigma,\mu]. \tag{A.6}$$

Taking the complex conjugate of Eq. (A.3) yields

$$\int \mathrm{d}^2\boldsymbol{p}\left[\delta(\boldsymbol{q}-\boldsymbol{p})(-\mathrm{i}\gamma_\mu^*\boldsymbol{p}_\mu + \gamma_0^*\mu) + \tilde{\sigma}^*(\boldsymbol{q}-\boldsymbol{p})\right]\chi_j^*(\boldsymbol{p}) = \lambda_j^*(\boldsymbol{q})\,\chi_j^*(\boldsymbol{q}), \tag{A.7}$$

where a subsequent application of $\mathscr{C}_+^*$ from the left and insertion of $\left(\mathscr{C}_+^*\right)^{-1}\mathscr{C}_+^* = \mathbb{1}$ left of $\chi^*(\boldsymbol{p})$ on the left

[1] Note that we omit the subscript "GN" in this section to ease notation.

hand side yields

$$\int \mathrm{d}^2\boldsymbol{p}\left[\delta(\boldsymbol{q}-\boldsymbol{p})(-\mathrm{i}\underbrace{\mathscr{C}_+^*\gamma_\mu^*\left(\mathscr{C}_+^*\right)^{-1}}_{=\gamma_\mu^\dagger=\gamma_\mu}p_\mu+\underbrace{\mathscr{C}_+^*\gamma_0^*\left(\mathscr{C}_+^*\right)^{-1}}_{=\gamma_0^\dagger=\gamma_0}\mu)+\tilde{\sigma}^*(\boldsymbol{q}-\boldsymbol{p})\right]\mathscr{C}_+^*\chi_j^*(\boldsymbol{p})=\lambda_j^*(\boldsymbol{q})\mathscr{C}_+^*\chi_j^*(\boldsymbol{q}). \tag{A.8}$$

This new eigenvalue equation leads to

$$\det Q[\sigma,\mu]=\det Q[-\sigma,-\mu]\overset{(A.6)}{=}\det Q[\sigma,-\mu], \tag{A.9}$$

showing that the determinant is also an even function of the chemical potential.

To show that $\det Q\in\mathbb{R}$ we apply the variable transformation $\boldsymbol{p},\boldsymbol{q}\to-\boldsymbol{p},-\boldsymbol{q}$ to Eq. (A.8)

$$\int \mathrm{d}^2\boldsymbol{p}\left[\delta(\boldsymbol{p}-\boldsymbol{q})(\mathrm{i}\gamma_\mu\boldsymbol{p}_\mu+\gamma_0\mu)+\underbrace{\tilde{\sigma}^*(\boldsymbol{p}-\boldsymbol{q})}_{\tilde{\sigma}(\boldsymbol{q}-\boldsymbol{p})}\right]\mathscr{C}_+^*\chi_j^*(-\boldsymbol{p}')=\lambda_j^*(-\boldsymbol{q})\mathscr{C}_+^*\chi_j^*(-\boldsymbol{q}), \tag{A.10}$$

where we assumed that $\sigma(\boldsymbol{x})\in\mathbb{R}$ and therefore $\tilde{\sigma}^*(\boldsymbol{p}-\boldsymbol{q})=\tilde{\sigma}(\boldsymbol{q}-\boldsymbol{p})$. On the left hand side $Q(\boldsymbol{q},\boldsymbol{p})$ is recovered and therefore is again an eigenvalue equation expressed through the original eigenvalues. Now we can conclude

$$\det Q=\prod_{\boldsymbol{q}}\prod_{j=1}^{2}\lambda_j(\boldsymbol{q})\overset{(A.10)}{=}\prod_{\boldsymbol{q}}\prod_{j=1}^{2}\lambda_j^*(-\boldsymbol{q})=\left(\prod_{\boldsymbol{q}}\prod_{j=1}^{2}\lambda_j(-\boldsymbol{q})\right)^*=\left(\prod_{\boldsymbol{q}}\prod_{j=1}^{2}\lambda_j(\boldsymbol{q})\right)^*=(\det Q)^*, \tag{A.11}$$

where we used that the momenta in the product are symmetric with respect to the origin.

A.2 Eigenvalues of the Gross-Neveu Model Dirac Operator for Homogeneous σ

Consider a generalization of Eq. (1.12) as a matrix

$$Q(\boldsymbol{x},\boldsymbol{y})\to Q^{A,B}(\boldsymbol{n}|\boldsymbol{m})=\mathbb{D}^A(\boldsymbol{n}|\boldsymbol{m})+\delta_{\boldsymbol{n},\boldsymbol{m}}\sum_{\boldsymbol{r}}\sigma(\boldsymbol{r})F^B(\boldsymbol{n}|\boldsymbol{r}), \tag{A.12}$$

where D^A is a general derivative of type A, F^B is a distribution function for σ of type B and the sum is representative for either a discrete sum or integral. The momentum representation of $Q^{A,B}(\boldsymbol{n}|\boldsymbol{m})$ is then

$$\tilde{Q}^{A,B}(\boldsymbol{p}|\boldsymbol{q})=\tilde{\mathbb{D}}^A(\boldsymbol{p}|\boldsymbol{q})+\frac{1}{\sqrt{|\Lambda|}}\sum_{\boldsymbol{p}'}\tilde{\sigma}(\boldsymbol{p}')\tilde{F}^B(\boldsymbol{p}-\boldsymbol{q}|\boldsymbol{p}'), \tag{A.13}$$

where $\tilde{\mathbb{D}}^A$, $\tilde{F}^B$, $\tilde{\sigma}$ are the Fourier transforms of $\mathbb{D}^A$, F^B, σ respectively. We continue this calculation with the assumption that $\tilde{\mathbb{D}}^A$, $\tilde{F}^B$ are diagonal in momentum space and σ is constant. Its Fourier transform is then $\tilde{\sigma}(\boldsymbol{p})=\sqrt{|\Lambda|}\delta_{\boldsymbol{p},\boldsymbol{0}}\sigma$. The matrix $\tilde{Q}$ then assumes the simpler form

$$\begin{aligned}\tilde{Q}^{A,B}(\boldsymbol{p}|\boldsymbol{q})&=\delta_{\boldsymbol{p},\boldsymbol{q}}\tilde{\mathbb{D}}^A(\boldsymbol{q})+\sum_{\boldsymbol{p}'}\delta_{\boldsymbol{p}',\boldsymbol{0}}\sigma\,\delta_{\boldsymbol{p}-\boldsymbol{q},\boldsymbol{p}'}\tilde{F}^B(\boldsymbol{p}-\boldsymbol{q})\\&=\delta_{\boldsymbol{p},\boldsymbol{q}}\left(\tilde{\mathbb{D}}^A(\boldsymbol{q})+\sigma\,\tilde{F}^B(0)\right).\end{aligned} \tag{A.14}$$

We assume that F^B is normalized such that $\tilde{F}^B(0) = 1$ and therefore omit it and the index B in the following. Since the matrix is diagonal in momentum space, we only need to determine the eigenvalues for the Dirac block matrix at $\boldsymbol{p}, \boldsymbol{q}$

$$\lambda_j^A(\boldsymbol{q})\,\chi_j(\boldsymbol{q}) = \tilde{Q}^{A,B}\left(\boldsymbol{p}|\boldsymbol{q}\right)\chi_j(\boldsymbol{q}) = \delta_{\boldsymbol{p},\boldsymbol{q}}\left(\tilde{\not{D}}^A\left(\boldsymbol{q}\right)+\sigma\right)\chi_j(\boldsymbol{q}) = \delta_{\boldsymbol{p},\boldsymbol{q}}\left(d_j^A(\boldsymbol{q})+\sigma\right)\chi_j(\boldsymbol{q}), \tag{A.15}$$

where $\lambda_j^A(\boldsymbol{q})$, $d_j^A(\boldsymbol{q})$ are the eigenvalues to eigenvector $\chi_j(\boldsymbol{q})$ of $\tilde{Q}^{A,B}\left(\boldsymbol{p}|\boldsymbol{q}\right)$, $\tilde{\not{D}}^A\left(\boldsymbol{q}\right)$respectively. The eigenvalues $d_j^A(\boldsymbol{q})$ can be found by applying $\tilde{\not{D}}^A\left(\boldsymbol{q}\right)$ twice to the eigenvector $\chi_j(\boldsymbol{q})$, i.e.

$$\left(d_j^A(\boldsymbol{q})\right)^2\chi_j(\boldsymbol{q}) = \tilde{\not{D}}^A\left(\boldsymbol{q}\right)\tilde{\not{D}}^A\left(\boldsymbol{q}\right)\chi_j(\boldsymbol{q}) = \tilde{D}_\mu^A\left(\boldsymbol{q}\right)\gamma_\mu\tilde{D}_\nu^A\left(\boldsymbol{q}\right)\gamma_\nu\chi_j(\boldsymbol{q}) = \tilde{D}_\mu^A\left(\boldsymbol{q}\right)\tilde{D}_\mu^A\left(\boldsymbol{q}\right)\chi_j(\boldsymbol{q}) \tag{A.16}$$

$$\Rightarrow\; d_\pm^A(\boldsymbol{q}) = \pm\sqrt{\tilde{D}_\mu^A\left(\boldsymbol{q}\right)\tilde{D}_\mu^A\left(\boldsymbol{q}\right)}, \tag{A.17}$$

where we used

$$\gamma_\mu a_\mu\gamma_\nu a_\nu = \frac{1}{2}\left(\gamma_\mu a_\mu\gamma_\nu a_\nu + \gamma_\nu a_\nu\gamma_\mu a_\mu\right) = \delta_{\mu,\nu}a_\mu a_\nu. \tag{A.18}$$

It then follows that the general eigenvalues are

$$\lambda_\pm^A(\boldsymbol{q}) = \sigma \pm \sqrt{\tilde{D}_\mu^A\left(\boldsymbol{q}\right)\tilde{D}_\mu^A\left(\boldsymbol{q}\right)}, \quad \lambda^A(\boldsymbol{q}) = \sigma^2 - \tilde{D}_\mu^A\left(\boldsymbol{q}\right)\tilde{D}_\mu^A\left(\boldsymbol{q}\right). \tag{A.19}$$

By setting, e.g. $D_\mu^A = \partial_\mu + \mu\delta_{\mu,0}$ we recover the known continuum eigenvalues

$$\lambda(\boldsymbol{q}) = \sigma^2 + (q_0 - \mathrm{i}\mu)^2 + q_1^2. \tag{A.20}$$

B Renormalization of the Effective Potential for Homogeneous σ in the Continuum

We start the discussion with the bosonized effective action S_{eff} from Eq. (1.35) and assume σ to be constant. We then define the effective potential

$$U_{\text{eff}}(\sigma) = \frac{1}{N_{\text{f}}\beta L_1} S_{\text{eff}} = \frac{1}{2\lambda}\sigma^2 - \frac{1}{\beta L_1} \ln \det Q. \tag{B.1}$$

We express $\det Q$ via the eigenvalues of Eq. (A.20)

$$\det Q = \prod_{p_1}\prod_{\omega_n} \beta^2 \left[(\omega_n - \mathrm{i}\mu)^2 + \varepsilon^2 \right] = \prod_{p_1} d(\beta, \mu, \varepsilon), \tag{B.2}$$

where $\varepsilon^2 = p_1^2 + \sigma^2$, the factor β^2 is a remnant of the momentum delta function in Eq. (A.14), and we renamed p_0 according to convention to ω_n, which are called the fermionic matsubara frequencies and are given by

$$\omega_n = \frac{2\pi}{\beta}\left(n + \frac{1}{2}\right) \quad \text{with} \quad n \in \mathbb{Z}. \tag{B.3}$$

We proceed to reshape d

$$\begin{aligned} d(\beta,\mu,\varepsilon) = \prod_{\omega_n} \beta^2 \left\{ (\omega_n - \mathrm{i}\mu)^2 + \varepsilon^2 \right\} &= \prod_{\omega_n} \beta \left\{ (\omega_n - \mathrm{i}\mu)^2 + \varepsilon^2 \right\}^{1/2} \prod_{-\omega_n} \beta \left\{ (\omega_n + \mathrm{i}\mu)^2 + \varepsilon^2 \right\}^{1/2} \\ &= \prod_{\omega_n} \beta^2 \left\{ \left[\varepsilon^2 + \omega_n^2 - \mu^2 \right]^2 + 4\mu^2\omega_n^2 \right\}^{1/2} \\ &= \prod_{\omega_n} \beta^2 \left\{ \left[(\varepsilon+\mu) \times (\varepsilon-\mu) + \omega_n^2 \right]^2 + 2\omega_n^2(\varepsilon^2+\mu^2) - 2\omega_n^2(\varepsilon^2-\mu^2) \right\}^{1/2} \\ &= \prod_{\omega_n} \beta^2 \left\{ \left[(\varepsilon-\mu)^2 + \omega_n^2 \right] \times \left[(\varepsilon+\mu)^2 + \omega_n^2 \right] \right\}^{1/2}, \end{aligned} \tag{B.4}$$

which we reinsert into the effective potential in Eq. (B.1) and thereby obtain

$$U_{\text{eff}}(\sigma) = \frac{1}{2\lambda}\sigma^2 - \frac{1}{\beta}\int \frac{\mathrm{d}p_1}{2\pi}\frac{1}{2}\sum_{n=-\infty}^{\infty} \left\{ \ln\left[\beta^2(\varepsilon-\mu)^2 + \pi^2(2n+1)^2 \right] + \ln\left[\beta^2(\varepsilon+\mu)^2 + \pi^2(2n+1)^2 \right] \right\}, \tag{B.5}$$

where the sum over p_1 is an integral since we consider infinite spatial volume and we inserted Eq. (B.3).

We proceed to rewrite the logarithm and perform the Mastubara sum:

$$\begin{aligned}
\frac{1}{2}\sum_{n=-\infty}^{\infty}\ln\left[\beta^2(\varepsilon\pm\mu)^2+\pi^2(2n+1)^2\right] &= \int_0^{\beta(\varepsilon\pm\mu)}\mathrm{d}x\,x\sum_{n=-\infty}^{\infty}\frac{1}{x^2+\pi^2(2n+1)^2}+\frac{1}{2}\ln\left[\pi^2(2n+1)^2\right] \\
&= \int_0^{\beta(\varepsilon\pm\mu)}\mathrm{d}x\,x\left[\sum_{n=0}^{\infty}\frac{1}{x^2+\pi^2(2n+1)^2}+\sum_{n=1}^{\infty}\frac{1}{x^2+\pi^2(2n-1)^2}\right] \\
&= \int_0^{\beta(\varepsilon\pm\mu)}\mathrm{d}x\,x\left[\sum_{n=1}^{\infty}\frac{1}{x^2+\pi^2(2n-1)^2}+\sum_{n=1}^{\infty}\frac{1}{x^2+\pi^2(2n-1)^2}\right] \\
&= \int_0^{\beta(\varepsilon\pm\mu)}\mathrm{d}x\,x\,\frac{2}{\pi^2}\sum_{n=1}^{\infty}\frac{1}{(x/\pi)^2+(2n-1)^2} \\
&= \int_0^{\beta(\varepsilon\pm\mu)}\mathrm{d}x\,x\,\frac{2}{4x}\tanh\frac{x}{2} = \int_0^{\beta(\varepsilon\pm\mu)}\mathrm{d}x\,\frac{1}{2}\tanh\frac{x}{2} \\
&= \int_0^{\beta(\varepsilon\pm\mu)}\mathrm{d}x\left(\frac{1}{2}-\frac{1}{\mathrm{e}^x+1}\right) = \frac{-\beta(\varepsilon\pm\mu)}{2}+\ln\left(1+\mathrm{e}^{\beta(\varepsilon\pm\mu)}\right) \\
&= \frac{\beta(\varepsilon\pm\mu)}{2}+\ln\left(1+\mathrm{e}^{-\beta(\varepsilon\pm\mu)}\right),
\end{aligned} \tag{B.6}$$

where we

- used the integral identity

$$\int\frac{x}{x^2+a^2} = \frac{1}{2}\ln(x^2+a^2), \tag{B.7}$$

- neglected the red term as it is a thermodynamically irrelevant constant,
- used the series identity (found, e.g. in Ref. [58])

$$\sum_{n=1}^{\infty}\frac{1}{x^2+(2n-1)^2} = \frac{\pi}{4x}\tanh\frac{\pi x}{2}. \tag{B.8}$$

The effective potential is then

$$U_{\mathrm{eff}}(\sigma) = \frac{1}{2\lambda}\sigma^2-\frac{1}{\beta}\int\frac{\mathrm{d}p_1}{2\pi}\left\{\beta\varepsilon+\ln\left(1+\mathrm{e}^{-\beta(\varepsilon+\mu)}\right)+\ln\left(1+\mathrm{e}^{-\beta(\varepsilon-\mu)}\right)\right\}, \tag{B.9}$$

where the green term is obviously UV-divergent. In order to renormalize the theory, we first calculate the so-called *gap equation* by minimizing the effective potential

$$0\overset{!}{=}\frac{\mathrm{d}U_{\mathrm{eff}}(\sigma)}{\mathrm{d}\sigma} = \frac{\sigma}{\lambda}-\int\frac{\mathrm{d}p_1}{2\pi}\frac{\sigma}{\varepsilon}\left\{1-\frac{1}{1+\mathrm{e}^{\beta(\varepsilon+\mu)}}-\frac{1}{1+\mathrm{e}^{\beta(\varepsilon-\mu)}}\right\}. \tag{B.10}$$

We regularize the theory by a spatial momentum cutoff Λ and require that the minimum of U_{eff} is at $\sigma_0>0$ for $T=0$ and $\mu=0$. The purple terms in Eq. (B.10) vanish for this μ, T and we obtain the simple expression

$$\frac{1}{\lambda} = 2\int_0^{\Lambda}\frac{\mathrm{d}p_1}{2\pi}\frac{1}{\sqrt{p_1^2+\sigma_0^2}} = \frac{1}{\pi}\operatorname{arsinh}\left(\frac{\Lambda}{\sigma_0}\right)\xrightarrow[\Lambda/\sigma_0\gg1]{}\frac{1}{\lambda} = \frac{1}{\pi}\ln\left(\frac{2\Lambda}{\sigma_0}\right), \tag{B.11}$$

which gives us a relation between the coupling λ, the cutoff Λ and the finite σ_0. We insert this into Eq. (B.9)

$$U_{\text{eff}}(\sigma) = \frac{\sigma^2}{2\pi}\ln\left(\frac{2\Lambda}{\sigma_0}\right) - \frac{2}{\beta}\int_0^\Lambda \frac{\mathrm{d}p_1}{2\pi}\left\{\beta\varepsilon + \ln\left(1+\mathrm{e}^{-\beta(\varepsilon+\mu)}\right) + \ln\left(1+\mathrm{e}^{-\beta(\varepsilon-\mu)}\right)\right\}. \tag{B.12}$$

We calculate the green part first

$$\int_0^\Lambda \frac{\mathrm{d}p_1}{\pi}\varepsilon = \frac{1}{2\pi}\left[\Lambda^2\sqrt{(\sigma/\Lambda)^2+1} + \sigma^2\,\mathrm{arsinh}\left(\frac{\Lambda}{|\sigma|}\right)\right] \xrightarrow[|\sigma|/\Lambda\ll 1]{} \frac{1}{2\pi}\left[\Lambda^2\left(1+\frac{\sigma^2}{2\Lambda^2}\right) + \sigma^2\ln\left(\frac{2\Lambda}{|\sigma|}\right)\right], \tag{B.13}$$

where we neglect the red term in the following as it is again a thermodynamically irrelevant constant.

We rewrite the purple term in Eq. (B.12) as

$$\begin{aligned}\frac{1}{\pi\beta}\int_0^\Lambda \mathrm{d}p_1 \left\{\ln\left(1+\mathrm{e}^{-\beta(\varepsilon+\mu)}\right) + \ln\left(1+\mathrm{e}^{-\beta(\varepsilon-\mu)}\right)\right\} = \\ -\frac{1}{\pi}\int_0^\Lambda \mathrm{d}p_1 \frac{p_1^2}{\varepsilon}\left[\frac{-1}{1+\mathrm{e}^{\beta(\varepsilon+\mu)}} + \frac{-1}{1+\mathrm{e}^{\beta(\varepsilon-\mu)}}\right] \\ + \frac{p_1}{\pi\beta}\left[\ln\left(1+\mathrm{e}^{-\beta(\varepsilon+\mu)}\right) + \ln\left(1+\mathrm{e}^{-\beta(\varepsilon-\mu)}\right)\right]\Bigg|_{p_1=0}^{p_1=\Lambda},\end{aligned} \tag{B.14}$$

where the green integral is finite for $\Lambda\to\infty$ and the red term vanishes at the evaluation points for $\Lambda/\sigma \gg 1$.

Inserting Eqs. (B.13) and (B.14) into Eq. (B.12) results in the properly renormalized effective potential

$$U_{\text{eff}}(\sigma) = \frac{\sigma^2}{2\pi}\left[\ln\left(\frac{|\sigma|}{\sigma_0}\right) - 2\right] - \frac{1}{\pi}\int_0^\infty \mathrm{d}p_1 \frac{p_1^2}{\varepsilon}\left(\frac{1}{1+\mathrm{e}^{\beta(\varepsilon+\mu)}} + \frac{1}{1+\mathrm{e}^{\beta(\varepsilon-\mu)}}\right). \tag{B.15}$$

Although we minimize this effective potential numerically to calculate the whole phase diagram, we want to derive the critical temperature T_c for $\mu = 0$ analytically. To do so, we use the gap equation from Eq. (B.10)

$$\ln\left(\frac{\sigma}{\sigma_0}\right) = -2\int_0^\infty \mathrm{d}p_1 \frac{1}{\varepsilon}\frac{1}{1+\mathrm{e}^{\beta_c\varepsilon}} = +\int_0^\infty \mathrm{d}p_1 \frac{1}{\varepsilon}\left[\tanh\left(\frac{\varepsilon\beta_c}{2}\right) - 1\right], \tag{B.16}$$

where we set $\mu = 0, \beta = \beta_c$ and used the condition Eq. (B.11). We are interested in the transition temperature for which there is a non-trivial solution of the gap equation and thus assume σ to be small (as σ vanishes smoothly), thereby approximating the right hand side as (we follow the prescription in Ref. [59] for the approximation)

$$\begin{aligned}&\int_0^\infty \mathrm{d}p_1\left[p_1^{-1}\tanh\left(\frac{p_1\beta_c}{2}\right) - \frac{1}{\varepsilon}\right] \\ &\quad= \int_0^\infty \mathrm{d}y\, y^{-1}\tanh(y) - \int_0^\infty \mathrm{d}p_1 \frac{1}{\sigma\sqrt{(p_1/\sigma)^2+1}} \\ &\quad= \left[\ln\left(\frac{p_1\beta_c}{2}\right)\tanh\left(\frac{p_1\beta_c}{2}\right)\right]_{p_1=0}^{p_1=\infty} \underbrace{-\int_0^\infty \mathrm{d}y\,\ln(y)\,\mathrm{sech}^2(y)}_{=\ln(4\mathrm{e}^\gamma/\pi)} - \left[\mathrm{arsinh}\left(\frac{p_1}{\sigma}\right)\right]_{p_1=0}^{p_1=\infty} \\ &\quad= \underbrace{\left[\ln\left(\frac{p_1\beta_c}{2}\right)\tanh\left(\frac{p_1\beta_c}{2}\right) - \ln\left(\frac{p_1}{\sigma} + \sqrt{(p_1/\sigma)^2+1}\right)\right]_{p_1=0}^{p_1=\infty}}_{\overset{p_1=0}{=}0} + \ln\left(\frac{4\mathrm{e}^\gamma}{\pi}\right)\end{aligned}$$

$$= \left[\underbrace{\ln(p_1)\left(\tanh(\frac{p_1\beta_c}{2})-1\right)}_{\xrightarrow{p_1\to\infty}0} + \ln\left(\frac{\beta_c}{2}\right)\underbrace{\tanh\left(\frac{\beta_c p_1}{2}\right)}_{\xrightarrow{p_1\to\infty}1} - \ln\left(\frac{2}{\sigma}\right)\right]^{p_1=\infty} + \ln\left(\frac{4\mathrm{e}^{\gamma}}{\pi}\right)$$

$$= \ln\left(\frac{\beta_c \sigma \mathrm{e}^{\gamma}}{\pi}\right), \tag{B.17}$$

where $\gamma = 0.57721\ldots$ is the *Euler-Mascheroni* constant. We insert this expression into Eq. (B.16) and obtain the critical temperature

$$T_c = \sigma_0 \frac{\mathrm{e}^{\gamma}}{\pi}. \tag{B.18}$$

C Notes on the Naively Discretized Gross-Neveu Model

C.1 Minimization of U_{eff} in the Naive Discretization for Homogeneous σ

In this section, we briefly cover the necessary numerical steps in order to calculate the homogeneous large-N_{f} phase diagram in the naive discretization. The ease notation we express everything in dimensionless lattice quantities e.g. $a\sigma \to \sigma$. Just as in the continuum, we have to minimize the effective potential with respect to σ. This effective potential for homogeneous σ is given by

$$U_{\text{eff}}^{\text{ND}} = \frac{1}{2\lambda}\sigma^2 - \frac{1}{L_0 L_1} \ln \det Q^{\text{ND}}, \tag{C.1}$$

where $\det Q^{\text{ND}}$ can be calculated with the help of Eq. (A.19) to be

$$\det Q^{\text{ND}} = \prod_{p_0 \in \tilde{\Lambda}} \prod_{p_1 \in \tilde{\Lambda}} \left(\sigma^2 + \sin^2\left(p_0 - \mathrm{i}\mu\right) + \sin^2\left(p_1\right) \right). \tag{C.2}$$

In the homogeneous case, the shape of the effective potential is rather simple and the minimization is not very complicated. Figures 1.1b and 1.1c show that we have to distinguish two cases. The first being that U_{eff} has a single minimum either at $\sigma = 0$ or smoothly connected to $\sigma = 0$ without a potential barrier and the other case being that there are two competing minima separated by a potential barrier. Algorithm 1 depicts the algorithm that we employ in the function `minimize` that minimizes the effective potential in the interval $[0, \sigma_u]$. See Ref. [60] for a description of the golden section search that is used in the minimization. Every following minimization of the effective potential is carried out in this way. If σ_0 is known, the default upper boundary given to `minimize` is $\sigma_u = 1.1 \times \sigma_0$.

The calculation of the phase diagram can then be characterized in two steps:

1. *Determine the right λ for the desired $a\sigma_0$.*

   We choose the value of $a\sigma_0$ for which we want to determine the phase diagram. Then we perform a bisection (see, e.g. Ref. [60] for a description of the algorithm) and search the root of the function $f(\lambda') = \texttt{minimize}(\lambda = \lambda') - \sigma_0$, where the σ_u given to `minimize` is chosen reasonably large. The determined λ' then produces the desired σ_0 and is then used in the next step.

2. *Determination of the phase boundary.*

   We fix the temporal extent N_0 and then perform kind of a bisection search in the interval $\mu \in [\mu_{l,0}, \mu_{b,0}]$ to minimize $g(\mu_l, \mu_u) = |\mu_u - \mu_l|$ with the constraints $\texttt{minimize}(\mu = \mu_l) \neq 0$, $\texttt{minimize}(\mu = \mu_u) = 0$ and the precision $|\mu_u - \mu_l| < \varepsilon$. The midpoint $\mu = (\mu_b + \mu_s)/2$ is then the critical chemical potential for the respective temperature. Algorithm 2 depicts this procedure.

Algorithm 1: Function `minimize` that is used to minimize the effective potential.

Require: a function `ueff(`σ`)` that calculates the effective potential for the physical parameters given to `minimize`, a function `minimizeInt(`σ_1, σ_2`)` that minimizes the effective potential with the golden section search in the interval $[\sigma_1, \sigma_2]$ and returns the minimzing σ for the physical parameters given to `minimizes`,

Input: upper bound for the minimization σ_u, physical parameters

for $\sigma = 0$ **to** $\sigma = \sigma_u$ **do**
  Calculate `ueff(`σ`)` and the numerical derivative
end
if *Sign of derivative changes from* + *to* - **then**
  Maximum in the interval
  σ_1'=`minimizeInt(`$0, 0.5 \times \sigma_u$`)`
  σ_2'=`minimizeInt(`$0.5 \times \sigma_u, \sigma_u$`)`
  σ_3'=`minimizeInt(`$0.8 \times \sigma_u, \sigma_u$`)`
  σ_4'=0
  return σ' *with the smallest* `ueff(`σ'`)`
else
  No Maximum in the interval
  σ_1'=`minimize(`$0, \sigma_u$`)`
  σ_2'=0
  return σ' *with the smallest* `ueff(`σ'`)`
end

Algorithm 2: Determination of the critical chemical potential for fixed temperature.

Result: Critical chemical potential
Input: lower bound $\mu_{l,0}$ with $\sigma_{l,0}$=`minimize(`$\mu = \mu_{l,0}$`)` $\neq 0$,
upper bound $\mu_{u,0}$ with $\sigma_{u,0}$=`minimize(`$\mu = \mu_{u,0}$`)` $== 0$, the precision ε
μ_u=$\mu_{u,0}$
μ_l=$\mu_{l,0}$
while $|\mu_u - \mu_l| > \varepsilon$ **do**
  $\mu' = (\mu_l + \mu_u)/2$
  σ_m=`minimize(`$\mu = \mu'$`)`
  if $\sigma_m > 0$ **then**
    $\mu_l = \mu$
  else
    $\mu_u = \mu$
  end
end
return $(\mu_l + \mu_u)/2$

C.2 Odd Lattice Extents in the Naively Discretized Gross-Neveu Model

We illustrate the effects of odd lattice extents on the effective potential of the naively discretized GN model by considering $\sigma = 0$ and $\mu = 0$ as the distortion of the potential is then most severe. The determinant of the Dirac operator $\det Q^{\mathrm{ND}}$ from Eq. (C.2) is then

$$\det Q^{\mathrm{ND}} = \prod_{\tilde{n}_0=0}^{N_0-1} \prod_{\tilde{n}_1=0}^{N_1-1} \left(\underbrace{\sin^2\left((2\tilde{n}_0+1)\frac{\pi}{N_0} \right)}_{:=A_0} + \underbrace{\sin^2\left(2\tilde{n}_1 \frac{\pi}{N_1} \right)}_{:=A_1} \right), \tag{C.3}$$

where we chose an asymmetric first Brillouin zone as we are not interested in the continuum limit and this choice eases notation. The term A_1 is zero for $\tilde{n}_1' = 0, N_1/2$. Only for an even N_1 is the latter value an integer and thus realized. We separate these special $\tilde{n}_1'$ from the product in Eq. (C.3) and thereby obtain

$$\det Q^{\mathrm{ND}} = \left(\prod_{\tilde{n}_0=0}^{N_0-1} A_0^{\#} \right) \prod_{\tilde{n}_0=0}^{N_0-1} \prod_{\substack{\tilde{n}_1=0 \\ \tilde{n}_1 \neq \tilde{n}_1'}}^{N_1-1} \left(A_0 + A_1 \right) \quad \text{with} \quad \# = \begin{cases} 1 & \text{if } N_1 \text{ is odd.} \\ 2 & \text{if } N_1 \text{ is even.} \end{cases} . \tag{C.4}$$

The term A_0 is zero for the special $\tilde{n}_0' = (N_0 - 1)/2$, which is realized for odd N_0. This results in $\det Q^{\mathrm{ND}} = 0$ and thus introduces divergences into the effective potential, because $U_{\mathrm{eff}}^{\mathrm{ND}} \propto \ln \det Q^{\mathrm{ND}}$. For N_0 even, there are no zero modes as $(N_0 - 1)/2$ is not integer and therefore $A_0 \neq 0$ for all possible $\tilde{n}_0$.

An odd N_0 also deforms the effective potential $U_{\mathrm{eff}}^{\mathrm{ND}}$ for $\sigma \neq 0$. Figure C.1a shows this effect for homogeneous σ, where the effective potential for odd N_1 is considerably deformed around $\sigma = 0$. An artificially potential barrier of infinite height arises at $\sigma = 0$ and the minimum is also at an incorrect position. The deformation compared to even N_0 is expected to be weaker for large N_0, which is confirmed by Figure C.1b, where the deviation from even N_0 is limited to small σ. Large volumes cause the boundary conditions to lose importance and therefore for temperature $T = 0$ this effect should vanish completely. For high temperatures that belong to the SP, odd N_0 also cause a divergence at $\sigma = 0$ that prevents the minimum of U_{eff} to be at $\sigma = 0$ and thus the restoration of chiral symmetry (compare Figure C.1c). The minimum is then at even larger $\sigma > \sigma_0$, which diverges for $T \to \infty$ as illustrated in Figure C.1d.[1] This effect was also observed in Ref. [2], where temporal periodic boundary conditions for the fermions were assumed on purpose.

[1] Note that the upper bound of the minimizing interval of σ defined in Appendix C.1 clearly has to be expanded for odd N_0 as the minimum can be $\sigma \gg \sigma_0$.

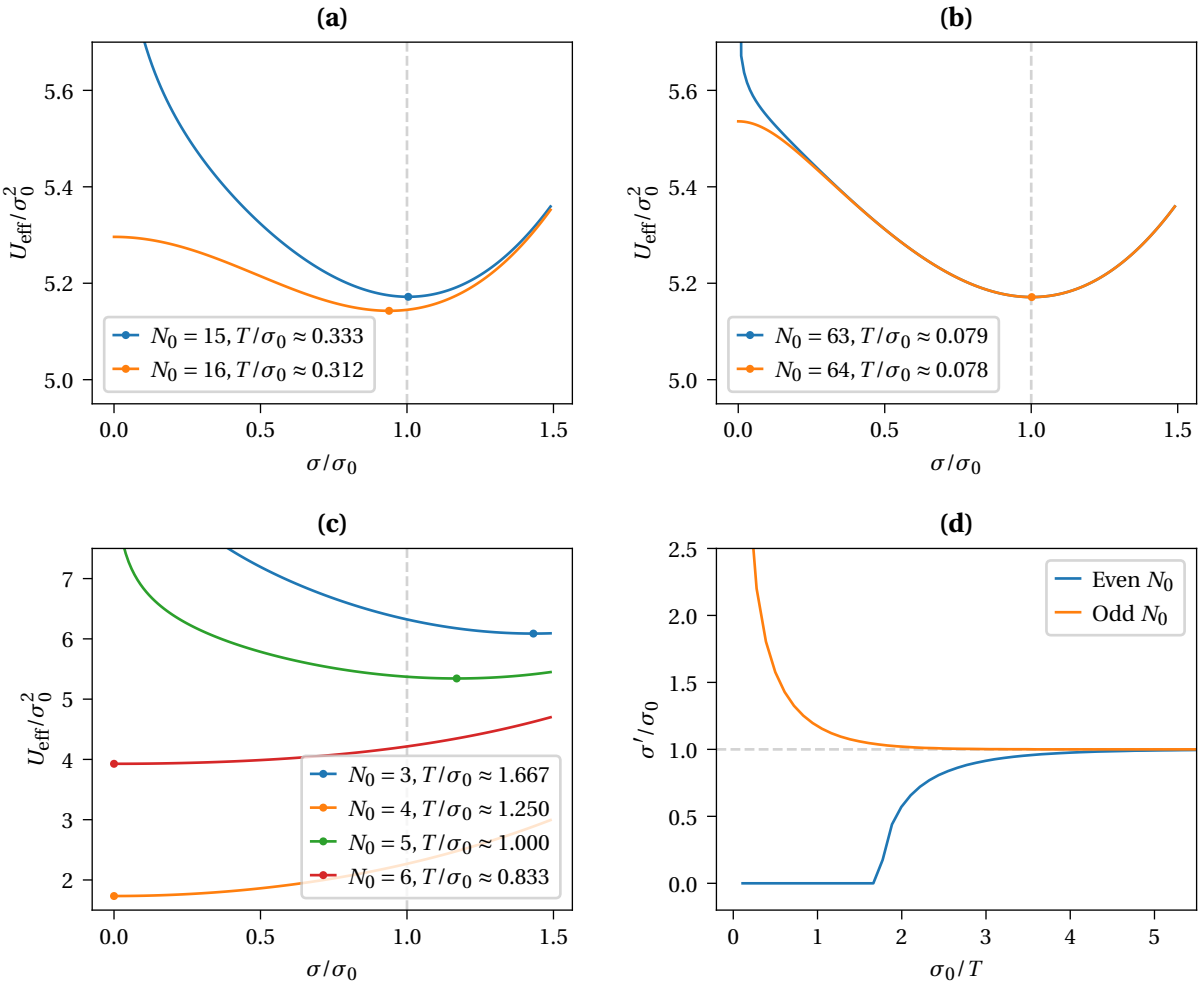

Figure C.1: **(a)**-**(c)** U_{eff} for homogeneous σ in $1+1$-dimensional GN in the ND discretization with $\mu = 0$, $a = 0.2/\sigma_0$ and $N_1 = 64$. The minima are indicated by a dot. **(a)** $N_0 = 15, 16$. **(b)** $N_0 = 63, 64$. **(c)** $N_0 = 4, 5, 6$. **(d)** Temperature scan of the minimum of the effective action $\sigma' = \min_{\sigma} U_{\text{eff}}^{\text{ND}}$ for $a \approx 0.055/\sigma_0$, $N_1 = 256$ and even/odd temporal lattice extents N_0.

D Benchmark Model Calculations

D.1 Preceding Remarks and Notation

This section serves to introduce the needed tools for the benchmark model calculation and its contents are based on Ref. [61].

Basic Notation Regarding Random Variables and Related Quantities

The expectation value of an observable O with respect to a continuous random variable X is calculated as

$$\langle O \rangle_X = \int_{-\infty}^{\infty} \mathrm{d}X \; p_X(X) \; O(X) \tag{D.1}$$

and for an integer random variable X as

$$\langle O \rangle_X = \sum_{X=-\infty}^{\infty} p_X(X) \; O, \tag{D.2}$$

where we call p_X the *probability density function* (PDF) of the random variable X and we assume in the following that all PDFs are normalized such that

$$\int_{-\infty}^{\infty} \mathrm{d}X \; p_X(X) = 1. \tag{D.3}$$

The expectation value with respect to all random variables is simply denoted as $\langle O \rangle$.

Of particular interest is the Gaussian distribution denoted as $\mathcal{N}(\mu, \sigma^2)$ with mean μ, variance σ^2 and PDF as

$$p(x \,|\, \mu, \sigma^2) = \frac{1}{\sqrt{2\pi\sigma^2}} \exp\left(- \frac{(x-\mu)^2}{2\sigma^2} \right). \tag{D.4}$$

The special case of $\mathcal{N}(0,1)$ is called the normal distribution. The PDF for two independent Gaussian distributed random variables X_1, X_2 is

$$p_X(x_1, x_2) = \frac{1}{2\pi\sigma_1\sigma_2} \exp\left(- \frac{(x_1-\mu_1)^2}{2\sigma_1^2} - \frac{(x_2-\mu_2)^2}{2\sigma_2^2} \right) = p_{X_1}(x_1 | \mu_1, \sigma_1^2) \cdot p_{X_2}(x_2 | \mu_2, \sigma_2^2). \tag{D.5}$$

Rescaled Random Variables

Consider the random variable $Y = aX$ with X being a random variable with PDF $p_X(u)$ and $a \in \mathbb{C}$. Then it holds for the PDF of Y that

$$p_Y(u) = \frac{1}{a} p_X(u/a). \tag{D.6}$$

If X is normally distributed according to $p_X(x|\mu,\sigma^2)$, the PDF of Y is then

$$p_Y(u) = p_X(u|a\mu, a^2\sigma^2). \tag{D.7}$$

Sum of Normal Random Variables

Consider N independent Gaussian distributed random variables X_i with $i = 0,1,\ldots,N-1$ with $\mathcal{N}_{X_i}(\mu_i,\sigma_i^2)$ and their sum $Z = \sum_{i=0}^{N-1} X_i$. Then Z is a random variable that is also Gaussian distributed with

$$\mathcal{N}_Z\left(\sum_{i=0}^{N-1}\mu_i, \sum_{i=0}^{N-1}\sigma_i^2\right). \tag{D.8}$$

D.2 Squared Spacetime Average Σ^2

In the first step we calculate the spacetime average of the full model ς

$$\begin{aligned}\bar{\varsigma} &= \frac{1}{|\Lambda|}\sum_{\boldsymbol{x}\in\Gamma}\left(A\cos\left(\frac{2\pi}{L_1}(x_1+\delta x)(q+\delta q)\right) + B\sigma_0 + \varepsilon\eta(\boldsymbol{x})\right)\\ &= \frac{A}{|\Lambda|}\underbrace{\sum_{\boldsymbol{x}\in\Gamma}\cos\left(\frac{2\pi}{L_1}(x_1+\delta x)(q+\delta q)\right)}_{=0} + \frac{1}{|\Lambda|}\sum_{\boldsymbol{x}\in\Gamma}\left(B\sigma_0+\varepsilon\eta(\boldsymbol{x})\right) = B\sigma_0 + \frac{1}{|\Lambda|}\sum_{\boldsymbol{x}\in\Gamma}\eta'(\boldsymbol{x}) = B\sigma_0 + \bar{\eta}',\end{aligned} \tag{D.9}$$

where according to Eq. (D.8) and Eq. (D.7) $\bar{\eta}'$ is also a Gaussian distributed random variable with the PDF $p_{\bar{\eta}'}(\bar{\eta}'|0,\varepsilon^2/|\Lambda|)$. Now we can calculate the ensemble average of $\bar{\varsigma}^2$ as

$$\left\langle\bar{\varsigma}^2\right\rangle = \int_{-\infty}^{\infty} \mathrm{d}\bar{\eta}'\left(B^2\sigma_0^2 + B\sigma_0\bar{\eta}' + (\bar{\eta}')^2\right)p(\bar{\eta}'|0,\varepsilon^2/|\Lambda|) = B^2\sigma_0^2 + 0 + \frac{\varepsilon^2}{|\Lambda|^2}, \tag{D.10}$$

where we neglected the integration over the random variables $\delta q, \delta x$ since the observable does not depend on them anymore and thus the integrals separate. For the different phases Σ^2_ς is then

$$\Sigma^2_{\varsigma_{\mathrm{SP}}} = \frac{\varepsilon^2}{|\Lambda|\sigma_0^2} \qquad \text{in the SP,} \tag{D.11a}$$

$$\Sigma^2_{\varsigma_{\mathrm{HBP}}} = B^2 + \frac{\varepsilon^2}{|\Lambda|\sigma_0^2} \qquad \text{in the HBP,} \tag{D.11b}$$

$$\Sigma^2_{\varsigma_{\mathrm{IP}}} = \frac{\varepsilon^2}{|\Lambda|\sigma_0^2} \qquad \text{in the IP.} \tag{D.11c}$$

D.3 Fourier Transformed Chiral Condensate $\tilde{\Sigma}^2$

We start with calculating the spatial FT of ς

$$\begin{aligned}
\tilde{\varsigma}(x_0,k) &= \frac{1}{\sqrt{N_1}} \sum_{x_1\in\Gamma_1} \left[A\cos\left(\frac{2\pi}{L_1}(x_1+\delta x)(q+\delta q)\right) + B\sigma_0 + \varepsilon\eta(\boldsymbol{x}) \right] \mathrm{e}^{-\mathrm{i}kx_1} \\
&= \frac{A}{2\sqrt{N_1}} \sum_{x_1\in\Gamma_1} \left[\exp\left(\mathrm{i}\frac{2\pi}{L_1}(x_1+\delta x)(q+\delta q)\right) + \exp\left(-\mathrm{i}\frac{2\pi}{L_1}(x_1+\delta x)(q+\delta q)\right) \right] \mathrm{e}^{-\mathrm{i}kx_1} \\
&\quad + \sqrt{N_1}B\sigma_0 + \frac{\varepsilon}{\sqrt{N_1}} \sum_{x_1\in\Gamma_1} \left[\eta(\boldsymbol{x})\cos(kx_1) - \mathrm{i}\eta(\boldsymbol{x})\sin(kx_1)\right] \\
&= \frac{A\sqrt{N_1}}{2} \left[\delta_{2\pi(\delta q+q)/L_1,k} \exp\left(\mathrm{i}\underbrace{\frac{2\pi}{L_1}(q+\delta q)}_{=k}\delta x\right) - \delta_{2\pi(\delta q+q)/L_1,-k} \exp\left(-\mathrm{i}\underbrace{\frac{2\pi}{L_1}(q+\delta q)}_{=-k}\delta x\right) \right] \\
&\quad + \sqrt{N_1}B\sigma_0 + \underbrace{\mathrm{Re}\left(\tilde{\eta}'(x_0,k)\right)}_{:=R} + \mathrm{i}\underbrace{\mathrm{Im}\left(\tilde{\eta}'(x_0,k)\right)}_{:=I} \\
&= \frac{A\sqrt{N_1}}{2} \mathrm{e}^{\mathrm{i}k\delta x} \left(\delta_{2\pi(\delta q+q)/L_1,k} - \delta_{2\pi(\delta q+q)/L_1,-k}\right) + \sqrt{N_1}B\sigma_0 + R + \mathrm{i}\,I,
\end{aligned} \tag{D.12}$$

where R, I are sums of rescaled independent normal distributed variables with variances calculated as

$$\mathrm{var}(R) = \frac{\varepsilon^2}{N_1} \sum_{x_1\in\Gamma_1} \cos^2\left(\frac{2\pi\tilde{n}x_1}{L_1}\right) = \begin{cases} \varepsilon^2 & \text{if } \tilde{n} = mN_1/2, \text{ with } m\in\mathbb{Z} \\ \varepsilon^2/2 & \text{otherwise} \end{cases}, \tag{D.13}$$

$$\mathrm{var}(I) = \frac{\varepsilon^2}{N_1} \sum_{x_1\in\Gamma_1} \sin^2\left(\frac{2\pi\tilde{n}x_1}{L_1}\right) = \begin{cases} 0 & \text{if } \tilde{n} = mN_1/2, \text{ with } m\in\mathbb{Z} \\ \varepsilon^2/2 & \text{otherwise} \end{cases}, \tag{D.14}$$

where we represented the physical momentum k by $2\pi\tilde{n}/L_1$ with $\tilde{n}\in[-N_1/2, N_1/2-1]$ (compare Eq. (2.5)) in order to calculate the result of the sum. Before we continue with calculating the ensemble averages, we remark on the independence of R and I.

Independence of $\mathrm{Re}\left(\tilde{\boldsymbol{\eta}}'(\boldsymbol{x_0},\boldsymbol{k})\right)$ and $\mathrm{Im}\left(\tilde{\boldsymbol{\eta}}'(\boldsymbol{x_0},\boldsymbol{k})\right)$

Any function can be represented as a linear combination of its even and odd part $f(x) = f_e(x) + f_o(x)$, with $f_{e,o} = (f(x)\pm f(-x))/2$. In the FT $\tilde{f}$ of a real function f only the even part f_e contributes to the real part of $\tilde{f}$ and only its odd part f_o to the imaginary part of $\tilde{f}$. Therefore, an independent f_e and f_o results in an independent real and imaginary part of $\tilde{f}$.

Now consider two independent normal distributed random variables X_1, X_2 and the transformation

$$Y_{1,2} = \frac{1}{2}(X_1 \pm X_2),\ X_{1,2} = (Y_1 \pm Y_2). \tag{D.15}$$

Since X_1 and X_2 are normal distributed and independent, they have a common bivariate normal distribution. According to Eq. (D.5) their joint PDF is trivially the product of their PDFs

$$p_{X_1,X_2}(x_1,x_2) = p_{X_1}(x_1\,|\,0,1)\,p_{X_2}(x_2\,|\,0,1). \tag{D.16}$$

Now we can apply the transformation from (D.15) to this joint PDF of $Y_{1,2}$ (compare

with Ref. [61])

$$\begin{aligned} p_{Y_1,Y_2}(y_1,y_2) &= p_{X_1,X_2}(g_1(y_1,y_2),g_2(y_1,y_2))\,|J| \\ &= (2\pi)^{-1}\exp(-((y_1+y_2))^2/2)\cdot\exp(-((y_1-y_2))^2/2)\cdot 2 \\ &= ((\pi)^{-1/2}\exp(-y_1^2))\cdot((\pi)^{-1/2}\exp(-y_2^2)) = p_{Y_1}(y_1\,|\,0,1/2)\cdot p_{Y_2}(y_2\,|\,0,1/2), \end{aligned} \tag{D.17}$$

with $g_{1,2}(y_1,y_2)=(y_1\pm y_2)$ and $|J|$ as the determinant of the Jacobian matrix of this transformation. The factorization of $f_{Y_1,Y_2}(y_1,y_2)$ into two independent normal distributions together with the fact that they are sums of independent normal variables shows the independence of $Y_{1,2}$ (see Ref. [61]). If we set $X_1=\eta(x_0,x_1)$, $X_2=\eta(x_0,-x_1)$, we have shown the independence of the spatial even and odd part of $\eta(x_0,x_y)$ for fixed x_0 and consequently the independence of the real and imaginary part of $\tilde{\eta}'(x_0,k)$.

Ensemble Average of $|\tilde{\varsigma}(x_0,k)|^2$

We proceed to calculate the ensemble average of $|\tilde{\varsigma}(x_0,k)|^2$

$$\begin{aligned} \left\langle|\tilde{\varsigma}(x_0,k)|^2\right\rangle &= \left\langle\left|\frac{A\sqrt{N_1}}{2}\,\mathrm{e}^{\mathrm{i}\,k\delta x}\left(\delta_{2\pi(\delta q+q)/L_1,k}-\delta_{2\pi(\delta q+q)/L_1,-k}\right)+\sqrt{N_1}B\sigma_0+R+\mathrm{i}\,I\right|^2\right\rangle \\ &= \left\langle\frac{A^2N_1}{4}\left(\delta_{2\pi(\delta q+q)/L_1,k}+\delta_{2\pi(\delta q+q)/L_1,-k}+\delta_{\delta q,-q}\delta_{k,0}\right)+B^2\sigma_0^2N_1+R^2+I^2\right\rangle \\ &= \frac{A^2N_1}{4}\left(p_q\left[k-\frac{2\pi}{L_1}q|0,\Delta q^2\right)+p_q\left(k-\frac{2\pi}{L_1}+q|0,\Delta q^2\right)+p_q(q|0,\Delta q^2)\,\delta_{k,0}\right] \\ &\quad + B^2\sigma_0^2N_1+\underbrace{\mathrm{var}(R)+\mathrm{var}(I)}_{=\varepsilon^2} \\ &\approx \frac{A^2N_1}{4}\left[p_q\left(k-\frac{2\pi}{L_1}q|0,\Delta q^2\right)+p_q\left(k-\frac{2\pi}{L_1}+q|0,\Delta q^2\right)\right]+B^2\sigma_0^2N_1+\varepsilon^2, \end{aligned} \tag{D.18}$$

where we used that the independence of all random variables results in the vanishing of terms that are linear in a symmetrically distributed random variables and used that $q\gg\delta q$ to neglect the term proportional to $p_q(q|0,\Delta q^2)$. The result clearly does not depend on x_0 anymore; therefore, we can read off $\tilde{\Sigma}^2_\varsigma$ for the different phases

$$\tilde{\Sigma}^2_{\varsigma_{\mathrm{SP}}} = \frac{\varepsilon^2}{\sigma_0^2} \qquad \text{in the SP,} \tag{D.19a}$$

$$\tilde{\Sigma}^2_{\varsigma_{\mathrm{HBP}}} = B^2N_1+\frac{\varepsilon^2}{\sigma_0^2} \qquad \text{in the HBP,} \tag{D.19b}$$

$$\tilde{\Sigma}^2_{\varsigma_{\mathrm{IP}}} = \frac{A^2N_1}{4\sigma_0^2}\left[p_q\left(k-\frac{2\pi}{L_1}q\right)+\left(k+\frac{2\pi}{L_1}q\right)\right]+\frac{\varepsilon^2}{\sigma_0^2} \qquad \text{in the IP.} \tag{D.19c}$$

D.4 Spatial Correlator

We calculate the product $\varsigma(y_0,y)\varsigma(y_0,y+x)$:

$$\begin{aligned}
&\varsigma(y_0,y)\varsigma(y_0,y+x) = \\
&\quad = A^2\cos\left(\frac{2\pi}{L_1}(y+\delta y)(q+\delta q)\right)\cos\left(\frac{2\pi}{L_1}(y+\delta y+x_1)(q+\delta q)\right) \\
&\quad + B\sigma_0 A\left[\cos\left(\frac{2\pi}{L_1}(y+\delta y)(q+\delta q)\right)+\cos\left(\frac{2\pi}{L_1}(y+\delta y+x_1)(q+\delta q)\right)\right] \\
&\quad + \varepsilon A\left[\eta(y_0,y+x)\cos\left(\frac{2\pi}{L_1}(y+\delta y)(q+\delta q)\right)+\eta(y_0,y)\cos\left(\frac{2\pi}{L_1}(y+\delta y+x_1)(q+\delta q)\right)\right] \\
&\quad + B^2\sigma_0^2+\varepsilon B\sigma_0\left(\eta(y_0,y)+\eta(y_0,y+x)\right)+\varepsilon^2\eta(y_0,y)\,\eta(y_0,y+x),
\end{aligned} \tag{D.20}$$

where we renamed the random variable δx to δy to avoid confusion.

D.4.1 Ensemble Averages over $\eta,\delta q$

We continue by taking the ensemble averages only over η and δq

$$\begin{aligned}
&\langle\varsigma(y_0,y)\varsigma(y_0,y+x)\rangle_{\eta,\delta q} = \\
&\quad = A^2\underbrace{\left\langle\cos\left(\frac{2\pi}{L_1}(y+\delta y)(q+\delta q)\right)\cos\left(\frac{2\pi}{L_1}(y+\delta y+x_1)(q+\delta q)\right)\right\rangle_{\delta q}}_{:=P} \\
&\quad + B\sigma_0 A\underbrace{\left\langle\cos\left(\frac{2\pi}{L_1}(y+\delta y)(q+\delta q)\right)+\cos\left(\frac{2\pi}{L_1}(y+\delta y+x_1)(q+\delta q)\right)\right\rangle_{\delta q}}_{:=S} \\
&\quad + \varepsilon A\left\langle\underbrace{\langle\eta(y_0,y+x)\rangle_\eta}_{=0}\cos\left(\frac{2\pi}{L_1}(y+\delta y)(q+\delta q)\right)+\underbrace{\langle\eta(y_0,y)\rangle_\eta}_{=0}\cos\left(\frac{2\pi}{L_1}(y+\delta y+x_1)(q+\delta q)\right)\right\rangle_{\delta q} \\
&\quad + B^2\sigma_0^2+\varepsilon B\sigma_0\underbrace{\langle\eta(y_0,y)+\eta(y_0,y+x)\rangle_\eta}_{=0}+\varepsilon^2\underbrace{\langle\eta(y_0,y)\,\eta(y_0,y+x)\rangle_\eta}_{=\delta_{x,0}\,\mathrm{var}(\eta(y_0,y))=\delta_{x,0}} \\
&\quad = A^2P+B\sigma_0 AS+B^2\sigma_0^2+\varepsilon^2\delta_{x,0} = \langle c_\varsigma(x,y)\rangle_{\eta,\delta q},
\end{aligned} \tag{D.21}$$

where the result does not depend on y_0 anymore, thus we are able to identify it with the observable c as defined in Eq. (3.11). We introduce the short hand notation

$$X := \frac{x_1}{L_1},\quad Y := \frac{y}{L_1},\quad \delta Y := \frac{\delta y}{L_1}$$

and continue with calculating the term P as

$$\begin{aligned}
P &= \left\langle\cos\left(2\pi\left(Y+\delta Y\right)\left(q+\delta q\right)\right)\cos\left(2\pi\left(Y+\delta Y+X\right)\left(q+\delta q\right)\right)\right\rangle_{\delta q} \\
&= \frac{1}{4\mathscr{C}}\sum_{\delta q=-\infty}^{\infty}\mathrm{e}^{-\delta q^2/2\Delta q^2}\left(\mathrm{e}^{\mathrm{i}2\pi(2Y+2\delta Y+X)(q+\delta q)}+\mathrm{e}^{-\mathrm{i}2\pi X(q+\delta q)}+\mathrm{e}^{\mathrm{i}2\pi X(q+\delta q)}+\mathrm{e}^{-\mathrm{i}2\pi(2Y+2\delta Y+X)(q+\delta q)}\right)
\end{aligned}$$

$$
\begin{aligned}
&= \frac{1}{4\mathscr{C}} \left(\mathrm{e}^{\mathrm{i}2\pi(2Y+2\delta Y+X)q} \sum_{\delta q=-\infty}^{\infty} \mathrm{e}^{-\delta q^2/2\Delta q^2+\mathrm{i}2\pi(2Y+2\delta Y+X)\delta q} + \mathrm{e}^{-\mathrm{i}2\pi Xq} \sum_{\delta q=-\infty}^{\infty} \mathrm{e}^{-\delta q^2/2\Delta q^2-\mathrm{i}2\pi X\delta q} \right. \\
&\qquad \left. + \mathrm{e}^{\mathrm{i}2\pi Xq} \sum_{\delta q=-\infty}^{\infty} \mathrm{e}^{-\delta q^2/2\Delta q^2+\mathrm{i}2\pi X\delta q} + \mathrm{e}^{-\mathrm{i}2\pi(2Y+2\delta Y+X)q} \sum_{\delta q=-\infty}^{\infty} \mathrm{e}^{-\delta q^2/2\Delta q^2-\mathrm{i}2\pi(2Y+2\delta Y+X)\delta q} \right) \\
&= \frac{1}{4\mathscr{C}} \left[\mathrm{e}^{\mathrm{i}2\pi(2Y+2\delta Y+X)q} \vartheta\left(2Y+2\delta Y+X, \mathrm{i}/2\pi\Delta q^2\right) + \mathrm{e}^{-\mathrm{i}2\pi Xq} \vartheta\left(-X, \mathrm{i}/2\pi\Delta q^2\right) \right. \\
&\qquad \left. + \mathrm{e}^{\mathrm{i}2\pi Xq} \vartheta\left(X, \mathrm{i}/2\pi\Delta q^2\right) + \mathrm{e}^{-\mathrm{i}2\pi(2Y+2\delta Y+X)q} \vartheta\left(-2Y-2\delta Y-X, \mathrm{i}/2\pi\Delta q^2\right) \right] \\
&= \frac{1}{2\vartheta\left(0, \mathrm{i}/2\pi\Delta q^2\right)} \left[\cos\left(2\pi\left(2Y+2\delta Y+X\right)q\right) \vartheta\left(2Y+2\delta Y+X, \mathrm{i}/2\pi\Delta q^2\right) \right. \\
&\qquad \left. + \cos\left(2\pi Xq\right) \vartheta\left(X, \mathrm{i}/2\pi\Delta q^2\right) \right],
\end{aligned}
\tag{D.22}
$$

where

- we introduced the Jacobi theta function of the third kind

$$
\vartheta(z,s) = \sum_{\tau=-\infty}^{\infty} \mathrm{e}^{\mathrm{i}\pi\tau^2 s+\mathrm{i}2\pi\tau z} = 1 + 2\sum_{\tau=1}^{\infty} \mathrm{e}^{\mathrm{i}\pi\tau^2 s} \cos(2\pi\tau z),
\tag{D.23}
$$

- we used in the last step that $\vartheta(z,s) = \vartheta(-z,s)$,
- we identified $\mathscr{C} = \vartheta\left(0, \mathrm{i}/2\pi\Delta q^2\right)$.

Analogously, we calculate S:

$$
\begin{aligned}
S &= \left\langle \cos\left(2\pi\left(Y+\delta Y\right)\left(q+\delta q\right)\right) + \cos\left(2\pi\left(Y+\delta Y+X\right)\left(q+\delta q\right)\right) \right\rangle_{\delta q} \\
&= \frac{1}{2\mathscr{C}} \sum_{\delta q=-\infty}^{\infty} \mathrm{e}^{-\delta q^2/2\Delta q^2} \left(\mathrm{e}^{\mathrm{i}2\pi\left(Y+\delta Y\right)\left(q+\delta q\right)} + \mathrm{e}^{-\mathrm{i}2\pi\left(Y+\delta Y\right)\left(q+\delta q\right)} + \mathrm{e}^{\mathrm{i}2\pi\left(Y+\delta Y+X\right)\left(q+\delta q\right)} + \mathrm{e}^{-\mathrm{i}2\pi\left(Y+\delta Y+X\right)\left(q+\delta q\right)} \right) \\
&= \frac{1}{2\mathscr{C}} \left(\mathrm{e}^{\mathrm{i}2\pi(Y+\delta Y)q} \sum_{\delta q=-\infty}^{\infty} \mathrm{e}^{-\delta q^2/2\Delta q^2+\mathrm{i}2\pi(Y+\delta Y)\delta q} + \mathrm{e}^{-\mathrm{i}2\pi(Y+\delta Y)q} \sum_{\delta q=-\infty}^{\infty} \mathrm{e}^{-\delta q^2/2\Delta q^2-\mathrm{i}2\pi(Y+\delta Y)\delta q} \right. \\
&\qquad \left. + \mathrm{e}^{\mathrm{i}2\pi(Y+\delta Y+X)q} \sum_{\delta q=-\infty}^{\infty} \mathrm{e}^{-\delta q^2/2\Delta q^2+\mathrm{i}2\pi(Y+\delta Y+X)\delta q} + \mathrm{e}^{-\mathrm{i}2\pi(Y+\delta Y+X)q} \sum_{\delta q=-\infty}^{\infty} \mathrm{e}^{-\delta q^2/2\Delta q^2-\mathrm{i}2\pi(Y+\delta Y+X)\delta q} \right) \\
&= \frac{1}{\vartheta\left(0, \mathrm{i}/2\pi\Delta q^2\right)} \left[\cos\left(2\pi\left(Y+\delta Y\right)q\right) \vartheta\left(Y+\delta Y, \mathrm{i}/2\pi\Delta q^2\right) \right. \\
&\qquad \left. + \cos\left(2\pi\left(Y+\delta Y+X\right)q\right) \vartheta\left(Y+\delta Y+X, \mathrm{i}/2\pi\Delta q^2\right) \right].
\end{aligned}
\tag{D.24}
$$

We proceed to insert the expressions for P and S into Eq. (D.21) and thereby obtain

$$\begin{aligned}\left\langle c_\varsigma(x,y)\right\rangle_{\eta,\delta q} =& \frac{A^2}{2\vartheta\left(0,\mathrm{i}/2\pi\Delta q^2\right)}\left[\cos\left(2\pi\left(2Y+2\delta Y+X\right)q\right)\vartheta\left(2Y+2\delta Y+X,\mathrm{i}/2\pi\Delta q^2\right)\right.\\ &\left.+\cos\left(2\pi Xq\right)\vartheta\left(X,\mathrm{i}/2\pi\Delta q^2\right)\right]\\ &+\frac{B\sigma_0 A}{\vartheta\left(0,\mathrm{i}/2\pi\Delta q^2\right)}\left[\cos\left(2\pi\left(Y+\delta Y\right)q\right)\vartheta\left(Y+\delta Y,\mathrm{i}/2\pi\Delta q^2\right)\right.\\ &\left.+\cos\left(2\pi\left(Y+\delta Y+X\right)q\right)\vartheta\left(Y+\delta Y+X,\mathrm{i}/2\pi\Delta q^2\right)\right]\\ &+B^2\sigma_0^2+\varepsilon^2\delta_{x,0}.\end{aligned} \tag{D.25}$$

D.4.2 Ensembles Averages with Assumed Distributions of δy

We calculate the ensemble average of $c_\varsigma(x,y)$

$$\left\langle c_\varsigma(x,y)\right\rangle = \int_{-\infty}^{\infty}\mathrm{d}\delta y\; p_y(\delta y)\;\left\langle c_\varsigma(x,y)\right\rangle_{\eta,\delta q} \tag{D.26}$$

under the assumption of two special cases of the distribution of the spatial shift $p_y(\delta y)$:

I A delta peak distribution where no shift occurs: $p_y^{\mathrm{I}}(\delta y)=\delta(\delta y)$

II A uniformly distributed shift over the whole lattice: $p_y^{\mathrm{II}}(\delta y)=\Theta(\delta y)\Theta(L_1-\delta y)/L_1$

Case I

Case I is easily calculated as

$$\begin{aligned}\left\langle c_\varsigma(x,y)\right\rangle^{\mathrm{I}} =& \int_{-\infty}^{\infty}\mathrm{d}\delta y\;\delta(\delta y)\;\left\langle c_\varsigma(x,y)\right\rangle_{\eta,\delta q}\\ =&\frac{A^2}{2\vartheta\left(0,\mathrm{i}/2\pi\Delta q^2\right)}\left[\cos\left(2\pi\left(2Y+X\right)q\right)\vartheta\left(2Y+X,\mathrm{i}/2\pi\Delta q^2\right)+\cos\left(2\pi Xq\right)\vartheta\left(X,\mathrm{i}/2\pi\Delta q^2\right)\right]\\ &+\frac{B\sigma_0 A}{\vartheta\left(0,\mathrm{i}/2\pi\Delta q^2\right)}\left[\cos\left(2\pi Yq\right)\vartheta\left(Y,\mathrm{i}/2\pi\Delta q^2\right)+\cos\left(2\pi\left(Y+X\right)q\right)\vartheta\left(Y+X,\mathrm{i}/2\pi\Delta q^2\right)\right]\\ &+B^2\sigma_0^2+\varepsilon^2\delta_{x,0}.\end{aligned} \tag{D.27}$$

Case II

Case II limits the integration interval and we need to perform integrals over terms $T(s,\alpha,\beta,\gamma)$ for the case $\alpha,\beta,\gamma\in\mathbb{Z},\ \beta\neq 0$ as

$$\frac{1}{L}\int_0^L\mathrm{d}\delta y\,T\left(s,\alpha,\beta,\gamma\right)=\frac{1}{L}\int_0^L\mathrm{d}\delta y\,\mathrm{e}^{s\mathrm{i}2\pi\left(\alpha Y+\beta\delta Y+\gamma X\right)q}\sum_{\delta q=-\infty}^{\infty}\mathrm{e}^{-\delta q^2/2\Delta q^2+\mathrm{i}2\pi\left(\alpha Y+\beta\delta Y+\gamma X\right)\delta q}$$

$$
\begin{aligned}
&= \mathrm{e}^{s\mathrm{i}2\pi(\alpha Y+\gamma X)q} \sum_{\delta q=-\infty}^{\infty} \mathrm{e}^{-\delta q^2/2\Delta q^2+\mathrm{i}2\pi(\alpha Y+\gamma X)\delta q} \frac{1}{L}\int_0^L \mathrm{d}\delta y\, \mathrm{e}^{\mathrm{i}2\pi\beta\delta Y(\delta q+sq)} \\
&= \mathrm{e}^{s\mathrm{i}2\pi(\alpha Y+\gamma X)q} \sum_{\delta q=-\infty}^{\infty} \mathrm{e}^{-\delta q^2/2\Delta q^2+\mathrm{i}2\pi(\alpha Y+\gamma X)\delta q} \delta_{\delta q,-sq} \\
&= \mathrm{e}^{s\mathrm{i}2\pi(\alpha Y+\gamma X)q} \mathrm{e}^{-\delta q^2/2\Delta q^2-\mathrm{i}2\pi(\alpha Y+\gamma X)sq} = \mathrm{e}^{-\delta q^2/2\Delta q^2}
\end{aligned} \tag{D.28}
$$

and for $\beta = 0$

$$
\frac{1}{L}\int_0^L \mathrm{d}\delta y\, T\left(s,\alpha,0,\gamma\right) = T\left(s,\alpha,0,\gamma\right). \tag{D.29}
$$

Using this, we can calculate the ensemble average for Case II

$$
\begin{aligned}
\left\langle c_\varsigma(x,y)\right\rangle^{\mathrm{II}} &= \frac{1}{L}\int_0^L \mathrm{d}\delta y\, \left\langle c_\varsigma(x,y)\right\rangle_{\eta,\delta q} \\
&= \frac{1}{L}\int_0^L \mathrm{d}\delta y \left[\frac{A^2}{4\vartheta\left(0,\mathrm{i}/2\pi\Delta q^2\right)} \left(T(+,2,2,1) + T(-,2,2,1) + T(+,0,0,1) + T(+,0,0,1) \right) \right. \\
&\qquad + \frac{B\sigma_0 A}{2\vartheta\left(0,\mathrm{i}/2\pi\Delta q^2\right)} \left(T(+,1,1,0) + T(-,1,1,0) + T(+,1,1,1) + T(-,1,1,1) \right) \\
&\qquad \left. + B^2\sigma_0^2 + \varepsilon^2\delta_{x,0} \right] \\
&= \frac{A^2}{2\vartheta\left(0,\mathrm{i}/2\pi\Delta q^2\right)} \left(\mathrm{e}^{-\delta q^2/2\Delta q^2} + \cos\left(2\pi X q\right)\vartheta\left(X,\mathrm{i}/2\pi\Delta q^2\right) \right) \\
&\quad + \frac{2AB\sigma_0}{\vartheta\left(0,\mathrm{i}/2\pi\Delta q^2\right)} \mathrm{e}^{-\delta q^2/2\Delta q^2} + \sigma_0^2 + \varepsilon^2\delta_{x,0} \\
&\approx \frac{A^2}{2\vartheta\left(0,\mathrm{i}/2\pi\Delta q^2\right)} \cos\left(2\pi X q\right)\vartheta\left(X,\mathrm{i}/2\pi\Delta q^2\right) + B^2\sigma_0^2 + \varepsilon^2\delta_{x,0} \equiv \left\langle \bar{c}_\varsigma(x)\right\rangle.
\end{aligned} \tag{D.30}
$$

D.4.3 Spatial Average over y

The expression in Eq. (D.25) (more precisely the terms S and P) still depends on the shift. This dependence vanishes when we perform the spatial average over y. To show this, we have to perform summations over similar terms of the general form

$$
T\left(s,\alpha,\beta,\gamma\right) = \mathrm{e}^{s\mathrm{i}2\pi(\alpha Y+\beta\delta Y+\gamma X)q} \sum_{\delta q=-\infty}^{\infty} \mathrm{e}^{-\delta q^2/2\Delta q^2+\mathrm{i}2\pi(\alpha Y+\beta\delta Y+\gamma X)\delta q}. \tag{D.31}
$$

We perform the y average over this general term assuming that $\alpha,\beta,\gamma\in\mathbb{Z}$, $\alpha\neq 0$ and obtain

$$
\begin{aligned}
\frac{1}{N_1}\sum_{y\in\Gamma_1} T\left(s,\alpha,\beta,\gamma\right) &= \frac{1}{N_1}\sum_{y\in\Gamma_1} \mathrm{e}^{s\mathrm{i}2\pi(\alpha Y+\beta\delta Y+\gamma X)q} \sum_{\delta q=-\infty}^{\infty} \mathrm{e}^{-\delta q^2/2\Delta q^2+\mathrm{i}2\pi(\alpha Y+\beta\delta Y+\gamma X)\delta q} \\
&= \mathrm{e}^{s\mathrm{i}2\pi(\beta\delta Y+\gamma X)q} \sum_{\delta q=-\infty}^{\infty} \mathrm{e}^{-\delta q^2/2\Delta q^2+\mathrm{i}2\pi(\beta\delta Y+\gamma X)\delta q} \frac{1}{N_1}\sum_{y\in\Gamma_1} \mathrm{e}^{\mathrm{i}2\pi\alpha Y(\delta q+sq)}
\end{aligned}
$$

$$
\begin{aligned}
&= \mathrm{e}^{s\mathrm{i}2\pi(\beta\delta Y+\gamma X)q} \sum_{\delta q=-\infty}^{\infty} \mathrm{e}^{-\delta q^2/2\Delta q^2+\mathrm{i}2\pi(\beta\delta Y+\gamma X)\delta q}\delta_{\delta q,-sq} \\
&= \mathrm{e}^{s\mathrm{i}2\pi(\beta\delta Y+\gamma X)q}\mathrm{e}^{-\delta q^2/2\Delta q^2-\mathrm{i}2\pi(\beta\delta Y+\gamma X)sq} = \mathrm{e}^{-\delta q^2/2\Delta q^2}
\end{aligned} \tag{D.32}
$$

and for $\alpha = 0$

$$
\frac{1}{N_1}\sum_{y\in\Gamma_1} T\left(s,0,\beta,\gamma\right) = T\left(s,0,\beta,\gamma\right). \tag{D.33}
$$

Now we can calculate the spatial averages $\bar{S},\bar{P}$ of S,P respectively

$$
\begin{aligned}
\bar{S} = \frac{1}{N_1}\sum_{y\in\Gamma_1} S &= \frac{1}{N_1}\sum_{y\in\Gamma_1}\frac{1}{\vartheta\left(0,\mathrm{i}/2\pi\Delta q^2\right)}\Big[\cos\left(2\pi\left(Y+\delta Y\right)q\right)\vartheta\left(Y+\delta Y,\mathrm{i}/2\pi\Delta q^2\right) \\
&\qquad + \cos\left(2\pi\left(Y+\delta Y+X\right)q\right)\vartheta\left(Y+\delta Y+X,\mathrm{i}/2\pi\Delta q^2\right)\Big] \\
&= \frac{1}{2\vartheta\left(0,\mathrm{i}/2\pi\Delta q^2\right)}\frac{1}{N_1}\sum_{y\in\Gamma_1}\left(T(+,1,1,0)+T(-,1,1,0)+T(+,1,1,1)+T(-,1,1,1)\right) \\
&= \frac{2}{\vartheta\left(0,\mathrm{i}/2\pi\Delta q^2\right)}\mathrm{e}^{-\delta q^2/2\Delta q^2}
\end{aligned} \tag{D.34}
$$

and

$$
\begin{aligned}
\bar{P} = \frac{1}{N_1}\sum_{y\in\Gamma_1} P &= \frac{1}{N_1}\sum_{y\in\Gamma_1}\frac{1}{2\vartheta\left(0,\mathrm{i}/2\pi\Delta q^2\right)}\Big[\cos\left(2\pi\left(2Y+2\delta Y+X\right)q\right)\vartheta\left(2Y+2\delta Y+X,\mathrm{i}/2\pi\Delta q^2\right) \\
&\qquad + \cos\left(2\pi Xq\right)\vartheta\left(X,\mathrm{i}/2\pi\Delta q^2\right)\Big] \\
&= \frac{1}{4\vartheta\left(0,\mathrm{i}/2\pi\Delta q^2\right)}\frac{1}{N_1}\sum_{y\in\Gamma_1}\left(T(+,2,2,1)+T(-,2,2,1)+T(+,0,0,1)+T(-,0,0,1)\right) \\
&= \frac{1}{2\vartheta\left(0,\mathrm{i}/2\pi\Delta q^2\right)}\left[\mathrm{e}^{-\delta q^2/2\Delta q^2}+\cos\left(2\pi Xq\right)\vartheta\left(X,\mathrm{i}/2\pi\Delta q^2\right)\right].
\end{aligned} \tag{D.35}
$$

With the calculated $\bar{P}$ and $\bar{S}$ we are able to perform the spatial average over y of Eq. (D.25):

$$
\begin{aligned}
\left\langle\bar{c}_\varsigma(x)\right\rangle_{\eta,\delta q} = \frac{1}{N_1}\sum_{y\in\Gamma_1}\left\langle c(x,y)\right\rangle_{\eta,\delta q} &= A^2\bar{P} + B\sigma_0 A\bar{S} + B^2\sigma_0^2 + \varepsilon^2\delta_{x,0} \\
&= \frac{A^2}{2\vartheta\left(0,\mathrm{i}/2\pi\Delta q^2\right)}\left[\mathrm{e}^{-\delta q^2/2\Delta q^2}+\cos\left(2\pi Xq\right)\vartheta\left(X,\mathrm{i}/2\pi\Delta q^2\right)\right] \\
&\quad + \frac{2AB\sigma_0}{\vartheta\left(0,\mathrm{i}/2\pi\Delta q^2\right)}\mathrm{e}^{-\delta q^2/2\Delta q^2} + B^2\sigma_0^2 + \varepsilon^2\delta_{x,0} \\
&\approx \frac{A^2}{2\vartheta\left(0,\mathrm{i}/2\pi\Delta q^2\right)}\cos\left(2\pi Xq\right)\vartheta\left(X,\mathrm{i}/2\pi\Delta q^2\right) + B^2\sigma_0^2 + \varepsilon^2\delta_{x,0}
\end{aligned}
$$

$$\equiv \left\langle \bar{c}_\varsigma(x) \right\rangle, \tag{D.36}$$

where we neglected terms $\propto \exp\left(-q^2/2\Delta q^2\right)$ under the assumption that $q \gg \Delta q$. The resulting expression does not depend on the spatial shift δy anymore and thus is equal to the full expectation value $\left\langle \bar{c}_\varsigma(x) \right\rangle$. The observable $C_\varsigma(x)$ reduces in the different phases to

$$C_{\varsigma_{\mathrm{SP}}}(x) = \varepsilon^2 \delta_{x,0} \qquad \text{in the SP,} \tag{D.37a}$$

$$C_{\varsigma_{\mathrm{HBP}}}(x) = B^2\sigma_0^2 + \varepsilon^2 \delta_{x,0} \qquad \text{in the HBP,} \tag{D.37b}$$

$$C_{\varsigma_{\mathrm{IP}}}(x) = \frac{A^2}{2\vartheta\left(0, \mathrm{i}/2\pi\Delta q^2\right)} \cos\left(2\pi\, x q / L_1\right) \vartheta\left(x/L_1, \mathrm{i}/2\pi\Delta q^2\right) + \varepsilon^2 \delta_{x,0} \qquad \text{in the IP.} \tag{D.37c}$$

E Uninterpolated Phase Diagram Plots

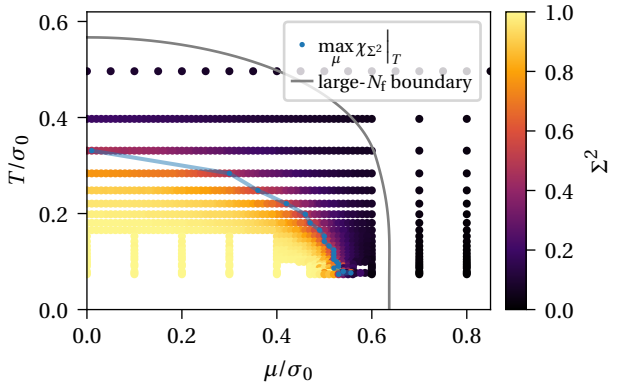

Figure E.1: The uninterpolated data corresponding to Figure 3.9.

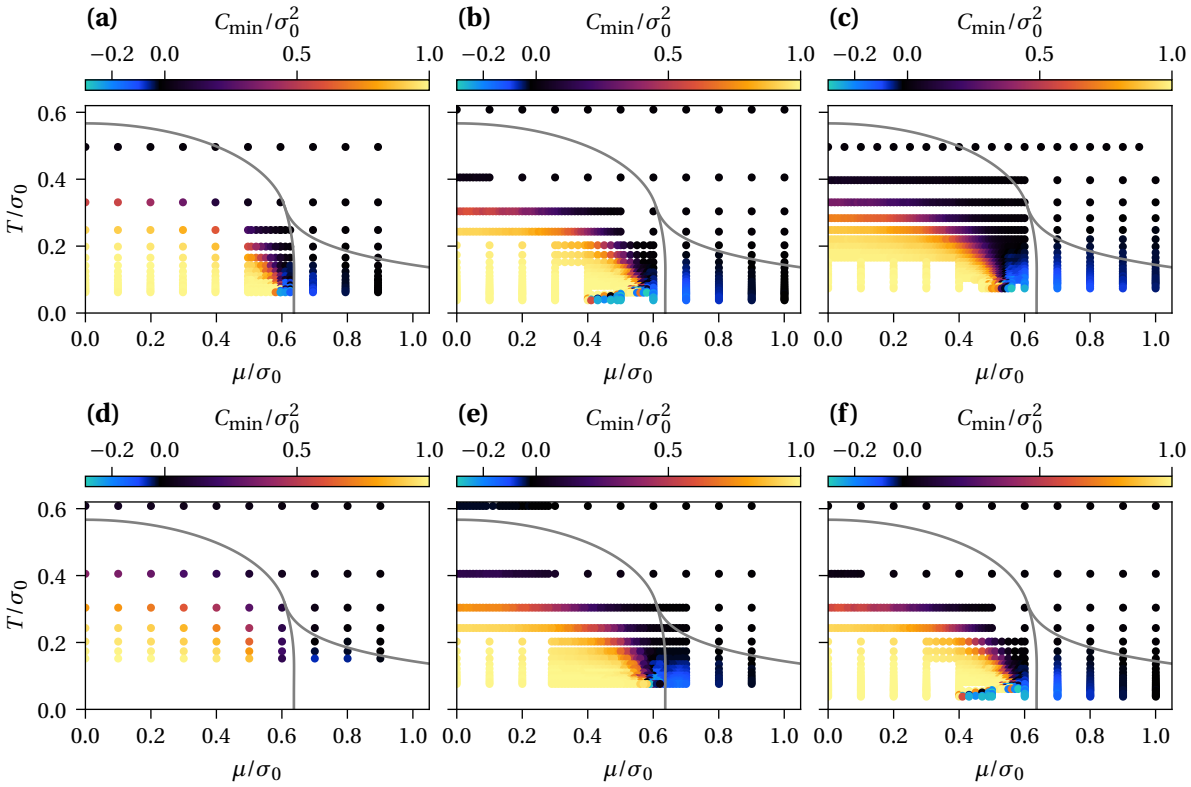

Figure E.2: The uninterpolated data corresponding to Figure 3.12. **(a)** Figure 3.12a. **(b)** Figure 3.12b.**(c)** Figure 3.12c. **(d)** Figure 3.12g. **(e)** Figure 3.12h. **(f)** Figure 3.12i.

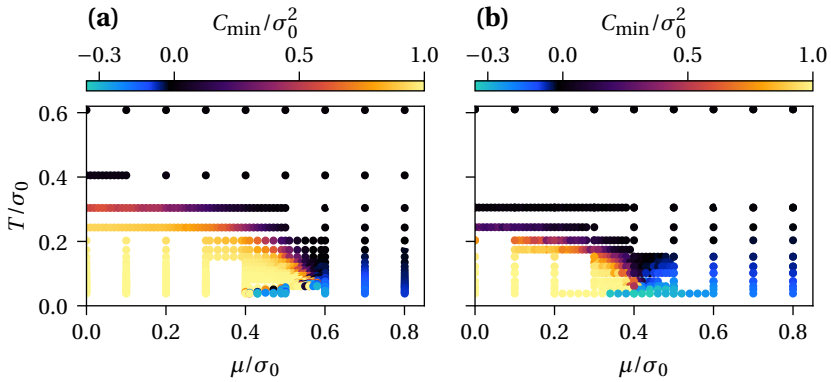

Figure E.3: The uninterpolated data corresponding to Figure 3.15. **(a)** Figure 3.15a. **(b)** Figure 3.15c.

Bibliography

[1] D. J. Gross and A. Neveu. “Dynamical Symmetry Breaking in Asymptotically Free Field Theories”. In: *Phys. Rev.* D10 (1974), 3235.

[2] U. Wolff. “The Phase Diagram of the Infinite N Gross-Neveu Model at Finite Temperature and Chemical Potential”. In: *Phys. Lett.* 157B (1985), 303.

[3] M. Thies and K. Urlichs. “Revised Phase Diagram of the Gross-Neveu Model”. In: *Phys. Rev.* D67 (2003), 125015. arXiv: hep-th/0302092.

[4] O. Schnetz, M. Thies, and K. Urlichs. “Phase Diagram of the Gross-Neveu Model: Exact Results and Condensed Matter Precursors”. In: *Ann. Phys* 314 (2004), 425. arXiv: hep-th/0402014.

[5] M. Buballa and S. Carignano. “Inhomogeneous Chiral Condensates”. In: *Prog. Part. Nucl. Phys.* 81 (2015), 39. arXiv: 1406.1367 [hep-ph].

[6] D. Nickel. “Inhomogeneous Phases in the Nambu-Jona-Lasino and Quark-Meson Model”. In: *Phys. Rev.* D80 (2009), 074025. arXiv: 0906.5295 [hep-ph].

[7] V. Schön and M. Thies. “Emergence of Skyrme Crystal in Gross-Neveu and ’t Hooft Models at Finite Density”. In: *Phys. Rev. D* 62.9 (2000), 096002. arXiv: hep-th/0003195.

[8] G. Basar, G. V. Dunne, and M. Thies. “Inhomogeneous Condensates in the Thermodynamics of the Chiral NJL(2) Model”. In: *Phys. Rev.* D79 (2009), 105012. arXiv: 0903.1868 [hep-th].

[9] M. Thies. “Phase Structure of the 1+1 Dimensional NambuJona-Lasinio Model with Isospin”. In: *Phys. Rev. D* 101.1 (2020), 014010. arXiv: 1911.11439.

[10] M. Thies. “First-Order Phase Boundaries of the Massive 1+1 Dimensional Nambu–Jona-Lasinio Model with Isospin”. In: *Phys. Rev. D* 101.7 (2020), 074013. arXiv: 2002.01190.

[11] S. Carignano, M. Buballa, and B.-J. Schaefer. “Inhomogeneous Phases in the Quark-Meson Model with Vacuum Fluctuations”. In: *Phys. Rev. D* 90.1 (2014), 014033. arXiv: 1404.0057.

[12] J. Mertsching and H. J. Fischbeck. “The Incommensurate Peierls Phase of the Quasi-One-Dimensional Fröhlich Model with a Nearly Half-Filled Band”. In: *Phys. Status Solidi B* 103.2 (1981), 783.

[13] D. V. Deryagin, D. Yu. Grigoriev, and V. A. Rubakov. “Standing Wave Ground State in High Density, Zero Temperature QCD at Large Nc”. In: *Int. J. Mod. Phys. A* 07.04 (1992), 659.

[14] E. Shuster and D. T. Son. “On Finite-Density QCD at Large Nc”. In: *Nucl. Phys. B* 573.1-2 (2000), 434. arXiv: hep-ph/9905448.

[15] F. Karsch, J. B. Kogut, and H. W. Wyld. “The Gross-Neveu Model at Finite Temperature and Density”. In: *Nucl. Phys.* B280 (1987), 289.

[16] J. Lenz, L. Pannullo, M. Wagner, B. Wellegehausen, and A. Wipf. “Inhomogeneous Phases in the Gross-Neveu Model in 1+1 Dimensions at Finite Number of Flavors”. In: *Phys. Rev.* D (2020). arXiv: 2004.00295. Forthcoming.

[17] J. I. Kapusta and C. Gale. *Finite-Temperature Field Theory: Principles and Applications*. Cambridge University Press, 2006.

[18] A. Wipf. “Statistical Approach to Quantum Field Theory: An introduction”. In: *Lect. Notes Phys.* 864 (2013).

[19] C. Wetterich. “Spinors in Euclidean Field Theory, Complex Structures and Discrete Symmetries”. In: *Nucl. Phys. B* 852.1 (2011), 174. arXiv: 1002.3556.

[20] H. Murayama. “Lecture Notes on ’Clifford Algebra and Spin(N) Representations’”.
[21] R. L. Stratonovich. “On a Method of Calculating Quantum Distribution Functions”. In: *Sov. Phys. Dokl.* 2 (1957), 416.
[22] J. Hubbard. “Calculation of Partition Functions”. In: *Phys. Rev. Lett.* 3.2 (1959), 77.
[23] H. Gies and L. Janssen. “UV Fixed-Point Structure of the Three-Dimensional Thirring Model”. In: *Phys. Rev. D* 82.8 (2010), 085018. arXiv: 1006.3747.
[24] M. Thies. “From Relativistic Quantum Fields to Condensed Matter and Back Again: Updating the Gross-Neveu Phase Diagram”. In: *J. Phys. A: Math. Gen.* 39.41 (2006), 12707. arXiv: hep-th/0601049.
[25] S. R. Coleman. “There Are No Goldstone Bosons in Two-Dimensions”. In: *Commun. Math. Phys.* 31 (1973), 259.
[26] E. Witten. “Chiral Symmetry, the 1/n Expansion, and the SU(N) Thirring Model”. In: *Nucl. Phys.* B145 (1978), 110.
[27] Y. Cohen, S. Elitzur, and E. Rabinovici. “A Monte Carlo Study of the Gross-Neveu Model”. In: *Nucl. Phys.* B220 (1983), 102.
[28] H. B. Nielsen and M. Ninomiya. “No Go Theorem for Regularizing Chiral Fermions”. In: *Phys. Lett.* 105B (1981), 219.
[29] H. B. Nielsen and M. Ninomiya. “Absence of Neutrinos on a Lattice: (I). Proof by Homotopy Theory”. In: *Nucl. Phys. B* 185.1 (1981), 20.
[30] H. B. Nielsen and M. Ninomiya. “Absence of Neutrinos on a Lattice: (II). Intuitive Topological Proof”. In: *Nucl. Phys. B* 193.1 (1981), 173.
[31] P. Hasenfratz and F. Karsch. “Chemical Potential on the Lattice”. In: *Phys. Lett. B* 125.4 (1983), 308.
[32] J. Lenz, L. Pannullo, M. Wagner, B. Wellegehausen, and A. Wipf. In preparation.
[33] C. Gattringer and C. B. Lang. “Quantum Chromodynamics on the Lattice”. In: *Lect. Notes Phys.* 788 (2010), 1.
[34] S. Aoki and K. Higashijima. “The Recovery of the Chiral Symmetry in Lattice Gross-Neveu Model”. In: *Prog. Theor. Phys.* 76 (1986), 521.
[35] S. D. Drell, M. Weinstein, and S. Yankielowicz. “Variational Approach to Strong Coupling Field Theory. 1. Phi**4 Theory”. In: *Phys. Rev.* D14 (1976), 487.
[36] S. D. Drell, M. Weinstein, and S. Yankielowicz. “Strong-Coupling Field Theories. II. Fermions and Gauge Fields on a Lattice”. In: *Phys. Rev. D* 14.6 (1976), 1627.
[37] L. H. Karsten and J. Smit. “The Vacuum Polarization with SLAC Lattice Fermions”. In: *Phys. Lett.* 85B (1979), 100.
[38] G. Bergner, T. Kaestner, S. Uhlmann, and A. Wipf. “Low-Dimensional Supersymmetric Lattice Models”. In: *Ann. Phys* 323 (2008), 946. arXiv: 0705.2212 [hep-lat].
[39] B. H. Wellegehausen, D. Schmidt, and A. Wipf. “Critical Flavor Number of the Thirring Model in Three Dimensions”. In: *Phys. Rev.* D96.9 (2017), 094504. arXiv: 1708.01160 [hep-lat].
[40] J. Lenz, B. H. Wellegehausen, and A. Wipf. “Absence of Chiral Symmetry Breaking in Thirring Models in 1+2 Dimensions”. In: *Phys. Rev.* D100.5 (2019), 054501. arXiv: 1905.00137 [hep-lat].
[41] H. J. Rothe. *Lattice Gauge Theories*. 4th ed. World Scientific, 2012.
[42] P. de Forcrand and U. Wenger. “New Baryon Matter in the Lattice Gross-Neveu Model”. In: *Proceedings, 24th International Symposium on Lattice Field Theory (Lattice 2006): Tucson, USA, July 23-28, 2006*. Vol. LAT2006. PoS. 2006, 152. arXiv: hep-lat/0610117.
[43] M. Wagner. “Fermions in the Pseudoparticle Approach”. In: *Phys. Rev.* D76 (2007), 076002. arXiv: 0704.3023 [hep-lat].
[44] A. Heinz, F. Giacosa, M. Wagner, and D. H. Rischke. “Inhomogeneous Condensation in Effective Models for QCD Using the Finite-Mode Approach”. In: *Phys. Rev.* D93.1 (2016), 014007. arXiv: 1508.06057 [hep-ph].

[45] M. Winstel, J. Stoll, and M. Wagner. “Lattice Investigation of an Inhomogeneous Phase of the 2+1-Dimensional Gross-Neveu Model in the Limit of Infinitely Many Flavors”. 2019. arXiv: 1909.00064 [hep-lat].
[46] M. Buballa, L. Kurth, M. Wagner, and M. Winstel. In preparation.
[47] A. D. Kennedy. “Algorithms for Dynamical Fermions”. 2012. arXiv: hep-lat/0607038.
[48] W. Janke. “Monte Carlo Methods in Classical Statistical Physics”. In: *Computational Many-Particle Physics*. Vol. 739. Berlin, Heidelberg: Springer Berlin Heidelberg, 2008, 79.
[49] B. H. Wellegehausen. “Phase Diagrams of Exceptional and Supersymmetric Lattice Gauge Theories”. Phd thesis. Friedrich-Schiller-Universität Jena, 2012.
[50] D. Schmidt. “Three-Dimensional Four-Fermion Theories with Exact Chiral Symmetry on the Lattice”. Phd thesis. Friedrich-Schiller-Universität Jena.
[51] D. H. Weingarten and D. N. Petcher. “Monte Carlo Integration for Lattice Gauge Theories with Fermions”. In: *Phys. Lett. B* 99.4 (1981), 333.
[52] F. Fucito, E. Marinari, G. Parisi, and C. Rebbi. “A Proposal for Monte Carlo Simulations of Fermionic Systems”. In: *Nucl. Phys. B* 180.3 (1981), 369.
[53] W. Fraser. “A Survey of Methods of Computing Minimax and Near-Minimax Polynomial Approximations for Functions of a Single Independent Variable”. In: 12 (1965), 295.
[54] K. Urlichs. “Baryons and Baryonic Matter in Four-Fermion Interaction Models”. Phd thesis. Friedrich-Alexander-Universität Erlangen-Nürnberg, 2007.
[55] R. Narayanan. “Phase Diagram of the Large N Gross-Neveu Model in a Finite Periodic Box”. 2020. arXiv: 2001.09200.
[56] M. Sadzikowski. “Coexistence of Pion Condensation and Color Superconductivity in Two Flavor Quark Matter”. In: *Physics Letters B* 553.1-2 (2003), 45. arXiv: hep-ph/0210065.
[57] M. Sadzikowski. “Comparison of the Non-Uniform Chiral and 2SC Phases at Finite Temperatures and Densities”. In: *Physics Letters B* 642.3 (2006), 238. arXiv: hep-ph/0609186.
[58] I. S. Gradshten, I. M. Ryzhik, and A. Jeffrey. *Table of Integrals, Series, and Products*. 7th ed. Amsterdam ; Boston: Academic Press, 2007.
[59] H. Kleinert. *Particles and Quantum Fields*. World Scientific, 2016.
[60] M. Wagner. “Lecture Notes on ’Numerical Methods in Physics’”.
[61] D. P. Bertsekas and J. N. Tsitsiklis. *Introduction to Probability*. 2nd edition. Belmont, Massachusetts: Athena Scientific, 2008. 544 pp.

Acknowledgements

I want to thank Prof. Marc Wagner for his great supervision and the many helpful discussion, which he always managed to integrate into his schedule. Moreover, I want to thank him for introducing me into the CRC-TR 211 and for providing me the opportunity to attend the LATTICE conference in Wuhan.
My next thanks goes to Alessandro Sciarra, who, albeit not involved in my project, always took the time to discuss and help me with virtually any question that I threw at him when he just wanted to get some coffee.
My thanks also go to Julian Lenz, who helped me with the troubles I had in using and extending the simulation code. He also provided useful Python scripts that I used to extract the simulation results for some of the result plots in Chapter 3.
I would also like to thank Marc Winstel for his useful comments on the manuscript of this thesis and Tom Weatherby for proofreading it.
Finally, I would like to thank Laura who could not help me with the subject of my thesis but supported me in every other way.

Selbstständigkeitserklärung

Hiermit erkläre ich, dass ich die Arbeit selbstständig und ohne Benutzung anderer als der angegebenen Quellen und Hilfsmittel verfasst habe. Alle Stellen der Arbeit, die wörtlich oder sinngemäß aus Veröffentlichungen oder aus anderen fremden Texten entnommen wurden, sind von mir als solche kenntlich gemacht worden. Ferner erkläre ich, dass die Arbeit nicht - auch nicht auszugsweise - für eine andere Prüfung verwendet wurde.

Frankfurt, den 6. Mai, 2020 _____

(Laurin Pannullo)